Simulation of flooding due to embankment breaches by Delft3D Flexible Mesh

Case study of coastal area in Shanghai

Jiangshan Yin
May, 2020

MSc Thesis

Simulation of flooding due to embankment breaches by Delft3D Flexible Mesh

Case study of coastal area in Shanghai

by

Jiangshan Yin

Student number:	4735684	
Thesis committee:	Prof. dr. ir. S. G. J. Aarninkhof,	TU Delft
	Dr. ir. J. D. Bricker,	TU Delft
	Dr. Q. Ke,	TU Delft
	Dr. ir. P. J. Visser,	TU Delft

This thesis is confidential and cannot be made public until May 18, 2020.

Delft University of Technology

Faculty of Civil Engineering and Geosciences (CEG)
Hydraulic Engineering
May, 2020

Abstract

As a low-lying city, Shanghai faces threats from typhoon and spring tide under the condition of climate change and land subsidence. With high water level at the toe, the sea embankment is likely to be overtopped and breached, finally resulting in inundation inland.

The objective of this research is to study climate change and land subsidence effects on Shanghai inland inundation due to dike overtopping and breaching under extreme weather condition.

A hydrodynamic model and a wave model have been established by Delft3D-FM and Delft3D respectively. Through validations on historical events, the hydrodynamic model and wave model are proved to be valid. The water level and wave condition along the coast, which are concerned as the results of these two models, are also essential inputs for overtopping and breach discharge calculation. In overtopping and breach discharge calculation, the threshold of breaching is estimated as an overtopping rate of 0.1 $m^3/m/s$. The resulting overtopping and breach discharge gives the boundary condition of the overland simulation. The inundation map over Shanghai area can then be achieved by the overland simulation. A sensitivity analysis of the breach widths is also done.

Ten hypothetical typhoon events are provided by the Met Office Hadley Center under past and future climate conditions. These cases are applied to the whole process to study the effects of climate change on coastal flooding in Shanghai. The relative sea level rise is also considered for both past and future climate conditions.

The results show that places with high water level and low sea dike elevation are more likely to get high overtopping that can finally result in breaching. For Shanghai city, such vulnerable places can be found along Hangzhou Bay, especially in Jinshan District and the south-east corner of Shanghai. Besides, the entrance of Shanghai Yangtze River Tunnel is also vulnerable due to land subsidence. For some extreme cases, the whole Shanghai coast is in danger.

In the future, given the challenge of climate change and land subsidence, the sea level is relatively rising. The intensity of typhoon will generally strengthen according to the simulation of the UK Met Office. For the past climate and land elevation

around the year 2000 with the wind speed return period [1] of 1.3 yr, it is simulated that 23 points along the embankment are likely to breach and the breach width is assumed to be 300 m. The maximum inundation area in Shanghai can be 1,805 km^2 (33.3% of the simulated area in Shanghai). For the future climate and land elevation around the year 2100 with the wind speed return period of 4.5 yr, it is simulated that 37 points along the embankment are likely to breach and the breach width is assumed to be 300 m. The inundation area in Shanghai can be 3,388 km^2 (62.4% of the simulated area in Shanghai), which is almost twice of the inundation area around the year 2000. In this case, the inundation area with the depth of 0-0.2 m is 327 km^2, 0.2-0.5 m depth is 526 km^2, 0.5-1 m depth is 1,047 km^2, 1-3 m depth is 1,154 km^2, larger than 3 m depth is 33 km^2.

The breach width also affects the inundation situation. With the 500 m breach width of each breach point, a maximum of 3,700 km^2 (68.2% of the simulation area) are flooded. With the 1,000 m breach width of each breach point, a maximum of 4,381 km^2 (80.7% of the simulation area) are flooded. If the breach width becomes larger, the inundation situation will be worse. However, as the breach width grows, the increase of the inundation area decreases.

This research provides inundation maps for Shanghai under different climate and land subsidence conditions, considering sea dike breaches due to overtopping. The results give strong support for further flood risk assessment and provide a reference for flood defence system maintenance and construction. The models in this research can also be applied to analyze the effects of forecasted typhoon and tide when the storm and tide conditions are provided.

---

[1] The return period is based on the maximum wind speed along the trajectory included in the Shanghai area of responsibility, rather than only hitting Shanghai.

Acknowledgement

This work has been carried out to meet the requirements of the Master of Science program in Civil Engineering at Delft University of Technology, the Netherlands. This research is also a part of the project called Sustainable Solutions for Managing Compound Flood Risks under Future Uncertainties: The Case of Shanghai City and the Yangtze River Delta Region. This project is funded and supported by Netherlands Organization for Scientific Research NWO (ALWSD.2016.007), National Natural Science Foundation NSFC (51761135024) and Engineering and Physical Sciences Research Council UK EPSRC (EP/R034214/1).

I would like to give my appreciation to all my committee members. Stefan Aarnikhof, my chairman, encouraged me a lot and told me how to be a good researcher. Jeremy Bricker, helped me a lot in the thesis structure and always guided me to the right way when I got confused. Qian Ke, my kind and patient daily supervisor, helped me with different kinds of problems I came across during the research. I am so happy to hear that you have a baby now. I wish your lucky boy a happy life. Paul Visser, gave me valuable advice on the breaching process and English writing, which helps me a lot.

I sincerely thank every member of Shanghai Project, including people from England, China and the Netherlands. I could not have completed my thesis on it without your efforts.

Moreover, I would like to thank my friends for giving me support and encouragement. With your accompany, my study time in Delft becomes so precious.

Finally, I would like to thank my parents, Qingmin Yin and Huijie Li. Your love and support are the greatest treasure of my life. I love you!

Jiangshan Yin
May 2020

Contents

1

Introduction

1.1 Background

Shanghai, one of the four direct-administered municipalities of China, situates on the eastern fringe of Yangtze River Delta, between 30°40′N-31°53′N and 120°52′E-122°12′E. Shanghai is a flat and low-lying area, it has the East China Sea to the east, Yangtze River to the north and Hangzhou Bay to the south, as shown in Fig 1.1. The total area of the municipality of Shanghai is 6,341 km^2 according to Shanghai Statistical Yearbook (2018). The coastline of Shanghai is about 172 km along the East China Sea (Yin et al., 2011). Shanghai experiences a northern subtropical monsoon climate (Niederleithinger et al., 2008), with an annual rainfall of 1,389 mm and an annual average temperature of 17.7 °C (Shanghai Statistical Yearbook, 2018). With a resident population of 24.2 million at the end of 2017, there are 16 districts or counties in Shanghai, according to Shanghai Statistical Yearbook (2018).

For the specific location near the coast and estuary, Shanghai experiences great flood risks from river, sea, lake and torrential rainfall. Among them, flood from the coast side is mainly considered in this research. Shanghai suffers from extreme tropical storm tide frequently. Typhoon, which usually occurs from July to September, is the common storm event that threats Shanghai coast.

1.2 Objective and research questions

The focus of this research is on:
To identify how climate change and land subsidence affect Shanghai inland inundation due to dike overtopping and breaching under extreme weather condition.

In order to achieve this objective, the project is separated into the following research questions:

1 Where are the vulnerable places to be overtopped and breached in Shanghai coast under extreme weather condition?

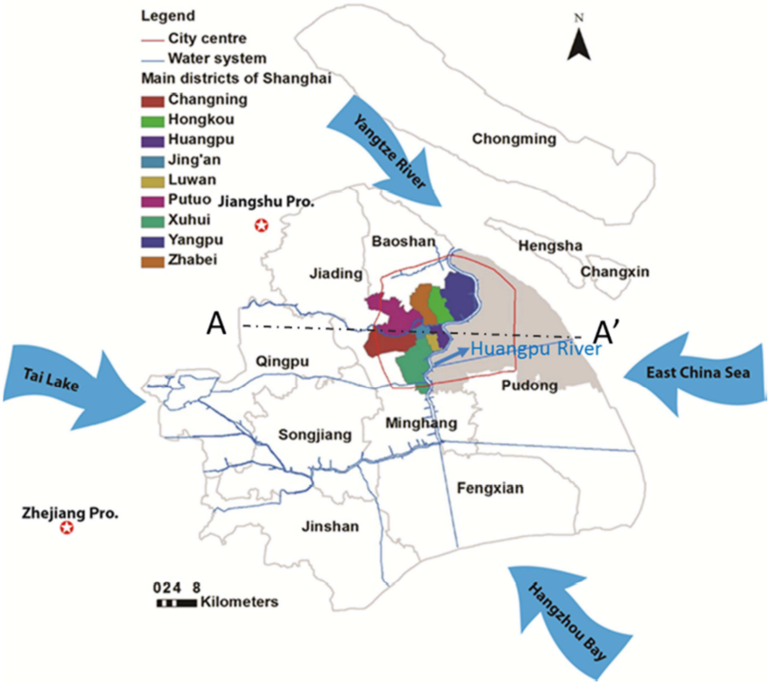

Fig. 1.1.: Shanghai municipality map (Ke, 2014)

2 How do climate change and land subsidence affect typhoon induced inundation in Shanghai?

1.3 General methodology

The research progress can be divided into five main stages. In order to make the research process more visualized, a flow chart as well as a schematic diagram for the main part of the research is shown in Fig. 1.2 and Fig. 1.3, respectively.

The main research method and progress is explained in the following sections.

Study area analysis

In the literature study, the storm impacts for Shanghai area are summarized. Input parameters and geographic data of the study area are prepared for the next step, e.g. tide constituents, storm conditions (incl. storm tracks, wind and pressure fields) and bathymetry condition. The information of the study area is shown in Chapter 2.

Hydrodynamic model and wave model

As shown in Fig. 1.2 and Fig. 1.3, the hydrodynamic model, which is represented by process ①, is established in D-FLOW module in Delft3D-FM. Two critical inputs of the hydrodynamic model are the tide level and storm conditions (incl. storm tracks, wind and pressure fields). Validation is needed to make sure the output reliable for the next step. The sources of these two inputs are different in the validation and application process. In the validation process, the tide is involved as tide constituents and the wind and pressure fields are generated from typhoon tracks by WES. The typhoon model also needs a validation. In the application process, the spring tide level in 1997 is used, which is simulated by the valid hydrodynamic model. The storm is simulated by the Met Office. The water level along the coast is concerned as a result.

Wave model, which is represented by process ② in Fig. 1.2 and Fig. 1.3, is established by Delft3D. Both D-WAVE module in Delft3D and Delft3D-FM are based on the third-generation SWAN. However, D-WAVE and D-FLOW coupling is still not stable in the application by the time of this research. As a result, D-FLOW in Delft3D-FM and D-WAVE in Delft 3D are used separately in this research. Wave model also needs validation before applying it. The input of wind and pressure fields is the same as that in the hydrodynamic model in both validation process and application process. Wave parameters are the output of the wave model and the wave set-up can be estimated from the significant wave height.

The validation of typhoon model is explained in Section 3.2.The set-up and validation of these two models are explained in Section 3.3 and 3.4. The application of climate change events is in Section 4.6 and 4.7.

Failure mechanism

Several failure mechanisms of embankment breaches can be summarized. However, when it comes to the study area, only a few of them are mentioned in this research. Since data of historical breaches and soil conditions are lacking, overtopping is seen as the main failure mechanism. With the output of process ①, ② and the dike dimensions and material, overtopping can be calculated based on GBT51015-2014 Chinese Guideline of Dike Design in process ③ as shown in Fig. 1.2 and Fig. 1.3.

Along the sea dike, several points are set for overtopping calculation. For each point, corresponded water level and wave parameters have already achieved from process ① and ②. Then, the overtopping rate of each point can be summarized to analyze the possible breaching places. The places that experience high overtopping rates are more likely to be breaching places. The threshold of breaching is estimated from the overtopping rate of a historical breaching event.

The broad-crested weir formulas are used to calculate the breach flow discharge, which is the process ④ in Fig. 1.2 and Fig. 1.3. Section 2.9.2 mentioned five stages of breaching process. For the lack of soil information, it is assumed that the stage I-III happens too fast to be involved in the calculation, only stage IV and V are considered in this research.

The parameters of overtopping formula and broad-crested weir formulas used in this research are explained in Section 3.5 and 3.6. In these sections, the overtopping rate is validated and the breaching threshold is estimated. The application of climate change events to this calculation is explained in Section 4.8 and 4.9.

Overland simulation

In this part, represented by the process ⑤ in Fig. 1.2 and Fig. 1.3, Delft3D-FM is used again. Scenarios for different storms are analyzed in this part. With the overtopping volume calculated in process ③ and the breach discharge in process④, the inundation map can finally be achieved. Sensitivity analysis is also made in this part to understand the relative importance of the breach width.

The model set-up of the overland simulation is in Section 3.7.1, and the application of climate change events to this calculation is explained in Section 4.10.

For all the research processes mentioned above, the results of the application of climate change events are presented in Chapter 5.

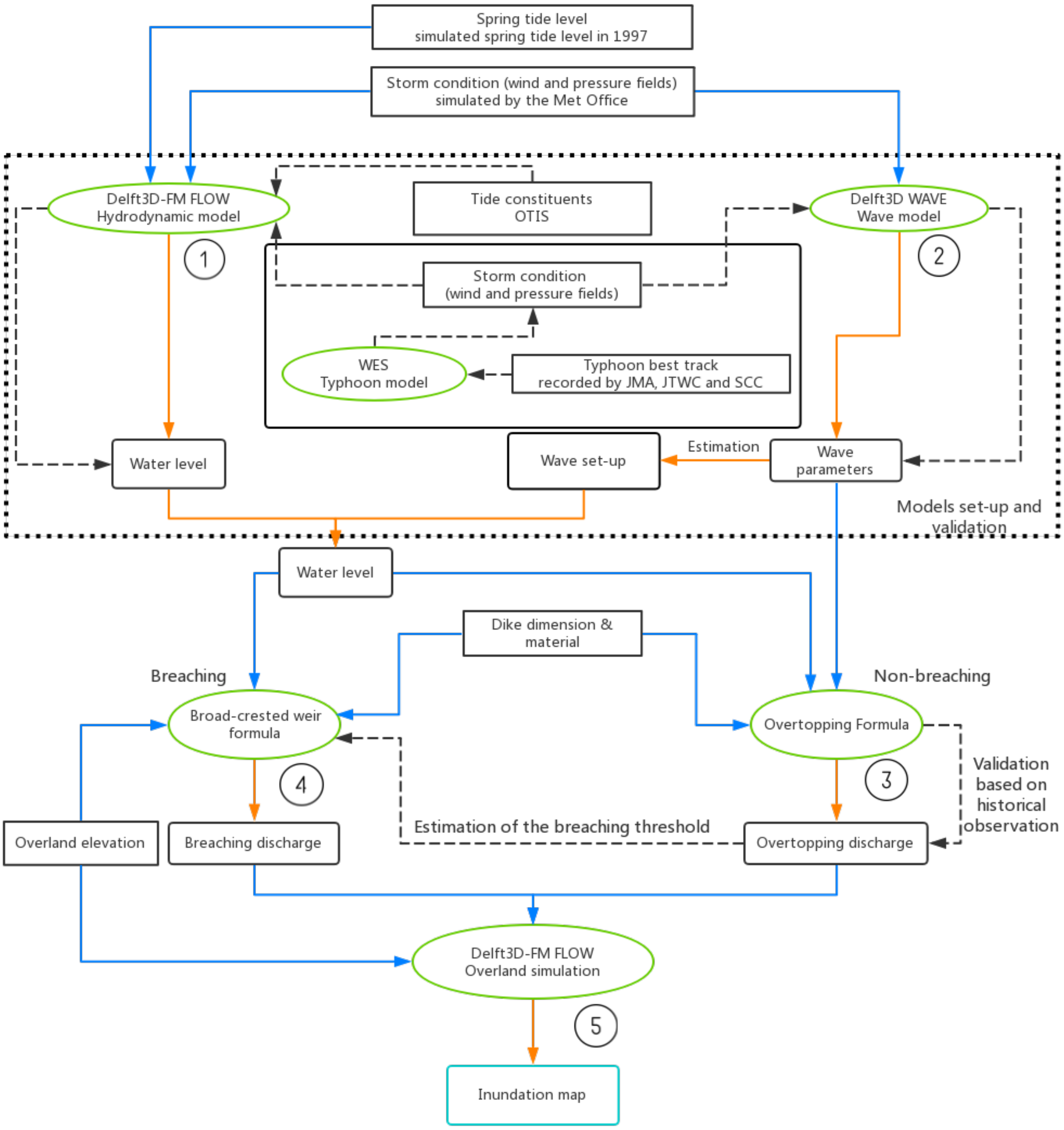

Fig. 1.2.: Flow chart of the main processes in the research. The rectangle represents the input of a model and formula while the rounded rectangle represents the output of the last step, and sometimes it is also the input of the next step. The models and formulas are circled by green ellipses. The blue arrow line ends at a model or formula. The orange arrow ends at the result of a model or formula. The black dash arrow line shows the validation process.

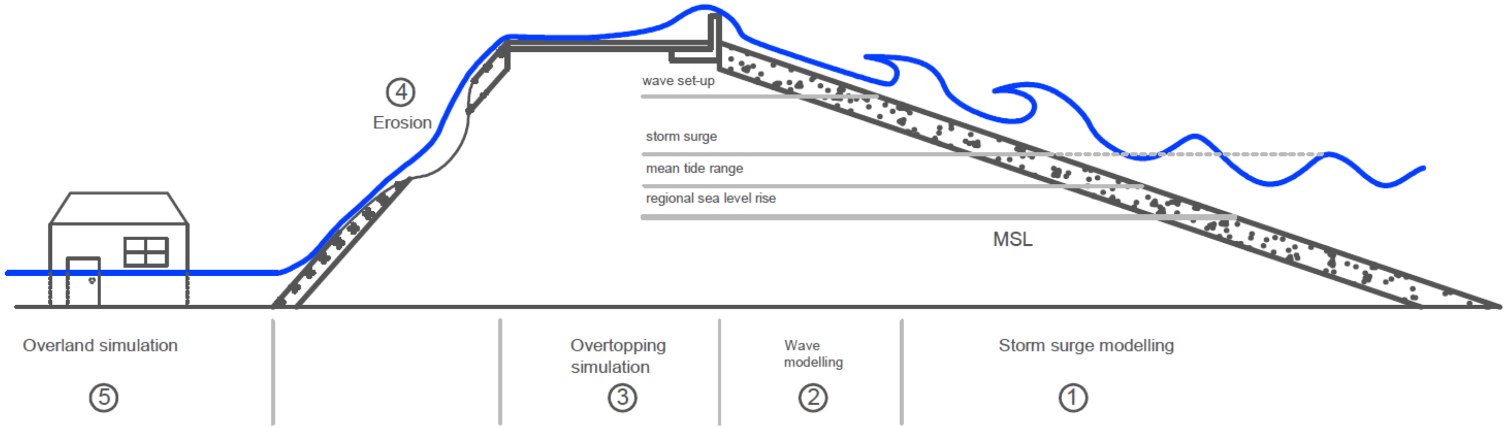

Fig. 1.3.: Schematic diagram of the main processes in the research

1.4 Scope

This research focuses on the effects on inundation conditions resulting from overtopping and breaching of sea embankment in Shanghai from effects of astronomical spring tide, storm and wave, sea level rise and land subsidence.

1.5 Outline

The outline of this research is shown as follows:
Chapter 2: Literature review of the related methods.
Chapter 3: Methodology of model set-up and model validation.
Chapter 4: Model and method application on climate change cases.
Chapter 5: Results of model and method applied to climate change cases.
Chapter 6: Discussion of model results.
Chapter 7: Conclusions and recommendations.

Literature review

2

2.1 Introduction

This chapter gives literature reviews related to this research. It starts with the general introduction of storm surge impacts in Section 2.2. Then, previous studies on Shanghai coastal flood is summarized in Section 2.3. Basic information of the study area, e.g. sea embankments, geographic data, are mentioned in Section 2.4 and 2.5. Section 2.6 gives information of typhoon model used to generate wind and pressure fields. Section 2.7 introduces the software used for the hydrodynamic model, wave model and overland simulation. In Section 2.8 and 2.9, literature review of overtopping and breaching is summarized.

2.2 Storm impacts

2.2.1 Description of tropical cyclone

Tropical cyclone is a severe tropical storm, the maximum sustained wind speed of which equals to or exceeds 33 m/s (Pielke, 1990). Typhoon is a kind of tropical cyclone that mainly happens on the west of North Pacific, while hurricane happens on Atlantic and the east of North Pacific.

Tropical cyclone causes great disasters around the sea and coast on both sides of the equator. The US and China suffer a lot from tropical cyclone attacks. Hurricane is a kind of tropical cyclone generated on Atlantic and eastern Pacific. In August and September 2005, hurricane Katrina closely passed New Orleans, causing the flood defence system to breach. It caused heavy damage with 700 direct casualties, more than 100 billion US $ damage and an enormous social disruption (Kanning et al., 2007).

According to the National standard of tropical cyclones grade (GB/T 19201-2006), tropical cyclones can be divided into six grades as in Tab. 2.1.

Tab. 2.1.: The grade of tropical cyclone (translated from National standard of tropical cyclones grade (2006))

Grade of tropical cyclone	Maximum average wind speed near the center of bottom layer [m/s]	Maximum winds near the center of bottom layer [Beaufort scale]
Tropical depression (TD)	10.8-17.1	6-7
Tropical storm (TS)	17.2-24.4	8-9
Severe tropical storm (STS)	24.5-32.6	10-11
Typhoon (TY)	32.7-41.4	12-13
Severe typhoon (STY)	41.5-50.9	14-15
Super typhoon (SuperTY)	$\geqslant 51.0$	$\geqslant 16$

2.2.2 Historical typhoon effects in Shanghai

As a low-lying city located at Yangtze Estuary, Shanghai suffers from severe typhoon attacks for a long time. In 1949, Typhoon Gloria (No.4906) attacked Shanghai together with astronomical tide. Sea dikes along Chuansha and Nanhui damaged along 40km and completely breached for more than 10 km (Shen, 1997). However, the standard of the sea dikes was quite different from now.

Typhoon Winnie (No. 9711) was the fourth super typhoon in the western North Pacific in 1997. Winnie landed in Zhejiang Province, which is close to Shanghai at 1200 UTC 18 August (Zhang et al., 2005). Winnie caused significant damage in Shanghai. The tide level in Huangpu park rose to 5.72 m, which was the maximum water level in record (Wang, 2019). There was seawater backfilling at Jinshanzui, part of the seawall was washed down over there. At Fengxian, dikes were overtopped at a length of about 22.6 km. Several places along the river flood wall were breached due to heavy rain and strong wind. River flood went into residential areas, hundreds of people were stuck because of the inundation (Wang, 2019; Xu, 2006).

In 2013, during Typhoon Fitow (No.1323), because of the astronomical spring tide and flood from Tai Lake, the tidal level along the Huangpu River in Shanghai has exceeded the warning line. Floodwall at the west bank of Qianbujing breached along 25 m (Zhang et al., 2018).

2.3 Coastal flood in Shanghai

The amount of people living in the low-lying Shanghai area is considerable, and the number is proliferating year by year (Small and Nicholls, 2003). There are many companies and factories situated all round the city, especially along the coast. Any flood inland will bring great danger to people's lives and properties. Due to the importance of Shanghai city safety, there have been already researches focusing on flood in Shanghai.

Floods in Shanghai area from the coast side are mainly generated by typhoons through raising two factors. One is the storm surge, which is the water level raised by the low-pressure centre of a typhoon. The surge can be 0.5 to 1.5 m temporarily, and then it can be amplified up to 2 to 3 m as it moves into the shallow waters within the Yangtze estuary and the Huangpu River (Zong and Chen, 1999). The other is local spring tides. As most typhoons occur during the summer months, the possibility of a storm surge coinciding with a high spring tide is high (Zong and Chen, 1999; Zhou and Liu, 1995).

Yin et al. (2011) tried to forecast the flooding along Shanghai coast in two scenarios: the scenario of sea level rise and storm surge to years 2030 and 2050. The socio-economic impacts are examined by combining the inundation areas with land use and land cover change.

This analysis shows that levee breach inundation mainly occurs in the coastal zones and minimally intrudes inland with the conservative protection of dike systems designed. However, storm surge flooding at the possible maximum tide level could cause nearly total inundation of the landscape.

Wang et al. (2011) used MIKE 21 models to evaluate the overtopping risk of seawalls and levees from the combined effect of land subsidence, storm tide, and sea level rise in Shanghai. In their research, three scenarios were designed to investigate the combined effect of these three hazards. In the result, the overtopping risk of seawalls and levees from the combined disaster effect of the three natural hazards is very high.

As a summary, for the flood threats from the coastal side, storm surge plays a crucial role. When the astronomical spring tide and the typhoon land at the same time, it is likely to raise the water level rapidly in the coastal areas, posing a significant threat to coastal structures. Land subsidence and sea level rise in Shanghai also contribute to the flood. Besides, wave set-up generated by wind-induced-wave during typhoon can also temporarily increase the water level over there. As a result, storm, tide and wind-induced-wave are considered in this research. Once overtopping happens, not only the overtopping volume may result in flood inland, the levees and seawalls are also at the risk of breaching, which will also worsen inundation.

2.4 Sea embankments in Shanghai

2.4.1 Overview of sea embankments in Shanghai

To prevent Shanghai from serious coastal flooding, efforts have already taken by flood defence system, e.g. embankment. Shanghai sea embankments protect highly developed industrial and agricultural areas, so do the most densely populated with tremendous industrial and mining enterprises or essential transportation hub and other vital facilities. The following important areas are protected by the embankment: Shanghai Pudong International Airport, Shanghai Lingang Town, Jinshan Petrochemical Industry Factory and Shanghai chemical industrial park, etc. The embankment failure could lead to catastrophic damage, and it is an urgent task to study how the inland areas are affected by embankment breaching.

The embankment along Shanghai coast was built from 1949 to 1990s. The main structural forms of Shanghai sea embankments are slope type earth-rock dam compound dike and slope type earth-rock dam dike; The body of the embankment is made of pipe and bag ridges filled with mud inside and outside (Chen and Qi, 2010). The outer slope protection structure of sea embankments is mainly composed of fence board or artificial block (mainly including torsion king body and torsion worker body). By the end of 2003, the total length of sea embankment in Shanghai was about 510 km.

In May 2009, the State Council agreed to abolish Shanghai's Nanhui district and merged its this area into Shanghai's Pudong new district. There are different cross-sections for embankments in former Pudong new district and former Nanhui district. To make a clear explanation, embankments in Pudong new district will be divided into three parts in this report. As shown in Fig. 2.1, district A represents the former Pudong new district, district B represents the former Nanhui district from Pudong Airport to Dishui Lake and district C represents the former Nanhui district along the Hangzhou Bay (Zhang et al., 2008). This research focuses on the mainland, so only the following districts are involved: Jinshan, Fengxian, Pudong new district (incl. Former Nanhui), Baoshan.

The embankment in Shanghai can be classified as the main embankment, first-line embankment and preparing embankment. The main embankments play a significant role in protecting Shanghai mainland and islands. The first-line embankments are mainly distributed at the Yangtze River estuary, Eastern Sea and along the coast of Hangzhou Bay. The preparing embankments are the old embankments situated inland under the protection of the main embankment.

Fig. 2.1.: Shanghai sea wall distribution. District A represents the former Pudong new district. District B represents the former Nanhui district from Pudong Airport to Dishui Lake. And District C represents the former Nanhui district along the Hangzhou Bay.

According to the Shanghai seawall plan (1996-2010) (Shanghai Water Resources Bureau, 1996) organized and compiled by the Shanghai Water Authority, strengthening and construction of the sea embankment have been done to improve the ability to prevent a flood. During this plan, the standard revetment project has been constructed at the length of 403 km, beach protection project of 100 km, and renovation project for Neiqingkan of 75 km. In the new Shanghai seawall plan (2011-2020)(Shanghai Water Resources Bureau, 2011), a new standard is putting forward as following: the main embankment at mainland has the standard of high water level at the return period of 200 years and 12 level wind. Chongming Island and Hengsha Island has the standard of high water level at the return period of 100 years and 11 level wind.

Under the measures and plans mentioned above, the probability of storm surge overtopping the sea wall is very low in Shanghai area. However, due to the interaction of sea level rise, land subsidence, coastal estuary erosion and deposition, and seawall subsidence, it is still possible for Shanghai to be affected by storm surge in the future. Therefore, relevant research is urgently needed.

The sea dike dimension is crucial for overtopping and breach discharge calculation. As a result of land subsidence and annual repairs, the sea dike dimensions are different in different locations and different times. In Section 2.4.2, typical cross-sections of sea embankments are discussed. A field work for Shanghai sea embankment was done in September 2019. There are more details about Shanghai sea embankments in Section A.

2.4.2 Typical cross-sections of sea embankments

Shanghai sea embankments have different typical cross-sections in different districts. The following typical cross-sections are collected and translated from Chen and Qi (2010) and these cross-sections are also based on the Shanghai seawall plan (1996-2010) (Shanghai Water Resources Bureau, 1996).

Fig. 2.2 to Fig. 2.7 show sea embankment cross-sections of relevant districts. It is notable that the elevations in these figures are based on Wusong datum.

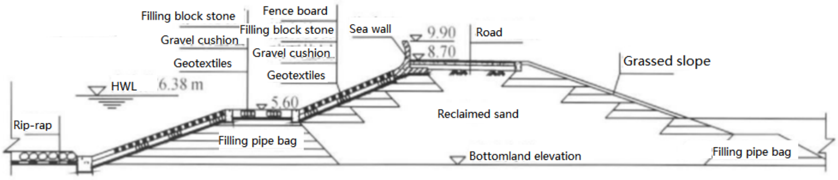

Fig. 2.2.: Typical cross-section of sea embankment in Baoshan district, Wusong datum (translated from Chen and Qi (2010))

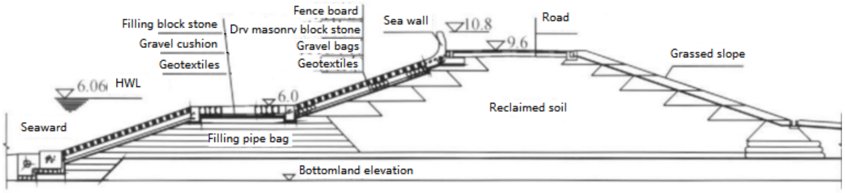

Fig. 2.3.: Typical cross-section of sea embankment in Pudong new district A, Wusong datum (translated from Chen and Qi (2010))

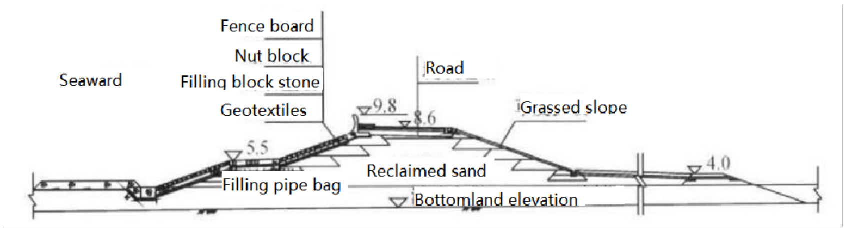

Fig. 2.4.: Typical cross-section of sea embankment in Pudong new district B, Wusong datum (translated from Chen and Qi (2010))

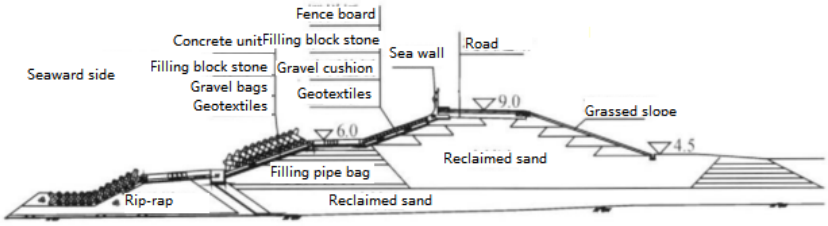

Fig. 2.5.: Typical cross-section of sea embankment in Pudong new district C, Wusong datum (translated from Chen and Qi (2010))

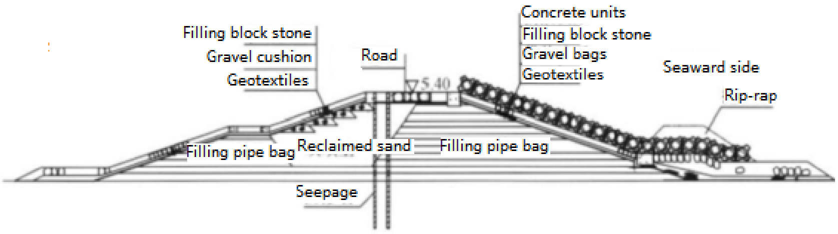

Fig. 2.6.: Typical cross-section of sea embankment in Fengxian district, Wusong datum (translated from Chen and Qi (2010))

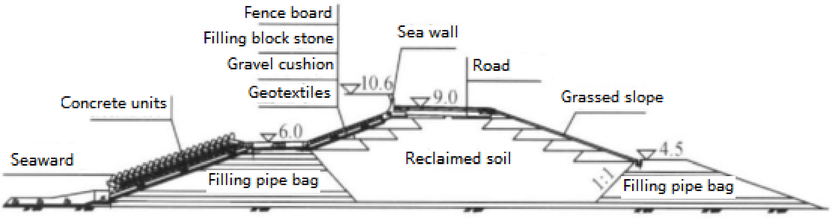

Fig. 2.7.: Typical cross-section of sea embankment in Jinshan district, Wusong datum (translated from Chen and Qi (2010))

2.5 Geographic data in Shanghai

2.5.1 Coordinate system and height datum

All the mentioned large scale geographic data are based on the WGS84 coordinate system. If there is no other explanation, the height datum is based on 1985 national height datum, which uses the perennial mean sea level of the yellow sea in Qingdao as the datum. According to Guo et al. (2004), there is a 35.7 cm vertical shift between the 1985 National Height Datum and the quasigeoid defined by WGS84. According to Wu (2008), the difference between Wusong datum and 1985 national height datum around Shanghai is: Wusong datum=1985 national height datum+1.926 m.

2.5.2 Overland elevation

The overland elevation in Shanghai comes from two parts:

1. Topographic map provided by Shanghai institute of surveying and mapping in 2010.
2. Lidar (Light Detection And Ranging) data in 2010.

2.5.3 Bathymetry for estuary and offshore near Shanghai

The data of bathymetry comes from local refined digitized bathymetry from the nautical chart in 2004 and GEBCO14 Grid (`http://www.gebco.net`).

2.5.4 Regional sea level rise and land subsidence

Land subsidence in Shanghai

The main causes of land subsidence are neotectonic subsidence and anthropogenic subsidence. The neotectonic subsidence rate is 1.5 mm/year in the Yangtze River Delta and adjacent areas (Wang et al., 2012). The anthropogenic subsidences, however, are different in different location and different times. Fig. 2.8 shows the changing rate of anthropogenic subsidence in Shanghai from 1996 to 2007.

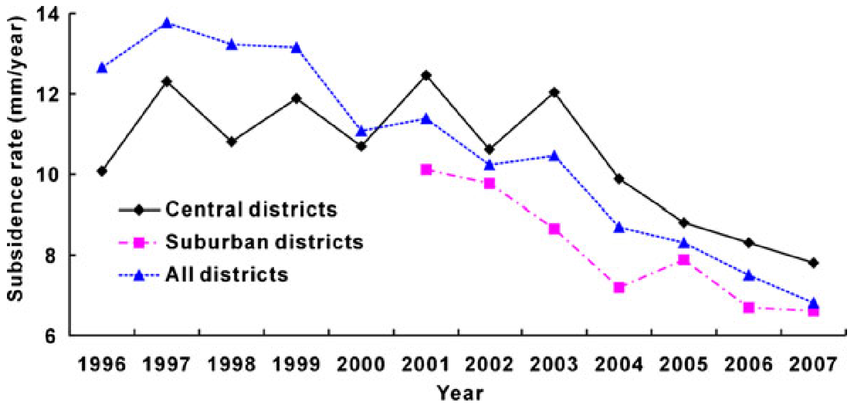

Fig. 2.8.: Change in the rate of anthropogenic subsidence (1996–2007) of Shanghai (Wang et al., 2012)

Sea level rise

Li et al. (1998) studied the historical evolution of sea level rise trend in the past century from 7 tide stations in Shanghai and predicted sea level rise in Shanghai till 2050. Their simulated rates for absolute sea level rises are: 2.0 mm/yr from 1990 to 2010, 2.5 mm/yr from 2011 to 2030 and 5.0 mm/yr from 2031 to 2050. China sea level bulletin (2018) predicted that sea levels along Shanghai coast are expected to rise by 75-155 mm in the following 30 years from 2018. That is 2.5 mm/yr to 5.2 mm/yr from 2018 to 2050. Based on all these references, the applied rates for absolute sea level rises in this research are: 2.5 mm/yr from 2011 to 2030 and 5.0 mm/yr from 2031 to 2100.

2.6 Typhoon model

Typhoon wind and pressure field is a crucial input to reflect typhoon effects in hydrodynamic model and wave. For the validation part in this research, the wind and pressure fields are generated from historical typhoon information by typhoon model.

2.6.1 Review existing typhoon wind and pressure models

Many pieces of research have been made to achieve typhoon wind and pressure in an empirical or semi-empirical way.

The stationary wind field can be calculated by two ways, one is to achieve the wind field directly by the wind parameters like maximum wind speed and radius associated with maximum wind speed. Rankine vortex model is an early application to achieve the wind field; Jelesnianski (1965) put forward typhoon wind model for the need of storm surge calculation. Besides, the wind field can also be generated by the pressure field. In this way, a pressure model is needed. There are some well-known pressure models as follows:

1 Bierknes model (1921)

$$p_a(r) = p_n - \frac{p_n - p_0}{1 + (r/R)^2} \tag{2.1}$$

2 Takahashi model (1939)

$$p_a(r) = p_n - \frac{p_n - p_0}{1 + (r/R)} \tag{2.2}$$

3 Fujita model (1952)

$$p_a(r) = p_n - \frac{p_n - p_0}{\sqrt{1 + (r/R)^2}} \tag{2.3}$$

4 Mayers model (1954)

$$p_a(r) = p_n - (p_n - p_0)(1 - e^{-\frac{R}{r}}) \tag{2.4}$$

5 Jelesnianski model (1965)

$$p_a(r) = \begin{cases} p_n - \frac{3}{4}(p_n - p_0)\frac{R}{r} & r \geqslant R \\ p_0 + \frac{1}{4}(p_n - p_0)(\frac{R}{r})^2 & r < R \end{cases} \tag{2.5}$$

in which: p_n is the environmental (outskirts) atmospheric pressure not affected by the typhoon, [mb]; p_0 is the atmospheric pressure at the center (eye) of the typhoon, [mb]; R is the radius associated with maximum wind speed, [km]; r is the distance from the center of a typhoon, [km].

For a moving typhoon, the wind field can be seen as a sum of two parts: one is the typhoon center movement, the other is the stationary typhoon wind field, which can be driven by the pressure gradient. So the wind speed model can be described as following (Thuy, 2003):

$$\begin{cases} W_x = F_x + W_r x = F cos\phi + C_2 W_r \, cos(90^\circ + \theta + \beta) \\ W_y = F_x + W_r y = F sin\phi + C_2 W_r \, sin(90^\circ + \theta + \beta) \end{cases} \tag{2.6}$$

in which: W_x,W_y are x- (east), - (north) components of the typhoon wind speed at altitude of 10m above sea level, [m/s]; F is the wind speed component related to moving center of typhoon at a distance r from the center of the typhoon, [m/s]; F_x,F_y are x-, y-components of velocity related to moving center of typhoon, [m/s]; W_r is the typhoon gradient wind speed at a distance r from the center of the typhoon, [m/s]; W_{rx},W_{ry} are x-, y-components of typhoon gradient wind speed, [m/s]; θ is the angle between x-axis and the line connecting calculation point and typhoon center, [deg]; β is the angle made by the gradient wind speed with isopiestic line, [deg]; ϕ is the angle between x-axis and typhoon track, [deg]; C_2 is the empirical coefficient in the range of 0.6 to 0.8.

Ke (2018) applied the Holland model (2010) by WES and found that this model is fine to estimate the wind speed at Dajishan with the RMSE of 4.6 m/s.

2.6.2 WES and holland's model

The wind enhawind enhance schemence scheme (WES) was initially developed by the UK Met Office, then improved by Deltares to make the programming results more reliable and consistent. Most of the content in this section is summarized from WES User Manual (2017).

Tropical cyclone winds usually are accounted for in the Numerical Weather Prediction (NWP) data. However, the low resolution of these models cannot make an accurate depiction of wind, which is crucial for hydrodynamic modelling and further inundation deception. The adoption of WES is based on Holland model (Holland, 1980). In that way, the surface wind and pressure fields can be obtained on a high-resolution grid. As an improvement, the asymmetry of observed wind field is introduced by addition of the translatory motion vector of tropical cyclone. It's a good way to overcome the underestimation of wind and pressure in the tropical cyclone from previous models.

In order to synthesis the tropical cyclone wind, a technical method called 'spiderweb' grid is used. Just as its name implies, this kind of grid has a shape of spiderweb, which is actually a polar co-ordinate grid centred on the centre of the tropical cyclone.The tropical cycolne wind and pressure fields are generated on this kind of grid. The 'spiderweb' file is also the input for simulation in DFM and D3D.

Basic equations

According to WES User Manual (2017), the geostrophic wind speed V_g at radius r is calculated following Holland (1980):

$$V_g(r) = \sqrt{\frac{ABp_{drop}exp(-A/r^B)}{\rho r^B} + \frac{r^2 f^2}{4}} - \frac{rf}{2} \tag{2.7}$$

in which: r is distance from the centre of the cyclone, [nmi]; f is Coriolis parameter, [1/s]; ρ is the density of air (assumed to be constant equal to 1.10 kgm^{-3}); $p_{drop} = p_n - p_c$, p_n is the ambient pressure (theoretically at infinite radius, however in this model the average pressure over the model domain is used), p_c is the central pressure, [pa]; A, B are empirical parameters, which will be explained in the following part, [-].

Parameter A determines the relation of the pressure or wind profile relative to the origin, and parameter B defines the shape of the profile.

In the region of maximum winds the Coriolis force is small in comparison to the pressure gradient and centrifugal forces, the cyclostrophic wind V_c at a distance r in this region is given by:

$$V_g(r) = \sqrt{\frac{ABp_{drop}exp(-A/r^B)}{\rho r^B}} \tag{2.8}$$

By setting $dV_c/dr = 0$, the radius of maximum winds R_w can be obtained and is given as follows:

$$R_w = A^{1/B} \tag{2.9}$$

R_w is independent of the relative values of ambient and central pressure and it is defined entirely by the scaling parameters A and B.

With the radius of maximum winds, the maximum wind speed can be computed as:

$$V_{max} = \sqrt{\frac{Bp_{drop}}{\rho e}} \tag{2.10}$$

Tab. 2.2.: Different methods in WES (summarized by WES User Manual (2017))

Method	Known parameters	Equations	Note
1	V_{max}, A and B	2.13 and 2.14	
2	V_{max}, R_{35}, R_{50} and R_{100}	2.7 and 2.9	
3	V_{max}, p_{drop} and R_w	2.11, 2.12 and 2.14	
4	V_{max}, p_{drop}	2.11, 2.12 and 2.14	R_w=25 km
5	V_{max} and R_w	2.11, 2.12 and 2.14	p_{drop} based on empirical model based on US hurricane
6	V_{max} and R_w	2.11, 2.12 and 2.14	p_{drop} based on empirical model for Indian tropical cyclones
7	V_{max}		Not recommended

Parameters A and B can now be expressed as functions of measurable quantities as follows:

$$A = R_w^B \tag{2.11}$$

$$B = \frac{\rho e V_{max}^2}{p_{drop}} \tag{2.12}$$

and the central pressure drop is given by:

$$p_{drop} = \frac{\rho e V_{max}^2}{B} \tag{2.13}$$

With all the equations above, the geostrophic wind V_g can be expressed as function of R_w:

$$V_g(r) = \sqrt{\frac{ABp_{drop}exp(-A/r^B)}{\rho r^B} + \frac{r^2 f^2}{4}} - \frac{rf}{2} \tag{2.14}$$

The equations above are valid for geostrophic winds. Before deriving A and B the wind speed and pressure values are now scaled to their geostrophic values.

Approaches in WES

There are seven methods in WES to compute the wind and pressure. Each method depends on different known parameters and different equations. Tab. 2.2 is a summary for related parameters and equations.

2.7 Delft3D and Delft3D-FM

2.7.1 General introduction of Delft3D and Delft3D-FM

Delft3D Flexible Mesh (Delft3D-FM or DFM) is a hydrodynamic simulation program developed by Deltares. It is a part of Deltares unique, fully integrated computer software suite for a multi-disciplinary approach and 1D, 2D and 3D computations for coastal, river and estuarine areas. It can carry out simulations of flows, waves, water quality and ecology (D-Flow User manual, 2018). Both the hydrodynamic model and overland simulation are based on the D-Flow module in DFM. The grid applied in DFM can be both structured and unstructured.

Actually, there is also a D-Wave module in DFM. However, for some technical problem to the software itself, it is still unachievable for neither standalone wave computation or the D-Wave and D-Flow coupling calculation by the time of this research. So it is hard to achieve the hydrodynamic model and wave model truly offline or online coupling in this research. D-Wave module in Delft3D is used for separate wave calculation.

Delft3D (D3D) is also a hydrodynamic simulation program developed by Deltares. D3D has similar functions as DFM. The apparent difference between D3D and DFM is that the grid in D3D must be structured, which may inaccurately describe the complicated boundary. However, D3D is early developed and is more stable in D-Wave calculation. D-Wave module in D3D is based on the third-generation SWAN model. SWAN is an acronym for Simulating WAves Nearshore. SWAN computes wave propagation, wave generation by wind, non-linear wave-wave interactions and dissipation, for a given bottom topography, wind field, water level and current field in waters of deep, intermediate and finite depth (Delft3D-Wave Manual, 2014).

2.7.2 Flow model

Basic equations in D-Flow

According to D-Flow User manual (2018), the hydrodynamics model is simulated by solving the system of two-dimensional of shallow water equations that consist of two horizontal momentum equations and one continuity equation.

Many assumptions have been made in D-FLOW FM. Two crucial assumptions are:

1 Hydrostatic pressure assumption: Vertical accelerations are assumed to be small compared to the gravitational acceleration and are therefore not taken into account.

2 Boussinesq approximation: The effect of variable density is only taken into account in the pressure term.

The depth and density averaged continuity equation is given by:

$$\frac{\partial h}{\partial t} + \frac{\partial Uh}{\partial x} + \frac{\partial Vh}{\partial y} = Q \tag{2.15}$$

in which: U and V are the depth averaged velocities, [m/s]; h is the water level above a reference level, [m]; Q represents the contributions per unit area due to the discharge or withdrawal of water, precipitation and evaporation, [m/s]. Actually, precipitation and evaporation are not included in this research.

The momentum equations in x- and y-direction are given by:

$$\frac{\partial u}{\partial t} + u\frac{\partial u}{\partial x} + v\frac{\partial u}{\partial y} + w\frac{\partial u}{\partial z} - fv = -\frac{1}{\rho_0}\frac{\partial P}{\partial x} + F_x + \frac{\partial}{\partial z}(\nu_v \frac{\partial u}{\partial z}) + M_x \tag{2.16}$$

$$\frac{\partial u}{\partial t} + u\frac{\partial v}{\partial x} + v\frac{\partial v}{\partial y} + w\frac{\partial v}{\partial z} + fu = -\frac{1}{\rho_0}\frac{\partial P}{\partial y} + F_y + \frac{\partial}{\partial z}(\nu_v \frac{\partial v}{\partial z}) + M_y \tag{2.17}$$

in which: u, v and w are the velocity components in the horizontal x, y and vertical z directions respectively, [m/s]; f is Coriolis parameter, [1/s]; ν_v is the vertical eddy viscosity coefficient, [m^2/s]; $\frac{\partial P}{\partial x}$ and $\frac{\partial P}{\partial y}$ represent the pressure gradients; The forces F_x and F_y represent the unbalance of horizontal Reynolds stresses; M_x and M_y represent the contributions due to external sources or sinks of momentum;

Wind

The wind shear stress is calculated by the widely used quadratic expression, according to D-Flow User manual, 2018):

$$|\tau_w| = \rho_a \, C_d \, W^2 \tag{2.18}$$

in which: ρ_a is air density, [kg/m^3]; C_d is the wind drag coefficient, [-]; W is wind speed at 10 m above the free surface, [m/s].

In Delft3D-FM, except for a constant drag coefficient, there are three concepts that can be chosen (Deltares, 2018):

1 Smith and Banke (1975)

$$10^3 C_d = 0.63 + 0.066W \pm 0.23 \tag{2.19}$$

When Smith and Banke's type is used, the wind drag is considered as dependent on the wind speed in a piecewise linear way, see Fig 2.9. In this figure, breakpoints ABC refer to three sets of coordinates, specifying a piecewise linear dependency for two ranges of wind speeds.

2 Charnock (1955)

$u_*$is the friction velocity, and $\tau \equiv \rho u_*^2$. For the wind speed at height z,

$$\frac{u}{u_*} = \frac{1}{\kappa} log \frac{z}{z_0} \tag{2.20}$$

in which: κ is the von Karman's constant, logz(0) is the intercept on the log z axis.

3 Hwang (2005)

$$C_d = [\frac{1}{\kappa} ln(\frac{\pi}{z_{0*}} \omega_{**}^2)]^{-2} \tag{2.21}$$

in which: κ is the von Karman's constant; $\omega_{**} = \omega_p u_* / g$ is a dimensionless frequency; $z_{0*} = g z_0 / u_*^2$ is the Charnock parameter.

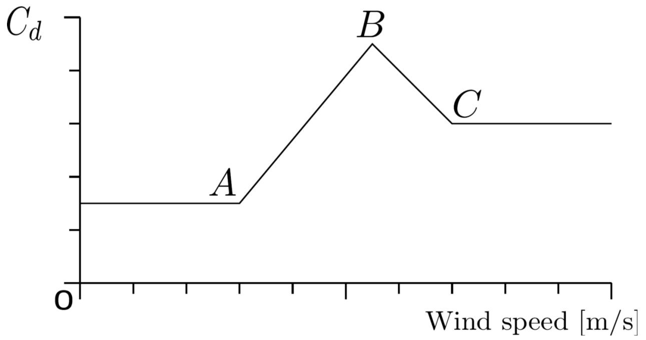

Fig. 2.9.: Relation between wind drag coefficient and the wind speed based on Smith and Banke type formular (D-Flow User manual, 2018)

Among these three concepts, the concept of Smith and Banke is used in this research by the suggestion of Ke (2018). The value of wind drag coefficient at ABC points are depended on Zijlema's adaptation (Zijlema et al., 2012):

$$C_D = (0.55 + 2.97\tilde{U} - 1.489\tilde{U}^2) \times 10^{-3} \tag{2.22}$$

in which:$\tilde{U} = U_{10}/U_{ref}$; $U_{ref} = 31.5$ m/s. Wind speed achieves the highest value at U_{ref}

2.7.3 Wave model

Basic equations in SWAN

According to D-Wave manual (2014), the evolution of the wave spectrum is described by the spectral action balance equation, which for Cartesian co-ordinates is:

$$\frac{\partial}{\partial t}N + \frac{\partial}{\partial x}c_x\,N + \frac{\partial}{\partial y}c_y\,N + \frac{\partial}{\partial \sigma}c_\sigma\,N + \frac{\partial}{\partial \theta}c_\theta\,N = \frac{S}{\sigma} \tag{2.23}$$

And in SWAN Scientific and Technical Documentation (2019), the equation for spherical coordinates (with longitude,λ and latitude,φ) is:

$$\frac{\partial}{\partial t}N + \frac{\partial}{\partial \lambda}c_\lambda\,N + (cos\varphi)^{-1}\frac{\partial}{\partial \varphi}c_\varphi\,(cos\varphi)\,N + \frac{\partial}{\partial \sigma}c_\sigma\,N + \frac{\partial}{\partial \theta}c_\theta\,N = \frac{S}{\sigma} \tag{2.24}$$

According to D-Wave manual (2014), the first term in the left-hand side of represents the local rate of change of action density in time, and the second and third term represent the propagation of action in geographical space. The fourth term represents shifting of the relative frequency due to variations in depths and currents. The fifth term represents depth-induced and current-induced refraction. On the right side of this equation is the source term, which is contributed by 6 processes, according to SWAN Scientific and Technical Documentation (2019):

$$S = S_{in} + S_{nl3} + S_{nl4} + S_{wc} + S_{bfr} + S_{br} \tag{2.25}$$

On the right hand side, the first term represents generation by wind. Wave-wave interaction terms follow behind, with the second term representing triad wave-wave interaction and the third term representing quadruplet wave-wave interaction. The fourth, fifth and sixth term on the right hand side represent dissipation by means of whitecapping, bottom friction and depth-induced wave breaking respectively.

Wind

The source term S_{in} represents wave growth by wind. S_{in} exists of a linear part A and a exponential part $BE(\sigma, \theta)$:

$$S_{in} = A + BE(\sigma, \theta) \tag{2.26}$$

in which A and B depend on wave frequency and direction, and wind speed and direction. The linear growth term A is basically used for initial wind growth (Cavaleri and Rizzoli, 1981). For the coefficient B, there are two options in SWAN. One comes from Komen et al. (1984), the other is based on Janssen (1991).

The wind speed U_{10} used in SWAN is at an elevation of $10m$. And the friction velocity U_* can be calculated by:

$$U_*^2 = C_D U_{10}^2 \tag{2.27}$$

Recently, the wind drag coefficient is also formulated according to Zijlema et al. (2012) as in Eq. 2.22

Bottom friction

Bottom friction in SWAN is modelled with:

$$S_{bfr}(\sigma, \theta) = -\frac{C_{bfr}}{g}[\frac{\sigma}{sinh(kd)}]^2 E(\sigma, \theta) \tag{2.28}$$

in which C_{bfr} is the bottom friction coefficient, which depends on the root-mean-square orbital velocity at the bottom $u_{rms,bottom}$.

SWAN provides three options to calculate the bottom friction coefficient, according to JONSWAP, Collins or Madsen.

For the mentioned two source terms and other source terms S_{nl3}, S_{nl4}, S_{wc} and S_{br}, there are detailed explanation in D-Wave manual (2014) and SWAN Scientific and Technical Documentation (2019).

Wave-induced set-up

According to SWAN Scientific and Technical Documentation (2019), the wave-induced currents are mainly driven by the divergence-free part of the wave forces whereas the set-up is mainly due to the rotation-free part of these forces (Dingemans et al., 1987). In the 2D case the computation of the wave-induced set-up is based on a momentum balance equation which is a balance between the wave force and the hydrostatic pressure gradient.

$$\frac{\partial F_x}{\partial x} + \frac{\partial F_y}{\partial y} - \frac{\partial}{\partial x}(\rho g H \frac{\partial \bar{\eta}}{\partial x}) - \frac{\partial}{\partial y}(\rho g H \frac{\partial \bar{\eta}}{\partial y}) = 0 \tag{2.29}$$

in which: $\bar{\eta}$ is the mean surface elevation (including the wave-induced set-up), [m].

Eq.2.29 is only applied to Cartesian coordinates, so that in this research, the wave set-up calculation cannot be applied to spherical model correctly. The wave set-up is estimated by a simple model provided by the lecture not of Coastal Dynamics I (Bosboom and Stive, 2015), using a simple dissipation model and assuming long-crested wave normally incident to straight and parallel depth contours. It is assumed that, wave height everywhere in the suffer zone, $H = \gamma h$. H is the wave height, [m]; γ is the wave breaking index, [-] and h is the water depth, [m]. The water level difference ($\Delta\bar{\eta}$) between the breaker line and the point of maximum water level rise (wave set-up) is:

$$\Delta\bar{\eta} = \frac{3}{8}\gamma H_b \tag{2.30}$$

in which γ is the wave breaking index(H_b/h_b), [-]; H_b is the wave height at point of breaking, [m]; h_b is the still water depth at point of breaking, [m].

However, in storm cases, the waves are irregular. Application of wave set-up calculation above is not proper. Feng et al. (2011) reported that reflected by maximum significant wave height of 12 m nearshore, there was a maximum 0.55 m wave set-up at the coast during Typhoon Saomai, ranging from $21°$N to $30°$N and from $116°$E to $128°$E. Yamanaka et al. (2020) applied 5% of the local significant wave height as the wave set-up and present reasonable agreement with the observed tide level.

2.8 Overtopping

2.8.1 Description of overtopping

Wave overtopping is the average discharge per linear meter of width, usually in m^3/s per m or l/s per m . Wave overtopping matters a lot on the dike stability and safety. Plenty of researches have been done all around the world.

Wave Overtopping of Sea Defences Structures and Related Structures Assessment Manual (EurOtop, 2016) is a manual on wave overtopping of sea defences and related structures based mainly on European research, but is applied worldwide. The method considers the effects of berm, revetment roughness, wave incident angle, sea wall etc. A more detailed introduction of this method is in Section 2.8.2. Chen et al. (2010) proposed the calculation formula of the average overrunning amount of irregular waves through the physical model test.

Every method has its own range of application. Chinese overtopping formula based on GBT51015-2014 Chinese Guideline of Dike Design is applied in this research.

2.8.2 Overtopping calculations

Chinese standard of overtopping calculation

The Chinese overtopping formula is based on GBT51015-2014 Chinese Guideline of Dike Design (2014). Some explanations for the parameters are shown in Fig 2.10.

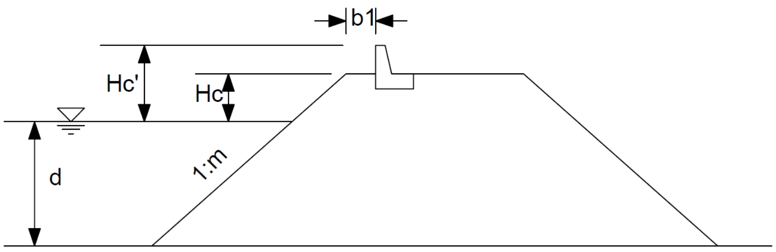

Fig. 2.10.: Sea embankment with seawall (Chinese Guideline of Dike Design, 2014)

Tab. 2.3.: Empirical parameter B (Chinese Guideline of Dike Design, 2014)

m	1.5	2.0	3.0
B	0.60	0.45	0.38

Tab. 2.4.: Empirical parameter K_A (Chinese Guideline of Dike Design, 2014)

Reventment	concrete slab	rip-rap	dolos	hollow squre
K_A	1.00	0.49	0.40	0.50

And the overtopping discharge Q (m^3/m/s) is calculated as (Chinese Guideline of Dike Design, 2014):

$$Q = 0.07^{\frac{H_c'}{H_{m0}}} exp(0.5 - \frac{b_1}{2H_{m0}}) B K_A \frac{H_{m0}^2}{T_p}[\frac{0.3}{\sqrt{m}} + th(\frac{d}{H_{m0}} - 2.8)^2] ln\sqrt{\frac{gT_p^2 m}{2\pi H_{m0}}} \tag{2.31}$$

in which:d is the water depth at the toe, [m]; Hc' is the crown wall freeboard, [m]; Hc is the crest freeboard, [m]; b_1 is the distance between the crest edge and the crown wall, [m]; m is the reciprocal of the slope angle, [-]; B is an empirical parameter which can be ensured by Tab. 2.3, [-]; K_A is an influence factor for roughness on the slope, which can be ensured by Tab. 2.4, [-]; H_{m0} is the incident significant wave height, [m]; T_p is the peak period, [s].

EurOtop calculation

Based on EurOtop (2016), the general formula for the average overtopping discharge on a slope (dike, levee, embankment) are given by the mean value approach, which should not be used for design and assessments:

$$\frac{q}{\sqrt{gH_{m0}^3}} = \frac{0.0023}{\sqrt{tan\alpha}} \gamma_b \xi_{m-1,0} exp[-(2.7 \frac{R_c}{\xi_{m-1,0} H_{m0} \gamma_b \gamma_f \gamma_\beta \gamma_v})^{1.3}] \tag{2.32}$$

with a maximum of

$$\frac{q}{\sqrt{gH_{m0}^3}} = 0.09 exp[-(1.5 \frac{R_c}{H_{m0} \gamma_f \gamma_\beta \gamma_*})^{1.3}] \tag{2.33}$$

in which: γ_b is the influence factor for a berm, [-], γ_f is the influence factor for roughness elements on a slope, [-], γ_β is the influence factor for oblique wave attack, [-], γ_v is the influence factor for a wall at the end of a slope, [-] and γ_* is a combined factor of all kind of geometrical influences, [-].

For a design or assessment approach it is strongly recommended to increase the average discharge by about one standard deviation:

$$\frac{q}{\sqrt{gH_{m0}^3}} = \frac{0.026}{\sqrt{tan\alpha}}\gamma_b\xi_{m-1,0}exp[-(2.5\frac{R_c}{\xi_{m-1,0}H_{m0}\gamma_b\gamma_f\gamma_\beta\gamma_v})^{1.3}] \tag{2.34}$$

with a maximum of

$$\frac{q}{\sqrt{gH_{m0}^3}} = 0.1035exp[-(1.35\frac{R_c}{H_{m0}\gamma_f\gamma_\beta\gamma_*})^{1.3}] \tag{2.35}$$

2.8.3 Tolerable overtopping limits

According to GBT51015-2014 Chinese Guideline of Dike Design, the tolerable overtopping rate should follow the standard in Tab. 2.5 in design cases.

Tab. 2.5.: Tolerable overtopping rate (translated from Chinese Guideline of Dike Design (2014))

Reventment	Tolerable overtopping rate [m^3/m/s]
The crest and the rear side are placed with 30cm dry masonry block	$\leqslant 0.01$
The crest is covered with concrete and the rear side is covered with well-grown grasses	$\leqslant 0.01$
The crest is covered with concrete and the rear side is covered with 30cm dry masonry block	$\leqslant 0.02$
The crest, the front side and the rear side are well protected, the crest and the rear side are protected with concrete	$\leqslant 0.05$

Other countries like the US, Japan, England, the Netherlands, etc. also have their own standard for tolerable overtopping rate with their own descriptions. Tab. 2.6 shows the wave overtopping limits in EurOtop (2016).

2.9 Failure mechanism of sea dike

2.9.1 Introduction

Flood defences are used worldwide to prevent inland from flooding. Once a flood defence fails, catastrophic consequences may happen. Several failure mechanisms

Tab. 2.6.: Limits for wave overtopping for structural design of breakwaters, seawalls, dikes and dams (EurOtop, 2016)

Hazard type and reason	Mean discharge q [l/s per m]	Max volume Vmax [l per m]
Rubble mound breakwaters; Hm0 >5 m; no damage	1	2,000-3,000
Rubble mound breakwaters; Hm0 >5 m; rear side designed for wave overtopping	5-10	10,000-20,000
Grass covered crest and landward slope; maintained and closed grass cover; Hm0 = 1 – 3 m	5	2,000-3,000
Grass covered crest and landward slope; not maintained grass cover, open spots, moss, bare patches; Hm0 = 0.5 – 3 m	0.1	500
Grass covered crest and landward slope; Hm0 <1 m	5-10	500
Grass covered crest and landward slope; Hm0 <0.3 m	No limit	No limit

may lead to failure of flood control systems. Fig. 2.11 shows possible failure mechanisms according to the lecture note of the course Flood Defences of TU Delft (Jonkman et al., 2017).

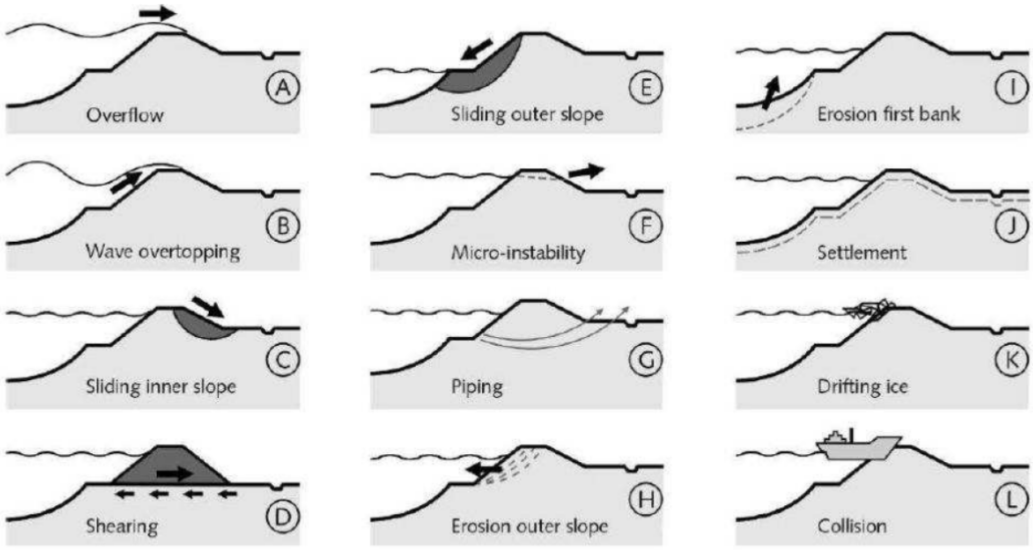

Fig. 2.11.: Possible failure mechanisms for an earthen dike (Jonkman et al., 2017)

2.9.2 Breaching process

The breach evolution process in sand dikes can be generally divided into five stages (Visser, 1998):

In Stage I ($t_0 < t \leqslant t_1$), the overtopping flow lowers the dike crest in the breach, and the dike inner slope in the channel is steepened until a certain critical angle β_1 arrives at $t = t_1$. β_1 is dependent upon the dike material properties. And in Stages II ($t_1 < t \leqslant t_2$), retrograde erosion of the inner slope happens at a constant angle, yielding a decrease of the width of the crest of the dike in the breach. At the end of this stage, the crest vanishes and the breach inflow starts to increase. In Stages III ($t_2 < t \leqslant t_3$), the top of the dike in the breach keep lowering with a constant angle of the breach side slopes and equal to the critical value γ, increasing of the width of the breach. At the end of this stage, dike in the breach is completely washed out down to the base of the dike at polder level.

For the last two stages (i.e. Stages IV and V,$t_3 < t \leqslant t_5$), the breach width increases markedly due to the continuous flow shear erosion and the discrete mass failure from the breach side slopes. The extent of vertical erosion in these two stages depends mainly on the geometrical and material conditions of the dike.

According to Visser (1998), there are three types of breaches distinguished by different geometrical and material conditions. When the vertical erosion at the breach inflow is prevented or extremely slowed down by a solid dike foundation, or by solid toe protection on the dike outer slope, or by a solid and relatively high foreland, or by an effective bottom protection on the foreland, a Type A breach (shown in Fig. 2.12) takes place. Solid here means high erosion resistant. A dike breaches as Type B when only a relatively high but erodible foreland is present. All the other cases belong to Type C breaches.

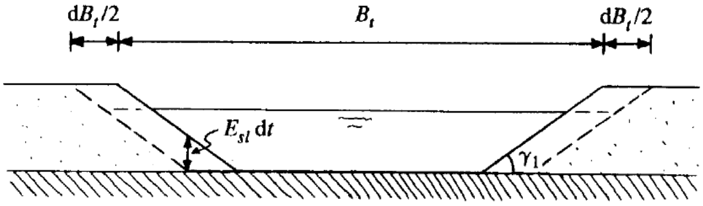

Fig. 2.12.: Breach width increase in Stages IV and V in a Type A breach (Visser, 1998)

For the clay dikes, the erosion process is similar as shown in Fig. 2.13.

2.9.3 Mathematical model

Based on the five-stage breach erosion process outlined above, a mathematical model has been developed for the growth of a breach in sand dikes.

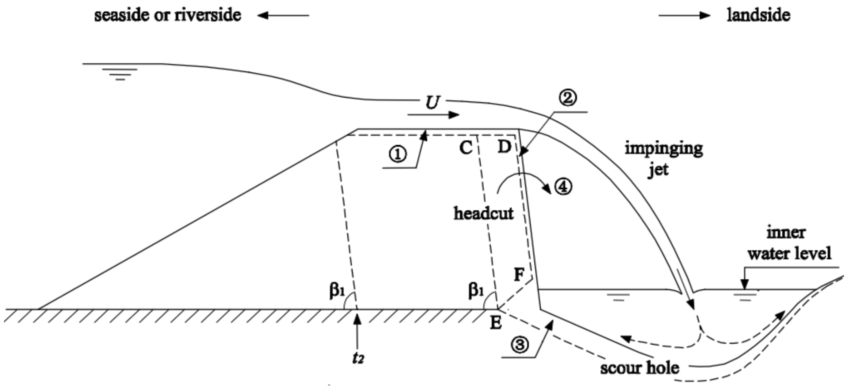

Fig. 2.13.: Erosion at the headcut in Stages II and III: (1) shear erosion along headcut top surface; (2) shear erosion along headcut slope; (3) dike foundation jet scour and headcut undercutting and (4) headcut slope mass wasting (Zhu et al., 2006)

The breach flow discharge is calculated with the broad-crested weir formulae as follows (Visser, 1998):

$$Q_{br} = m(\frac{2}{3})^{3/2}\sqrt{g}B(H_w - Z_{br})^{3/2} \qquad for \quad t_0 < t \leqslant t_4 \tag{2.36}$$

$$Q_{br} = m\sqrt{2g}B(H_w - H_p)^{1/2}(H_p - Z_{br}) \qquad for \quad t_4 < t \leqslant t_5 \tag{2.37}$$

in which Q_{br} is the flow discharge through the breach, [m^3/s]; m is the discharge coefficient, which is 1 for type A and approximate $\pi/2$ for type B and C, [-]; g is the gravity acceleration, [m/s^2]; B is the averaged breach width over water depth, [m]; H_w is the outer water level, i.e. water level of the river or sea, [m]; Z_br is the height of the breach bottom, [m]; and H_p is the water level in the polder behind the dike, [m].

2.9.4 Relation between overtopping and breaching

There is no official standard for breaching. According to Chinese Guideline of Dike Design, only the tolerable overtopping in design is stipulated (see Tab. 2.5). This standard is only applied in the design stage, and it doesn't mean that overtopping rate larger than it can directly lead to dike breaches. For an accurate threshold of sea dike breach, additional researches are needed, including large-scale model experiments and prototype measurements.

Zhang et al. (2017) made a physical model experiment on sea dike breaching. The dike is made of standard material of real sea dikes in China. The baseline generalized section is also similar to sea dikes in Shanghai (shown in Fig. 2.14). They found that most of the sea dikes will be completely unstable and then breached within the overtopping range of 0.117 to 0.424 $m^3/m/s$. For the rear slope of 1:3, they measured the failure overtopping rates between 0.263-0.305 $m^3/m/s$ for concrete revetment and 0.105-0.117 $m^3/m/s$ for dry masonry block revetment. Moreover, dike with 1 m sea wall are found to have a lower failure overtopping rate, 35% and 18% decreases for concrete and dry masonry block revetment respectively.

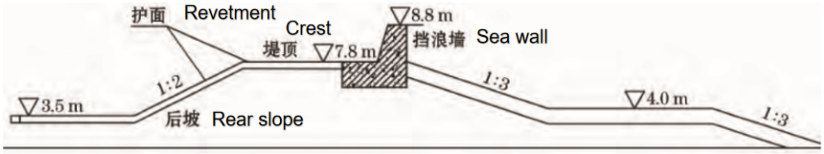

Fig. 2.14.: Baseline generalized section (translated from Zhang et al. (2017))

2.10 Summary

This chapter gives the literature review on different aspects in this research, including the necessary information of the study area and the references of the methods. In the next chapter, the methods used in this research are explained in detailed based on the literature review mentioned in this chapter.

Methods and model validation

3

3.1 Introduction

In this chapter, the approach and methodology of this research are explained in details. To prove the reliability of the simulation process, validation of each part is needed. However, for the lack of measurement data, only the hydrodynamic model and wave model can be validated.

A hydrodynamic model and a wave model are established by Delft3D-FM and Delft3D, respectively. Validations should be made to these models to make sure the resulting water level and wave parameters reliable for the next step. The validations are based on historical events. The wind and pressure fields of the historical events are generated from storm track by WES. To apply reliable wind and pressure fields, validation is also needed for the typhoon model.

Overtopping is seen as the main cause of dike breaching. Several points are set for overtopping and breach discharge calculations along the coastline. The places where experience high overtopping are more likely to be the breaching places. A threshold of breaching is also estimated based on reference and historical observation.

An overland simulation is established by Delft3D-FM for Shanghai city. The overtopping discharge and breach discharge are the input of the overland simulation, resulting in inundation in the study area.

3.2 Typhoon model

3.2.1 Introduction

Typhoon wind and pressure fields are crucial to reflect typhoon effects in hydrodynamic model and wave model. During the processes of hydrodynamic model and wave model validations, the wind and pressure fields are based on historical typhoon track information. This kind of wind and pressure field needs validation.

3.2.2 Typhoon track data

Typhoon track information is used in this research to simulate wind and pressure field during historical typhoon events for the hydrodynamic models validation.

The Joint Typhoon Warning Center (JTWC, `https://www.metoc.navy.mil/jtwc/jtwc.html?western-pacific`) has records of typhoons from 1945, the so-called Western North Pacific Ocean Best Track Data. Japan Meteorological Agency (JMA, `https://www.jma.go.jp/jma/jma-eng/jma-center/rsmc-hp-pub-eg/besttrack.html`) has typhoon records from 1989. Both of these two sources usually consist of information of time, position, typhoon centre pressure (P_c), maximum sustained wind speed (V_{max}) every 6 hours. For early years, some of the information mentioned above wasn't recorded. For JMA, radius of R_{50} and R_{35} every 6 hours are also recorded. R_{50} refers to the radius of 50 kt winds or greater, while R_{35} refers to the radius of 35 kt winds or greater according to the explanation from JMA.

Besides, Shanghai Climate Center (SCC) also provides useful information on typhoon tracks in this research. The information on track also consists of time, position, typhoon centre pressure and maximum sustained wind speed every 6 hours.

3.2.3 Validation of the wind model

Data sources

Shanghai Water Authority (`http://bmfw.swj.sh.gov.cn/`) provides records of wind speed and direction at Luchaogang with an interval of 5 min during Typhoon Lekima in 2019. Typhoon Lekima was the strongest typhoon in China since 2019. The following validation for wind field is depended on Typhoon Lekima.

According to the information from China Meteorological Administration (`http://www.cma.gov.cn`), Typhoon Lekima was born on 4 August, 2019 as the ninth typhoon in the Pacific typhoon season. Lekima upgraded to super typhoon on 7 August and landed Zhejiang coast on 10 August. The wind velocity of 52 m/s made Lekima the strongest storm in China since 2019. Then it moved across Zhejiang and Jiangsu Provinces and entered Yellow Sea. On 11 August, it landed again in Shandong Province and moved into Bohai Sea and weaken afterwards. On the morning of the 13 August, Lekima weakened to a tropical depression. For the same day, the central meteorological station stopped numbering it.

Input parameters and method chosen

As mentioned in Section 2.6.2, V_{max}, P_{drop} and R_{max} are the three essential elements for method decision in WES. For the typhoon track from JMA, V_{max} is given, P_{drop} can be calculated by $P_{drop} = P_n - P_c$, as the ambient pressure P_n is assumed to be 1015 hpa and typhoon center pressure P_c is given. R_{max} can be calculated by an empirical equation $R_{max} = 0.23R_{50}$ from Tagaki model (Takagi and Wu, 2016). For that JMA gives the longest radius of 50 kt winds or greater as well as the shortest radius of 50 kt winds or greater, R_{50} takes the average value of theses two in this case. With V_{max}, P_{drop} and R_{max} known, method 3 can be applied and method 4 can also be applied only using V_{max} and P_{drop}. Method 3 can only be applied when the values of all three parameters are provided. According to the record by JMA, R_{50} is only recorded from 6000 UTC 6 August to 0000 UTC 10 August. It means R_{max} can only be computed in this period, which is much shorter than the actual typhoon period. So method 3 cannot provide a complete wind field or pressure field for the whole typhoon period in this case. Method 4 is then chosen for the provided JMA data during Typhoon Lekima. After applying method 4 in WES, the modelled wind velocity and direction can be achieved.

Wind field validation results

The selected part of record for Typhoon Lekima consists information of wind speed and wind direction every 5 min from 1200 Beijing Standard Time (BST, be equal to UTC+08 hr) 4 August to 0000 BST 12 August. The location of the observation point is at Luchaogang, which is a port situated on the east part along Hangzhou Bay. The blue dots in Fig 3.1 and Fig 3.2 show the wind speed and wind during this period respectively. For the wind velocity, the error (RMSE) is 3.7 m/s for this period, which is lower than the RMSE of 4.6 m/s in Dajishan in 1997 validated by Ke (2018). The model overestimates the wind velocity around the top values, which is acceptable for safety reasons. For the wind direction, the modelled direction is larger in some dates and the error (RMSE) is 42.2 degrees. The total tendency fit well for both figures.

3.3 Hydrodynamic model

In this research, the hydrodynamic model is established by Delft3D-FM. It simulates both the water level raised by the low-pressure centre of a typhoon and the possible

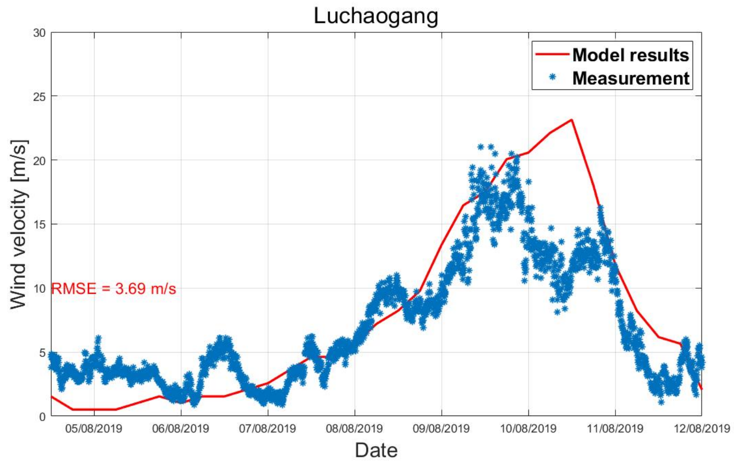

Fig. 3.1.: Wind speed at Luchaogang during Lekima

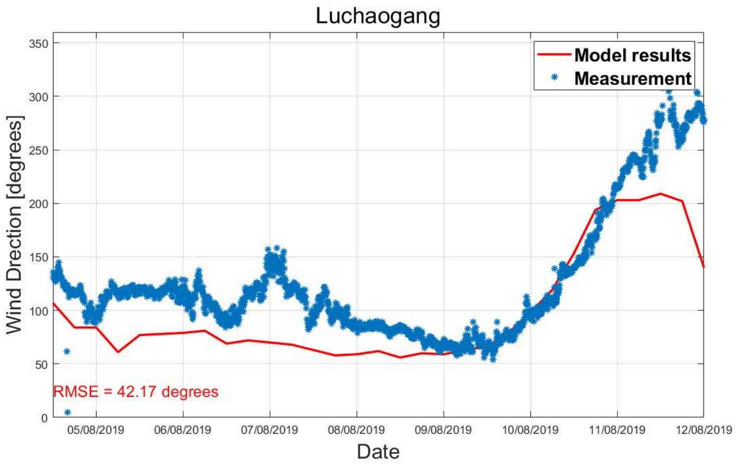

Fig. 3.2.: Wind direction at Luchaogang during Lekima

coinciding high spring tide. In this section, the hydrodynamic model is set up and then calibrated and validated depending on records of several historical typhoon events.

3.3.1 Model set-up

The domain area and computational grids

The domain area of the model covers part of East China Sea, Hangzhou Bay, Yangtze Estuary and downstream Yangtze River, roughly ranging from 24°N to 34°N and 118°E to 120°E. With the coordinate system of WGS84, the flexible mesh (see

Fig. 3.3) is made up of unstructured grids, including curvilinear and triangle grids with a total number of 68,731.

Boundary condition

This model contains five boundaries. One of them is located at Datong Station ($30.82°$N, $117.54°$E, shown in Fig 3.3, B4), which gives information about discharge in the Yangtze River. With the shape of lines, the other four boundaries (shown in Fig. 3.3, B1, B2, B3 and B5) are open boundaries at the sea side. Tide information is provided along these four open boundaries. In the validation part, the regional tide information is collected from OTIS (`http://www.coas.oregonstate.edu/research/po/research/tide/index.html`, Oregon State University Tidal Inversion Software) and are applied to the model in the form of tide constitutes. Besides tide constitutes, tide can also be applied at the boundaries as the form of tide amplitudes and phases along the time.

The detailed names and locations of points on these boundaries are provided in Appendix B in Fig. B.1 and in Tab. B.1.

Bathymetry

The data of bathymetry comes from the digitized local nautical chart in 2004 and GEBCO14 Grid (`http://www.gebco.net`). However, since there is some dredging work at the estuary and erosion of the Delta since the Three Gorges Dam was completed, the bathymetry may be different at sometimes. This will be considered for calibration to get a more reliable bathymetry for the model.

Wind drag coefficient

As explained in Section 2.7.2, the concept of Smith and Banke (1975) is used in this research as the conception of wind drag coefficient by the suggestion of Ke (2018). The set of the wind drag coefficient at ABC points depended on Zijlema's adoptation (2012) is shown in Tab. 3.1.

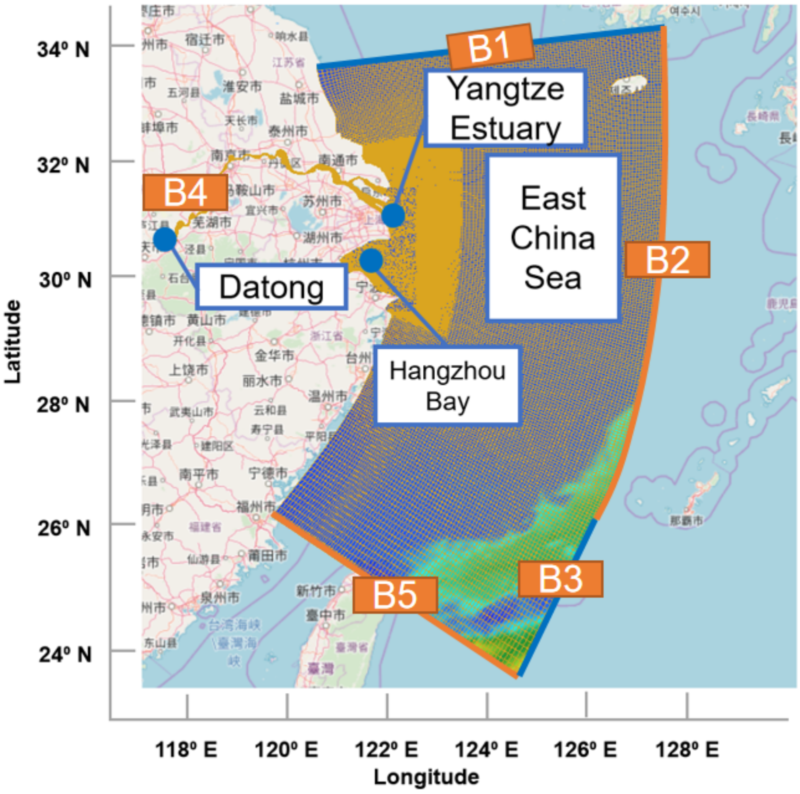

Fig. 3.3.: Overview of the study area. B1, B2, B3, B5 are open boundaries, B4 is the discharge boundary.

Tab. 3.1.: Wind drag coefficient set

Breakpoint	Wind speed(m/s)	Cd
A	5	0.0009839
B	31.5	0.002
C	60	0.0008013

Other parameters

The selected roughness coefficient is manning roughness coefficient, and it is assumed to be 0.026 in the ocean. The calibration of the roughness was based on the work done by Ke (2018).

Since it is the sea water, the water density is set to be 1,025 kg/m^3. And the viscosity is set to be 1 m^2/s.

3.3.2 Calibration and validation for the tide level

Tidal data for validation

Tidal data for validation comes from the following sources:

- Tide table provided by Shanghai Water Authority. The tide table contains the tide level every hour from 0000 BST 15 August to 0000 BST 21 August in 1997, 9000 BST 15 September to 2300 BST 15 October in 2013 and 0000 BST 24 July to 2300 BST 24 August 2015.
- Tide measurement in 2007 from the State Key Laboratory of Estuarine and Coastal Research (East China Normal University). For different measurement points, the measurement date is different. Generally, the measurement took place at the end of July in 2007, and the tide level was recorded every hour and last for 27 hours.

The tide level mentioned above is used in calibration and validation. It is notable that even though some data are provided during a storm, the tidal data are just records for astronomical tides. In other words, tide is the only forcing resulting in the tide table and the measurement result.

Observation points for validation

For different years, data for validation are provided for different observation points. For the tide table provided by Shanghai Water Authority, the observation points are distributed in the estuary and the sea as shown in Fig 3.4. The measured tide level from State Key Laboratory of Estuarine and Coastal Research have another set of measurement points (see Fig 3.5).

Boundary condition for validation

The discharges at Datong from January 1998 to December 2015 are provided by Datong Hydrological Gauging Station. For validation, such discharge is needed for the validation periods in 1997, 2007, 2013 and 2015. For the lack of discharge record in 1997, the discharge at Datong Station is assumed to be 31,000 m^3/s. For other validation cases, the discharges are provided for the validation periods in Appendix B from Fig. B.2 to Fig. B.4. For the open boundaries, M2, S2, N2, K2, K1, O1, P1, Q1 are provided at different locations along the boundaries. For validation

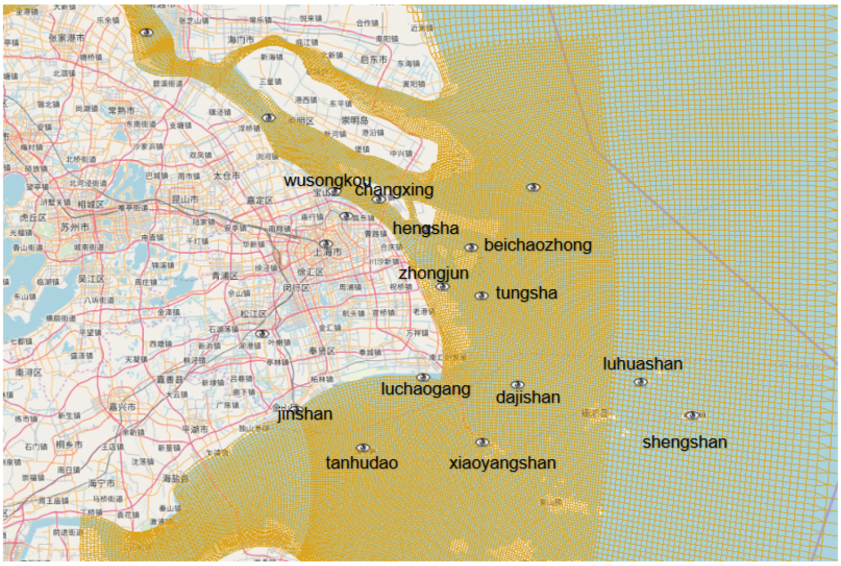

Fig. 3.4.: Observation points for the tide table

cases, the amplitudes and phases for each tide component and each point on the boundaries are provided in Appendix B in Tab. B.2 and Tab. B.3.

Criteria for evaluating results

The criterion for evaluation of the tide level is the error between the modelled water level and the measured water level by root-mean-square error (RMSE) in:

$$RMSE = \sqrt{\frac{\sum(\eta - \eta_m)^2}{N}} \tag{3.1}$$

The correlation coefficient (CC) is also used to see how the simulated water level and tide level from the tide table or the measured water level relate to each other:

$$CC = \frac{\sum(\eta - \bar{\eta})(\eta_m - \bar{\eta}_m)}{\sqrt{\sum(\eta - \bar{\eta})^2}\sqrt{\sum(\eta_m - \bar{\eta}_m)^2}} \tag{3.2}$$

in which η is the modelled water level, [m] and η_m is the tide level from the tide table or the measured water level, [m].These equations are also valid for total water level evaluating when change η_m to be the measured total water level.

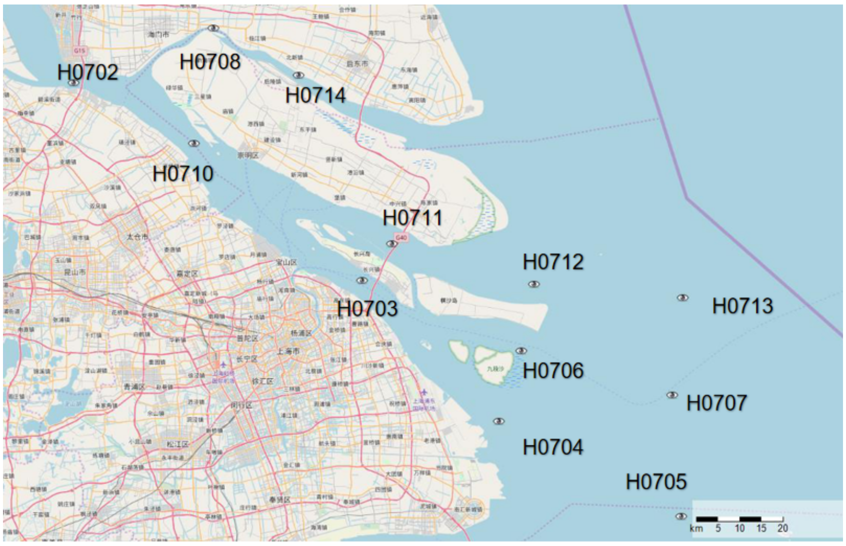

Fig. 3.5.: Measurement points in 2007

Tab. 3.2.: Error of model validation for tides in 1997

No	Station	Without changing		Deducted 2m		Deducted 3m	
		RMSE [m]	CC	RMSE [m]	CC	RMSE [m]	CC
1	Wusongkou	0.19	0.98	0.19	0.98	0.19	0.98
2	Changxing	0.16	0.99	0.16	0.99	0.16	0.99
3	Hengsha	0.2	0.99	0.2	0.99	0.2	0.99
4	Zhongjun	0.21	0.99	0.21	0.99	0.21	0.99
5	Beichaozhong	0.27	0.99	0.27	0.99	0.27	0.99
6	Luchaogang	0.25	0.98	0.25	0.98	0.25	0.98
Average		0.21	0.99	0.21	0.99	0.21	0.99

Calibration processes

The bathymetry may be different resulting from dredging work at the estuary and erosion of the Delta since the Three Gorges Dam was completed. The calibration process of bathymetry is to change the bathymetry of some places in the estuary to see if the modelled tide level fit the tide table better. During this process, keep the bathymetry at the ocean the same as before and then interpolated the changing value together with the former one. By checking the results of tide level, how the tide level affected by the bathymetry can be seen. In order to study the local bathymetry effects on tide level, the bathymetry at the estuary has been deducted 2 m and 3 m. According to the results from Fig. B.5, Fig. B.6 and Fig. B.7 in Appendix B, the RMSE (shown in Tab. 3.2) and the shape of model results don't have any visible differences. The dredging work at the estuary doesn't have any significant effects on the model results. So there is no need to make any differences on the bathymetry.

Tab. 3.3.: Errors of model validation for tides in 2013

No.	Station	RMSE [m]	CC
1	Wusongkou	0.23	0.97
2	Xiaoyangshan	0.16	0.99
3	Zhongjun	0.25	0.99
4	Beichaozhong	0.21	0.99
Average		0.21	0.99

Tab. 3.4.: Errors of model validation for tides in 2015

No.	Station	RMSE [m]	CC
1	Wusongkou	0.25	0.97
2	Hengsha	0.18	0.99
3	Zhongjun	0.26	0.99
4	Beichaozhong	0.22	0.99
5	Luchaogang	0.24	0.99
Average		0.23	0.99

Tide level validation results

The validation for the tide level is also done for 2007, 2013 and 2015 for specific periods. The comparing figures are shown from Fig B.8 to B.10 in Appendix B. There are also summaries for the error of each year from Tab. 3.3 to 3.5.

The average RMSE for the tide level is about 20 cm for 1997, 2013 and 2015, which are compared with the tide table. When it comes to the measurement in 2007, the RMSE is 16 cm. The correlation coefficient is 0.99 for 1997, 2013 and 2015, 0.98 for 2007. That is to say, the model goes well with tide level.

Tab. 3.5.: Error of model validation for tides in 2007

No.	Station	RMSE [m]	CC
1	H0704x	0.17	0.99
2	H0705d	0.15	0.99
3	H0706d	0.13	0.99
4	H0706x	0.09	0.99
5	H0707d	0.18	0.99
6	H0707x	0.15	0.96
7	H0712x	0.20	0.98
8	H0713d	0.17	0.98
9	H0713x	0.19	0.94
Average		0.16	0.98

3.3.3 Validation for the tide plus typhoon

Water level data for validation

The data for validation is the total water level recorded every hour from 15 August to 21 August in 1997, which is also provided by Shanghai Water Authority. To achieve the water level with tide and surge, tide and typhoon should be added into the model. The former is reflected in the input of open boundaries. The latter can be involved in the model with the input of *.spw file. The wind and pressure fields are described by the *.spw file. In this case, the *.spw file is generated with the information of Typhoon Winnie provided by Shanghai Climate Centre. The typhoon information contains typhoon track, central wind speed and pressure from 10 August to 20 August in 1997 with an interval of 6 hours. So only water level from 15 August to 20 August can be validated.

Boundary condition for validation

The discharge at Dangtong is 31,000 m^3/s in 1997. The location and regional tide information for the boundaries at sea side are the same as in Section 3.3.1.

Observation points

The observation points for tide plus typhoon validation are the same in Fig. 3.4.

Criteria for evaluating results

The criterion for evaluation of the result is the error between the modelled water level and the measured water level as in Eq 3.1 and Eq 3.2.

Validation for the tide + surge level

The results of water level validation are shown at Fig B.11 and Fig B.12 in Appendix B, and the RMSE is listed at Tab. 3.6. With a value of 40 cm, the RMSE is a little bit large but the highest water level fits well a few hours before 19 August (see Fig 3.6 as an example). The later two high levels are missed. Ke (2018) has done the validation of tide plus surge level during Typhoon Winnie with the RMSE of 42 cm. The correlation coefficient has an average value of 0.96, which is higher than

Tab. 3.6.: Errors of model validation for water level during Typhoon Winnie

No.	Station	RMSE [m]	CC
1	Beichaozhong	0.44	0.95
2	Changxing	0.42	0.94
3	Dajishan	0.26	0.98
4	Hengsha	0.40	0.95
5	Jinshan	0.70	0.93
6	Luchaogang	0.38	0.97
7	Shengshan	0.31	0.97
8	Tanhudao	0.40	0.96
9	Wusongkou	0.39	0.94
10	Xiaoyangshan	0.23	0.98
11	Zhongjun	0.41	0.95
Average		0.40	0.96

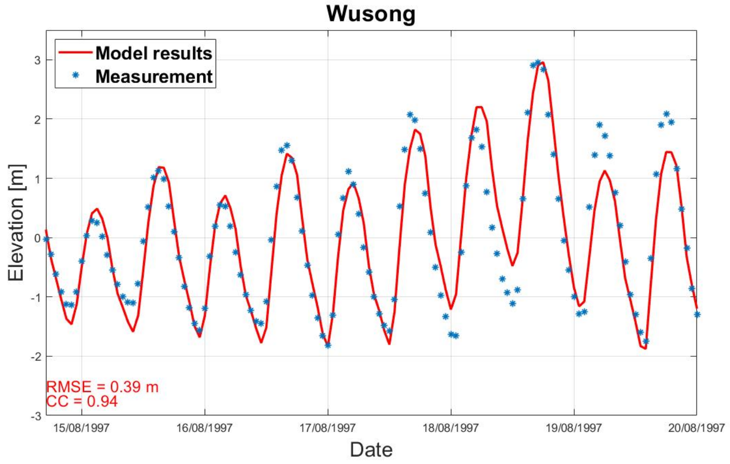

Fig. 3.6.: Model results at Wusongkou

tide level only. But it is still acceptable. Considering the limited data for validation, possible measurement error and typhoon model error, it is reasonable to assume that the hydrodynamic model itself works well.

3.4 Wave model

3.4.1 Model set-up

Boundary condition

All the waves in the study area are generated by wind, there is no boundary condition.

Computational grid

Since unstructured grids are not supported in SWAN or D3D, spherical and constructed grids are used. The grids can be divided into two parts (see in Fig. 3.7). The larger part, which is coarser, covers part of East China Sea, Hangzhou Bay and Yangtze Estuary. And the nested part is more detailed and closer to Shanghai coast. The resolution of the nested part along the coast is about 30 m.

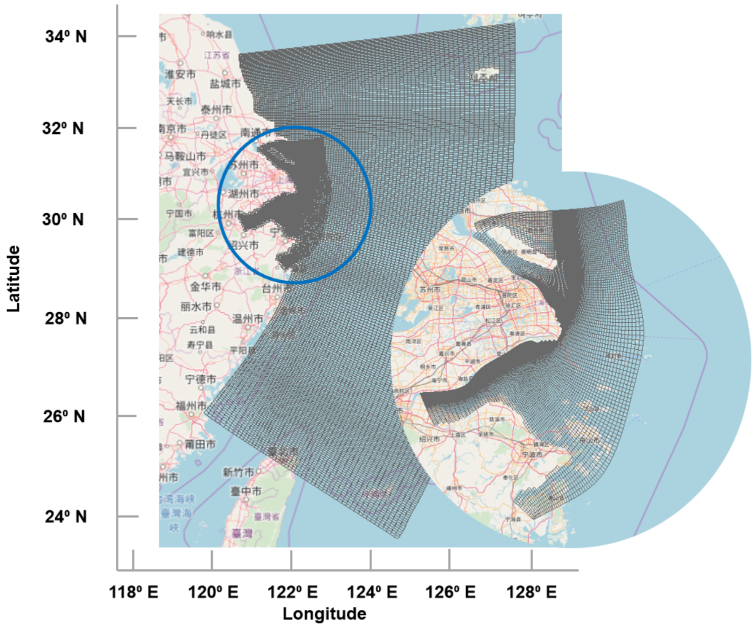

Fig. 3.7.: Nested computational grid for wave model

Bathymetry

The bathymetry used for wave model is the same as used in the hydrodynamic model, which comes from digitized local nautical chart and GEBCO14 Grid. See in Section 3.3.2.

Wind

The input data for wind are the wind velocity in x-direction and y-direction during a typhoon. The specific value is related to the corresponding typhoon.

Other parameters

The gravity is 9.81 m/s^2. The water density is 1,025 kg/m^3. For the other physical parameters and numerical parameters, default values are used. And the computational mode is set to be stationary.

3.4.2 Validation for the significant wave height

Data for validation

The data for wave validation is quite limited. The only set of data in the domain area is from a buoy (122.8°E, 31°N) during Typhoon Fitow in 2013. The buoy recorded the significant wave height from 0100 BST 20 September to 2300 BST 10 October every 60 min. For that the wind file for Fitow only covers from 6 October to 8 October, the significant wave height will be only validated during this period.

Wind and pressure field for typhoon Fitow

The *.spw file containing wind and pressure fields for typhoon Fitow is generated by WES with method 4 (mentioned in Section 2.6.2). The input storm track information is provided by Japan Meteorological Agency (JMA). The track information consists of time, position, typhoon centre pressure (P_c), maximum sustained wind speed (V_{max}) every 6 hours.

Criteria for evaluating results

The criterion for evaluation of the result is the error between the modelled significant wave height and the recorded significant wave height by root-mean-square error (RMSE) in:

$$RMSE = \sqrt{\frac{\sum(Hs - \tilde{Hs})^2}{N}} \tag{3.3}$$

in which Hs is the modelled significant wave height, [m] and $\tilde{Hs}$ is the recorded significant wave height, [m].

Validation results

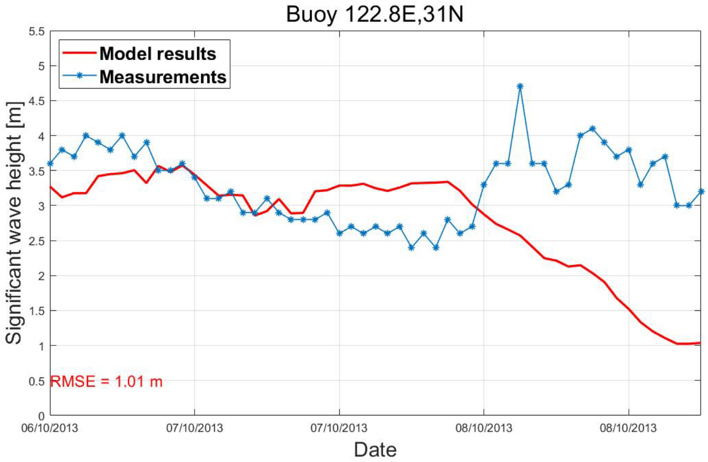

Fig. 3.8.: Significant wave height validation for the wave model

The validation results for significant wave height and peak period during typhoon Fitow are shown in Fig. 3.8 and Fig. 3.9. It is obvious that the model results have similar magnitude. But the RMSE is 1 m, which is a relative high value. It may because of the rapid decrease of the model result for the last few hours. A possible explanation for that is the model result only consider Typhoon Fitow, but in reality, Typhoon Danas also affected the wave at the buoy location.

As shown in Fig. 3.10, the green line represents the track of Typhoon Fitow, and the blue line represents the track of Typhoon Danas. The track of Typhoon Danas also comes from the record by JMA. The red triangle is the location of the bouy. Around 8 October, typhoon Danas was closed to the buoy, and the wave was affected by Danas, so the measured results are different from the model results which only take Fitow into consideration.

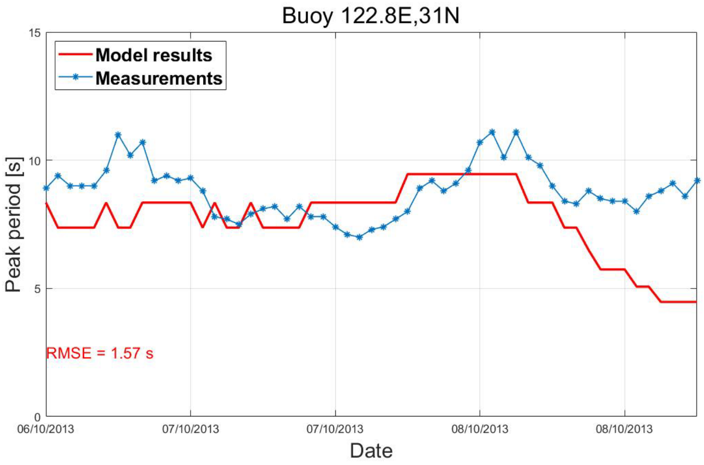

Fig. 3.9.: Peak period validation for the wave model

3.4.3 Wave set-up estimation

For that the wave set-up calculation cannot be applied to spherical model correctly in Delft3D and SWAN, it should be estimated as a part of the water level at the toe of the sea dike.

Based on the references mentioned in Section 2.7.3, the wave set-up at the coastline is assumed to be 5% of the significant wave height modelled at the observation points.

3.5 Overtopping calculation

3.5.1 Parameters in the overtopping equation

According to Eq. 2.31, several parameters are needed for the overtopping calculation.

The significant wave height (H_{m0}) and the peak period (T_p) are directly simulated by the wave model. The water depth (d) is the sum of water depth simulated by hydrodynamic model and the wave set-up. The crown wall freeboard (Hc') can be calculated as:

$$Hc' = EL - (WL + setup) \tag{3.4}$$

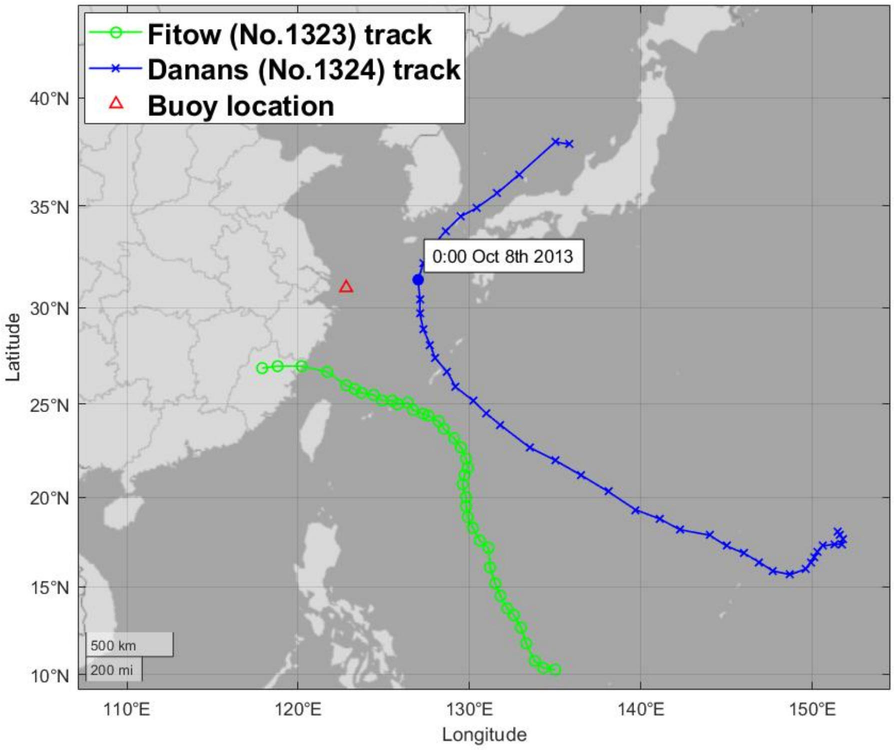

Fig. 3.10.: Typhoon tracks of Fitow and Danas

in which, WL is the water level simulated by hydrodynamic model, [m]; $setup$ is the wave set-up estimated in Section 3.4.3, [m]; EL is the crow wall elevation, [m]. For the validation part, the crown wall elevation for different district is based on the cross-section mentioned in Section 2.4.2.

The reciprocal of the slope angle (m) has the value of 3 for Shanghai sea dikes, so the empirical parameter B is 0.38 according to Tab. 2.3. According to Tab. 2.4, the empirical K_A is set to be 1 with the concrete slab as the revetment. According to the field work in Shanghai, there is no distance between the crest edge and the crown wall, so b_1 is set to be 0.

3.5.2 Validation to overtopping during Typhoon Winnie

As mentioned in Section 2.2.2, it was observed that there was sea dike breaching in Jinshan and sea dike overtopping in Fengxian during Typhoon Winnie in 1997. Overtopping calculation should be validated by historical records. Firstly, hydrodynamic model and wave model are applied to Typhoon Winnie. During this process, the basic set-up of these two hydrodynamic models is the same in Section 3.3.1 and Section 3.4.1. The input wind and pressure fields are generated by WES based on typhoon best track provided by Shanghai Climate Centre. Then, with the resulting water level and wave parameters, overtopping rate along the coast can be calculated according to the method in Section 3.5.

Observation points for overtopping validation

The observation points for overtopping validation are distributed along the coast as the blue points shown in Fig. 3.11. The green points in Fig. 3.11 show the corresponded calculation points in the hydrodynamic model and wave model, which give the water level and wave condition at the toe.

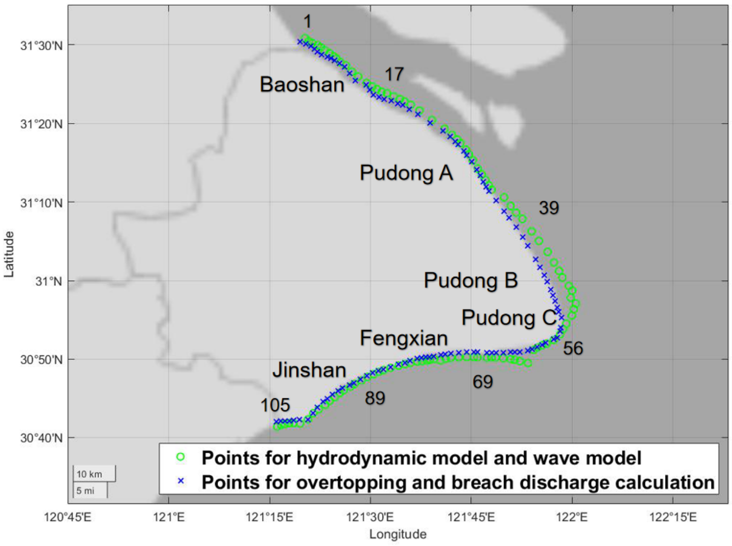

Fig. 3.11.: Observation points for overtopping calculation and corresponded calculation points in hydrodynamic models

Overtopping validation result

The result of overtopping during Typhoon Winnie is shown in Fig. 3.12. The maximum overtopping on the y-axis means the highest overtopping during the specific typhoon for each observation point. The No. of the observation point on the x-axis represent 105 observation points (shown in Fig. 3.11, blue points) from the No.1 place in Baoshan to the No.105 in Jinshan district. According to Fig. 3.12, the highest overtopping rate is 0.32 $m^3/m/s$ around Jinshan Zui. The average overtopping rate in Fengxian is about 0.09 m^3/m/s. Such high overtopping rate is roughly consistent with historical observation that there was sea dike breaching in Jinshan and sea dike overtopping in Fengxian during Typhoon Winnie in 1997.

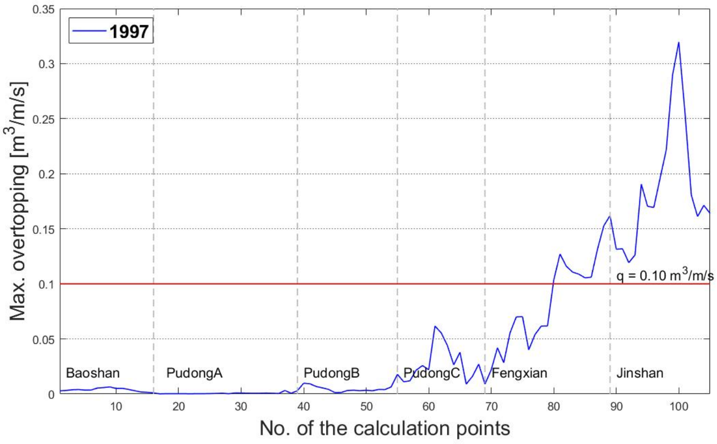

Fig. 3.12.: Overtopping results during Typhoon Winnie in 1997

3.6 Breach discharge calculation

3.6.1 Calibration of the threshold

It is described in Section 2.9.4 that Zhang et al. (2017) concluded from their experimental data that for the dry masonry block covered on the inner slope (1:3), the failure overtopping rate ranges from 0.105 to 0.117 m^3/m/s. But it is just a general result of physical model experiment, the threshold of breaching specific for sea dike in Shanghai should be estimated. As mentioned in Section 2.2.2, it was recorded that there was sea dike breaching in Jinshan and sea dike overtopping in Fengxian during Typhoon Winnie in 1997. According to the result in Section. 3.5.2, during Typhoon Winnie, the highest overtopping rate is 0.32 m^3/m/s around Jinshan Zui. The average overtopping rate in Fengxian during Typhoon Winnie is about 0.09 m^3/m/s. In order to achieve worse cases, it is assumed that the sea dike starts to breach with the overtopping rate of 0.1 m^3/m/s.

3.6.2 Parameters in the breaching equations

Once the sand dike breaches, the breaching process will be quite fast. Then it is reasonable to assume that the final breach dimensions can be achieved soon after the start of the breaching process. In this research, only the last two stages are considered. Eq. 2.36 and Eq. 2.37 give the discharges through the breaches in these last two stages. Only the points which have the overtopping rate higher than the threshold of breaching can be applied to these equations.

In Section 2.9.2, the three breach types distinguished by Visser (1998) have been described. According to the cross-sections in Shanghai (shown in Section 2.4.2) and the field work in Shanghai (in Appendix A), there is always some protections over the forehead. It is assumed that the breach in Shanghai sea embankment is a type A breach. So the discharge coefficient m is 1 in Eq. 2.36 and Eq. 2.37. In type A breaching, the berm structure is actually the breach bottom, so the height of the breach bottom (Z_{br}) is the height of the berm.

The outer water level (H_w) is the sum of water level simulated by hydrodynamic model and the estimated wave set-up. The water level in the polder behind the dike (H_p) is assumed to be the bed level behind the dike. That is because the dike is assumed to breach in a short time and there is nearly no water behind the dike when the dike starts to breach. Since the breach width is still unclear, a breach width of 300 m, 500 m and 1,000 m will be applied. It is still necessary to see how the breach width affects the overland simulation.

3.7 Overland simulation

The overland simulation is also based on D-Flow module in Delft3D-FM. For the overland simulation, the drainage capacity of Shanghai, because when the tide level is high, it is hard to drain waterlogged fields (Wang et al., 2012). Since there was no breach area recorded, no validation is made for the overland simulation. The hypothetical events are applied to the overland simulation directly after the model is set up.

3.7.1 Model set-up

Boundary condition

The locations of the boundaries are set along the coastline of Shanghai. The discharge at boundaries are overtopping discharge and breach discharge calculated. It is notable that the overtopping rate has the unit of $m^3/m/s$. As the discharge boundary should have the unit of m^3/s. So the overtopping applied here is the product of the overtopping rate and the average distance from a calculation point to two adjacent points. There is no information about the discharge through the sluices. It is assumed that all the sluices along Shanghai coast are closed during the model time, the discharge for each sluice is set to be 0 m^3/s. The locations of the sluices are the blue points shown in Fig. 3.13. As shown in Fig. 3.13, only the part of Wusong River in Shanghai is considered in the model, and the green point shows the boundary point of Wusong River. For the lack of discharge in Wusong River, it is also assumed that there is no water exchange at that point, so the discharge at the boundary is also assumed to be 0 m^3/s.

Grid

The grids for overland simulation are unstructured. Most of the grids are in the shape of triangle, which are distributed on land. The overall area covered in the grid is 5,427 km^2. Only a few grids on river are in the shape of rectangle. Fig. 3.13 shows the grid-covered area. And Fig. 3.14 shows the details of land grids near Wusongkou.

Bathymetry

The elevation of underlying surface is the same as mentioned in Section 2.5.2. The bathymetry is set to be the initial water depth in the overland simulation(see Fig. 3.15).

Roughness

Fig. 3.16 shows the roughness overland. The rivers and open roads are smoother while the buildings are rougher. The roughness is represented by floodplain Manning roughness coefficients in the model for individual pixels. The value for urban area,

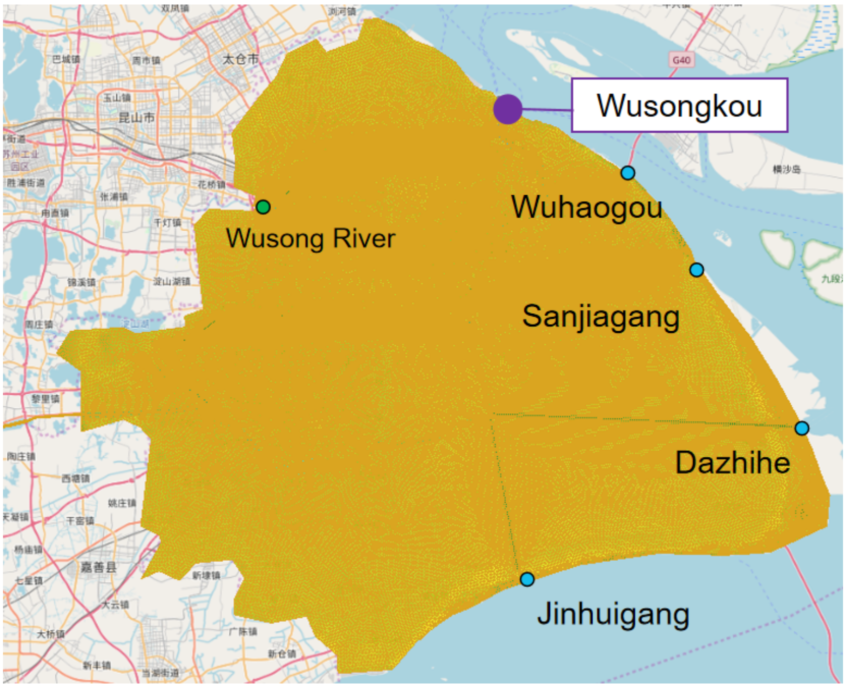

Fig. 3.13.: Overview of the computational grid in overland simulation. Blue points are the location of the sluices. The green point is the boundary point of Wusong River in the model

farmland, grasses, water bodies and bareland are 0.01, 0.05, 0.06, 0.03 and 0.035 respectively (Yu et al.,2016).

3.8 Summary

In this chapter, the approach and methodology of this research are explained. Wind model, hydrodynamic model and wave model are set up and then validated. For the lack of historical data, the validation of overtopping calculation is based on the comparison with historical record. There is no validation for the breach discharge calculation and overland simulation since there is no historical record.

With the approach and methodology prepared, they can be applied to analyze the effects of climate change on coastal flooding in the following chapter.

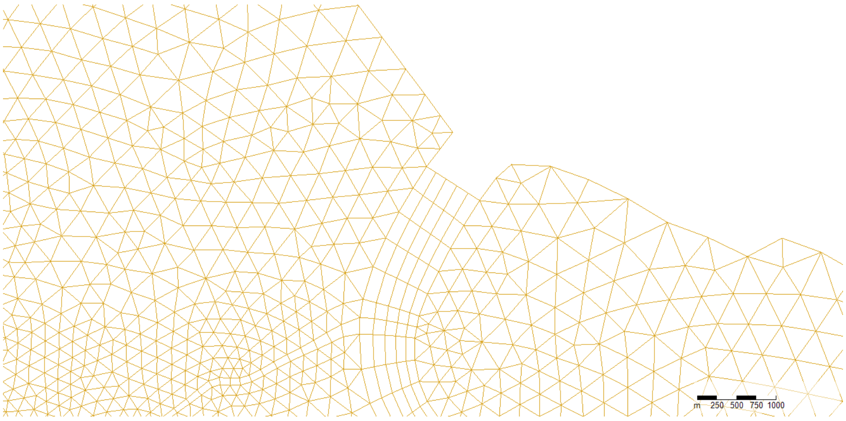

Fig. 3.14.: Details of land grids near Wusongkou

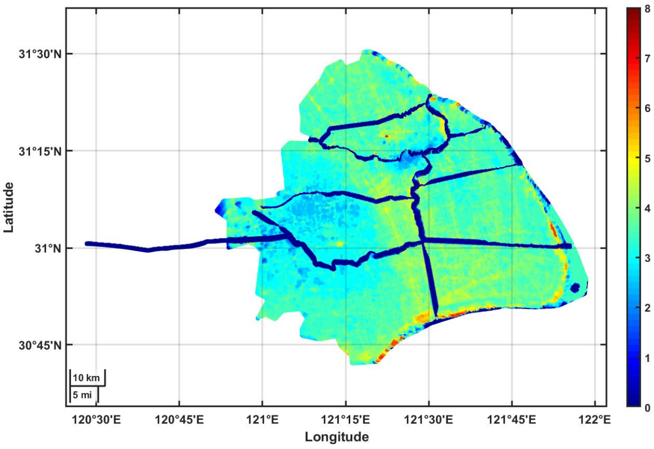

Fig. 3.15.: Land level over Shanghai area (1985 national height datum)

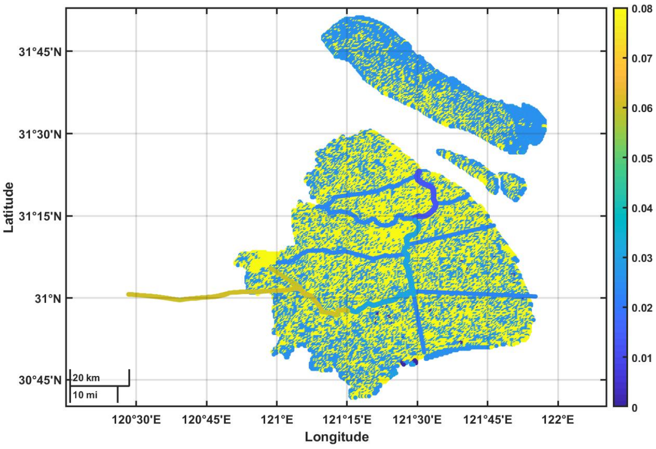

Fig. 3.16.: Overland roughness over Shanghai area

4

Effects of climate change on coastal flooding in Shanghai: model set-up

4.1 Introduction

In this chapter, all the methods and models mentioned in Chapter 3 are applied to climate change cases. The application environment is explained in Section 4.2, 4.3 and 4.4.

After the hydrodynamic model and wave model proved to be valid, they are applied to hypothetical typhoon events provided by the Met Office Hadley Center under historical and future climate conditions. The wave condition and water level along the coast are achieved for these hypothetical events, considering multiple effects of storm, wave and spring tide.

Overtopping is seen as the main cause of dike breaching. Several points are set for overtopping and breach discharge calculations along the coastline. The places where experience high overtopping volumes are more likely to be the breaching places. A threshold of breaching is also estimated. The overtopping and breaching calculations are also applied to these hypothetical events.

An overland simulation is established by Delft3D-FM for Shanghai city, considering sea level rise and land subsidence. The hypothetical events are also applied to the overland simulation.

4.2 Hypothetical typhoon events

UK Met Office Hadley Center made extreme value analysis of the most intense tropical storms with different climate conditions over the Shanghai area of interest (26°N-34°N, 117°E-127°E). They analysed not only the events hit the coast but also tropical storms passing in this region, which still have the potential to affect

Shanghai. They analysed storm events from 1981 to 2000 under historical climate condition and events from 2080 to 2099 with the representative concentration pathways (RCP) of 8.5. Five typhoon events simulated under historical climate condition around the year 2000 are shown in Tab. 4.1. Moreover, five typhoon events simulated under future climate condition around the year 2100 are shown in Tab. 4.2. In general, events in the future climate show greater intensity than the past climate. The typhoon tracks over the Shanghai area of interest for events under historical climate condition are shown in Fig.4.1, and typhoon tracks over the Shanghai area of interest for events under future climate condition are shown in Fig.4.2.

In the tables, lon and lat are standard longitude and latitude of the centre of the storm, [deg]; MSLP is the minimum mean sea level pressure along the typhoon track in the Shanghai area of responsibility, [pa]; Wspeed is the 10 m maximum wind speed along the typhoon track in the Shanghai area of responsibility, [m/s]; τ is the return period considering the maximum wind speed along the trajectory included in the Shanghai area of responsibility, [yr]. The return period is based on all the typhoon events one over the Shanghai area of responsibility, rather than only hitting Shanghai. The wind and pressure fields for these ten scenarios are all provided.

For easy explanation later, these hypothetical events are named after the wspeed return period. For example, the case R7.9 represents the case with the return period of 7.9 yr.

Tab. 4.1.: Hypothetical typhoon events in historical climate condition

Scenario	Lon	Lat	MSLP	Wspeed	τ
R7.9	123.17	27.08	93470	50.2	7.9
R3.4	124.27	25.62	93082	47.7	3.4
R2.9	125.09	31.93	94270	47.0	2.9
R1.3	121.24	25.34	94096	42.3	1.3
R1.0	124.70	29.81	96739	39.7	1.0

Tab. 4.2.: Hypothetical typhoon events in future climate condition

Scenario	Lon	Lat	MSLP	Wspeed	τ
R18.3	125.52	25.49	89738	58.45	18.3
R8.0	123.74	29.58	91583	56.67	8.0
R6.9	126.00	30.85	90093	56.18	6.9
R4.5	122.24	30.09	93047	54.64	4.5
R3.6	126.73	27.63	91908	53.62	3.6

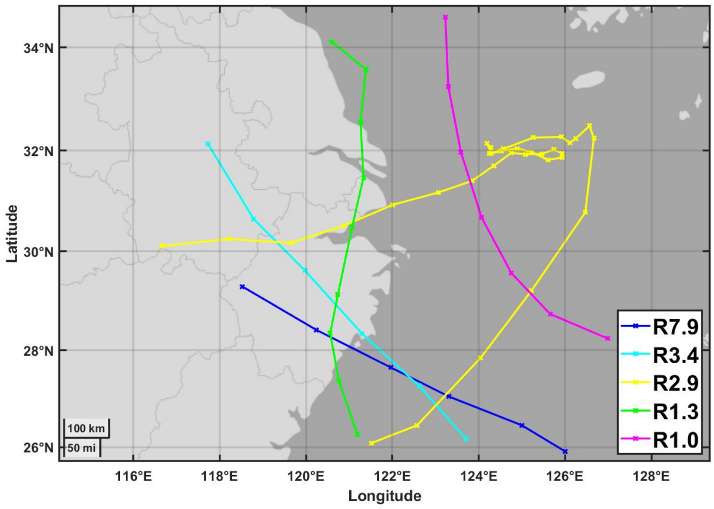

Fig. 4.1.: Typhoon tracks over the Shanghai area of interest in historical climate condition for every 6 hr

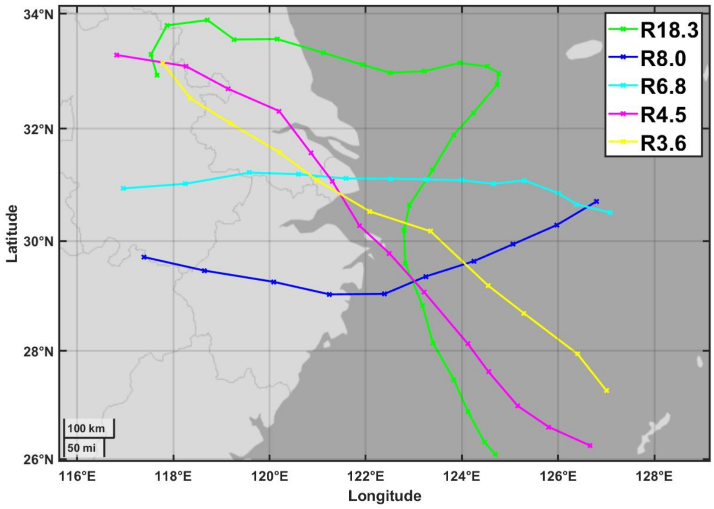

Fig. 4.2.: Typhoon tracks over the Shanghai area of interest in future climate condition for every 6 hr

4.3 Assumptions for the sea embankments

In this case, it is assumed that all the dikes have a typical shape as following: with good quality of grass and dry masonry block in the inner slope dike side at the first layer of revetment. Fig. 4.3 shows a typical inner slope of sea dikes in Shanghai. The geo-bags served in the second underneath layer being fulfilled with silt and covered by plastic bags. This assumption is based on field work in Shanghai (in Appendix A) and the typical cross-section in Section 2.4.2.

Two sets of sea embankment dimensions are used in this research. One is for the reference situation, the other is for the actual situation.

Fig. 4.3.: Typical inner slope of sea dikes in Shanghai, taken during the field work in Shanghai

4.3.1 Reference situation

The reference situation is mainly based on the typical cross-sections provided by Chen and Qi (2010) as mentioned in Section 2.4.2.

Several assumptions are made for the reference situation:

1 The sea embankments along Shanghai coast can be divided into six parts.

2. The sea embankments in each part have the same cross-section as the typical cross-section in this part apart from the Fengxian District part. Because the cross-section in Fengxian does not have a crown wall as shown in Fig. 2.6, which cannot fully reflect the reality as a reference.

3. In Fengxian District part, the crest elevation is 8.7 m and the wall elevation is 9.9 m (Chen and Wang, 2015).

4.3.2 Actual situation

The other is mainly the measurement result from the field work in Shanghai in September 2019. Since only the crest elevation and the crown wall elevation have been measured for a few points along the coast, several assumptions are made for the actual situation:

1. The crest elevation and the crown wall elevation at the places between the measurement points are interpolated by distance.

2. The general cross-sections are not changed. It means that the elevation between crest and berm is the same as that in the reference situation.

4.3.3 Regional sea level rise and land subsidence for different hypothetical cases

Section 2.5.4 introduced the regional sea level rise and land subsidence condition in Shanghai. The geographic data in Shanghai are provided around the year 2010. So for the hypothetical cases under historical climate condition, the related land elevation may be higher than the elevation in 2010. For the hypothetical cases under future conditions, the land elevation may be lower.

Land subsidence and sea level rise are considered in overland simulation and it can be achieved by changing the inland elevation. The changes for different cases are shown in Tab. 4.3.

Tab. 4.3.: Effects of sea level rise and land subsidence for different hypothetical cases

Cases	Sea level rise	Land subsidence (m)	rSLR(m)
Historical hypothetical events (10 years ago)	-0.02	-0.015	-0.035
Future hypothetical events (90 years later)	0.3925	0.1335	0.526

4.4 Explanation for the application cases

Considering sea level rise and land subsidence, three different cases are applied to overtopping calculation, breaching calculation and overland simulation. These three cases, relating sea embankment and inland elevations, are called the reference case, the past case and the future case. Tab. 4.4 shows how these three cases are applied to different climate condition.

Tab. 4.4.: Explanation for the application cases

	Sea embankment	Inland elevation	Application
Reference case	Reference case	Inland elevation around 2010 (see in Section 2.5.2) -rSLR 10 years ago	Historical climate condition
Past case	Actual situation -rSLR 10 years ago (see in Tab. 4.3)	Inland elevation around 2010 (see in Section 2.5.2) -rSLR 10 years ago	
Future case	Actual situation +rSLR 90 years later (see in Tab. 4.3)	Inland elevation around 2010 (see in Section 2.5.2) +rSLR 90 years later	Future climate condition

4.5 Calculation points

As shown in Fig. 4.4, there are two sets of points. The green circles represent the observation points for hydrodynamic model and wave model, while the blue crosses represent the calculation points for overtopping and breach discharge calculation. For each set of points, there are altogether 105 points along the coastline. The distance between two adjacent points is about 2 km. It is assumed that for each hydrodynamic calculation point, there is a related fixed calculation point along the coastline on land, representing the sea dike over there. A hydrodynamic calculation point is closed to the corresponded calculation point for overtopping and breaching. However, for the reason that there is a reclaimland under construction on the southeast of Shanghai, the observation points over there are set to be more seaward. In this way, the results are not underestimated.

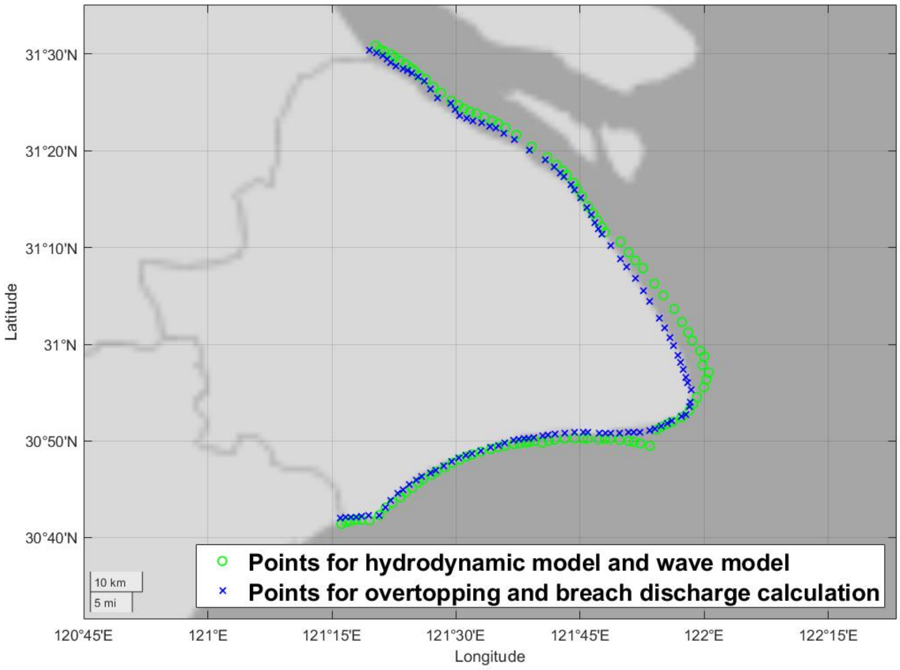

Fig. 4.4.: Calculation points for overtopping and breaching

4.6 Hydrodynamic model

When the model is set up and validated, it can then be applied to cases in different climate conditions. The water level at different observation points along the coast are concerned in the hydrodynamic model and are useful for further calculation. The basic set-up is the same in Section 3.3.1. The following input is specific for these events.

The discharges at Datong Station for the hypothetical events were not simulated or predicted. To achieve the worst case results, the discharge applies to Datong Station is set to be same as the daily average discharge in 1998 from 26 July to 9 August (shown in Fig. 4.5), which was the discharge during an extraordinary flood in 20th century in Yangtze River.

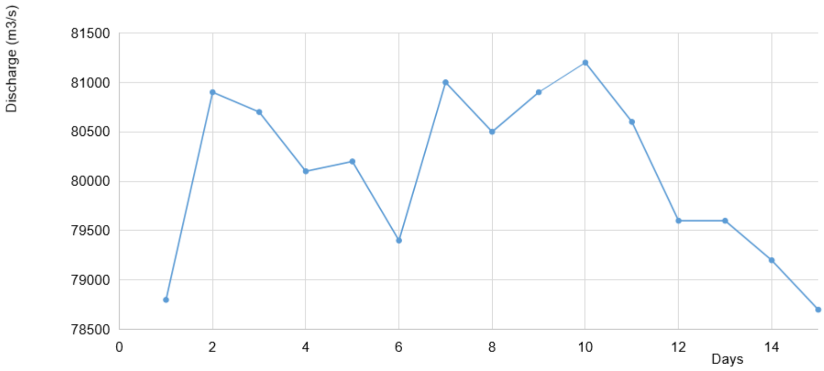

Fig. 4.5.: Daily average discharge at Datong Station from 26 July to 9 August in 1998

Tide level during spring tide is also set for the four boundaries in the sea. Since the tide level validation has done, apply the model with tide constitutes to check for the spring tide in 1997. The spring tide level from 21 July to 6 August contains the highest tide level of 1.8 m at these four boundaries. Then the tide level of four boundaries during this period are assumed to be the boundaries of the spring tide. In this way, storm surge and spring tide can meet each other to get a worse case.

As mentioned in Section 4.2, the wind and pressure fields for the hypothetical typhoon events are provided for every time step. The observation points for the hydrodynamic model are mentioned in Section 4.5.

4.7 Wave model

When the model is proved to go well, it can then be applied to the hypothetical typhoon events mentioned in Section 4.2 to see the results. The significant wave height and wave period at different observation points along the coast are concerned in the wave model and are useful for further calculation. The basic set-up is the same in Section 3.4.1. The applied wind and pressure fields are the same as in the hydrodynamic model in Section 4.6. The observation points for the wave model are the same as used in the hydrodynamic model. See in Section 4.5.

4.8 Overtopping calculation

As explained in Section 3.5, most of the parameters can be achieved directly by the hydrodynamic model and wave model while the rest can be achieved by easy calculation. In Section 4.4, three cases called reference case, past case and future case are mentioned considering relative sea level rise. In addition to the result of hydrodynamic model and wave model, the difference among three cases lies in the seawall elevation when applying to the overtopping calculation.

The result of overtopping calculation for different cases is the overtopping rate at the calculation points (mentioned in Section 4.5) along the coast.

4.9 Breach discharge calculation

The parameters for breach discharge calculation are explained in Section 3.6. The calculation points for breaching are explained in Section 4.5. It is assumed in Section 3.6.1 that the sea dike starts to breach with the overtopping rate of 0.1 $m^3/m/s$. That is to say, only the calculation points with maximum overtopping rate higher than 0.1 $m^3/m/s$ can be applied to breaching calculation. The parameters for breach discharge calculation are explained in Section 3.6. In addition to the result of hydrodynamic model and wave model, the breach bottom (Z_{br}) and the water level in the polder behind the dike (H_p) are affected when applying different cases. That is because the breach bottom (Z_{br}) is a part of sea embankment and the water level in the polder behind the dike (H_p) is related to the inland elevation. See Section 4.4 for the detailed differences among different cases.

The result of overtopping calculation for different cases is the breach discharge at the calculation points (mentioned in Section 4.5) along the coast.

4.10 Overland simulation

The basic set-up of overland simulation is explained in Section 3.7.1. For different cases, the boundary discharge and the overland elevation are different. The boundary discharge relies on the result of overtopping and breach discharge calculation for different cases. The overland elevation is applied considering relative sea level rise as explained in Section 4.4. For a specific case, if the sea embankment is not likely to breach according to the breaching threshold (mentioned in Section 3.6.1), only the overtopping rate will be considered along the coast. If the sea embankment is likely to breach somewhere, both the overtopping and breach discharge will be considered.

The result of overland simulation for different cases is the inundation map, including inundation area and inundation depth over the land.

4.11 Summary

In this chapter, the whole research process is applied to climate change cases. The application environment is also explained. The result of each step of the process will be shown in the next chapter.

5

Effects of climate change on coastal flooding in Shanghai: results

5.1 Introduction

In this chapter, the results of climate change cases set up in the last chapter are shown.

The result of hydrodynamic model is the water level along the coast during specific typhoon events. The water level is more or less harmonic along the time because of the tide. The maximum water level of each observation point is used to represent the situation along the coast.

The result of wave model is the wave parameters along the coast. Significant wave height and peak period are two concerned parameters for the overtopping calculation in the next step. In this part, the maximum significant wave height of each observation point is used to represent the situation along the coast.

The result of overtopping calculation is the overtopping rate along the coast. For a specific calculation point, the overtopping rate changes with time. In this part, the maximum overtopping rate of each calculation point is used to represent the situation along the coast.

For breach discharge calculation, not every calculation points are breached. So result of breach discharge calculation is the breach discharge at the points where are likely to breach. Since the breach width is still unclear, for different cases, the maximum breach discharge per meter of each breaching point is used to show the breaching situation. Results of different breach widths (300 m, 500 m and 1,000 m) applied to the case R4.5 is also shown.

For the overland simulation, the inundation map of each case is shown with the maximum water depth during the corresponded typhoon event. The inundation process of case R4.5 is shown as an example. The inundation maps of case R4.5

with different breach widths (300 m, 500 m and 1,000 m) are also shown to make a comparison.

5.2 Storm surge model

5.2.1 Hypothetical events under past climate condition

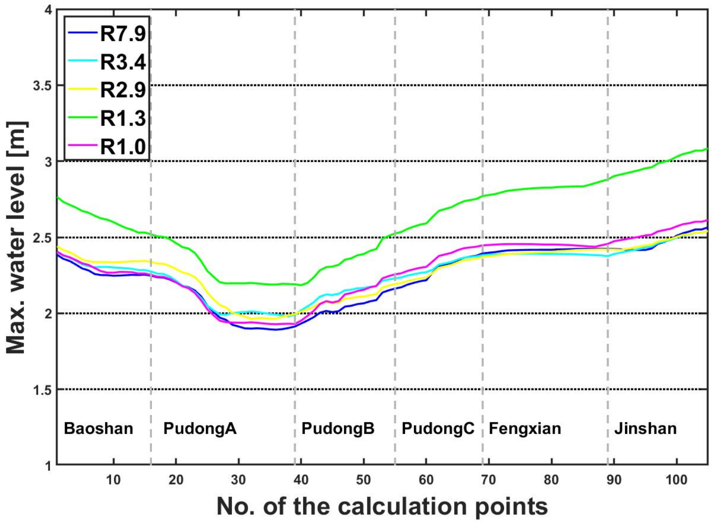

Fig. 5.1.: Max. water level during hypothetical events under past climate condition

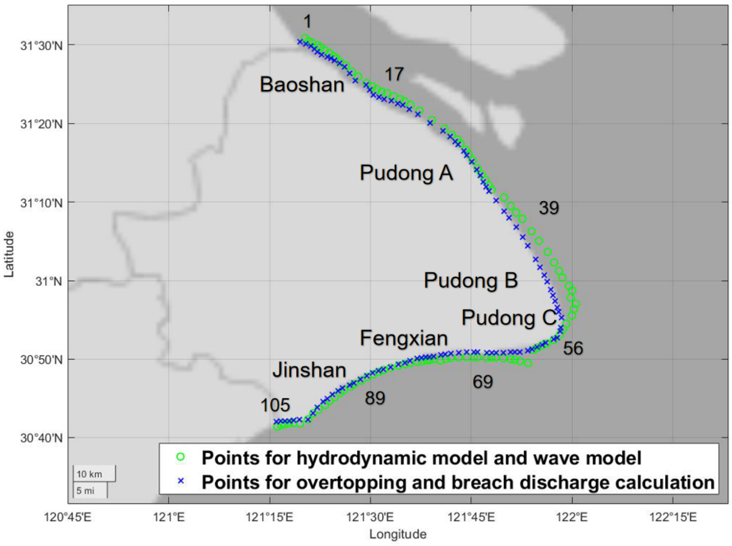

Fig. 5.2.: Distribution of the calcualtion points

Fig. 5.1 shows the maximum water level during hypothetical events under past climate condition. The No. of the calculation point on the x-axis represent 105 calculation points from Baoshan District to Jinshan District (shown in Fig. 5.2). The Max. water level on the y-axis represent the highest water level for each calculation point during the related event. The water level here contains the tide and surge.

For all these cases, the water level seems to be lower in Pudong New District and higher in Baoshan District and Jinshan District. Among these events, case R1.3 shows visible higher water level than other cases, and the highest water level is higher than 3 m. Case R7.9, R3.4, R2.9 and R1.0 show similar highest water level along the coast.

In Appendix B, Fig. B.13 and Fig. B.14 show the resulting time-varying water level at Wusongkou for different cases as examples.

5.2.2 Hypothetical events under future climate condition

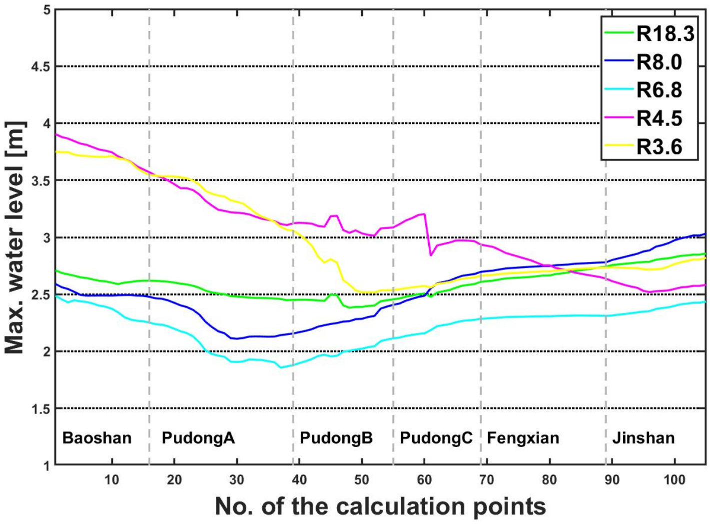

Fig. 5.3.: Max. water level during hypothetical events under future climate condition

Fig. 5.3 shows the maximum water level during hypothetical events under future climate condition. Case R4.5 and R3.6 show general higher water level than other cases, especially in Baoshan District and Pudong New District. The highest water level is almost 4 m in case R4.5 in Baoshan, which is about 1 m higher than the maximum water level in the past cases.

In Appendix B, Fig. B.15 and Fig. B.16 show the resulting time-varying water level at Wusongkou for different cases as examples.

5.3 Wave model

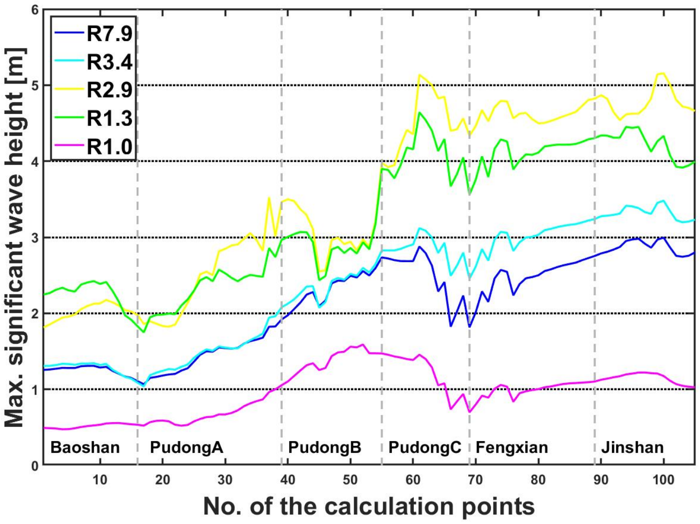

Fig. 5.4.: Max. significant wave height during hypothetical events under past climate condition

The local significant wave height and the peak period during specific typhoon events are concerned in this part. Fig. 5.4 and Fig. 5.5 show the maximum significant wave height along the coast during hypothetical typhoon events under past climate condition and future climate condition, respectively.

In general, the significant wave height is higher along Hangzhou Bay, e.g. in Pudong New District C, Fengxian District and Jinshan District. For past climate cases, case R2.9 and R1.3 have higher significant wave height than the other cases. For some parts in Pudong New District C and Jinshan District, the significant wave height of case R2.9 is even higher than 5 m. Interestingly, the return periods of these two cases do not rank high among the past climate cases. Case R7.9 and R3.4 have longer return period, but the significant wave height of these two cases are lower than case R2.9 and R1.3 along the coast. The same thing happens to future climate cases. Even though case R18.3 and R8.0 have longer return period than other future cases, the significant wave height is lower than case R6.8, R4.5 and R3.6.

From Fig. B.17 to B.20 in Appendix B, the time-varying significant wave height at Wusongkou for different events are shown.

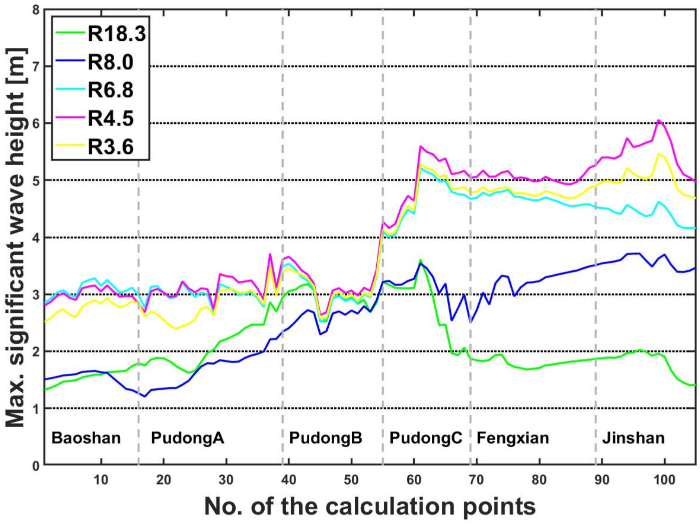

Fig. 5.5.: Max. significant wave height during hypothetical events under future climate condition

5.4 Overtopping calculation results

Fig. 5.6 shows the maximum overtopping rate during hypothetical historical events with the sea embankment of the reference case. The maximum overtopping on the y-axis means the highest overtopping during the specific typhoon for each calculation point. The threshold of breaching is also shown in the figure, represented by a red line with the overtopping rate of 0.1 $m^3/m/s$

During typhoon in the case R1.3, the overtopping is much higher than other events, especially in Pudong New C, Fengxian and Jinshan District. It is reasonable since case R1.3 shows visible higher water level than the other cases as shown in Fig. 5.1.

Fig. 5.7 shows the maximum overtopping rate during hypothetical historical events with the sea embankment of the past case. Overtopping in case R1.3 is also much higher than the other events at the same calculation point. Several points in Pudong New C, Fengxian and Jinshan District have overtopping higher than the maximum overtopping in the reference case.

Fig. 5.8 shows the maximum overtopping rate during future hypothetical events with the sea embankment of future case. The overtopping rates in most of the future climate cases are higher than the past climate cases. The overtopping is more significant in case R3.6 and R4.5. In case R3.6, all the districts have places with overtopping rate higher than the breaching threshold. Even though case R18.3

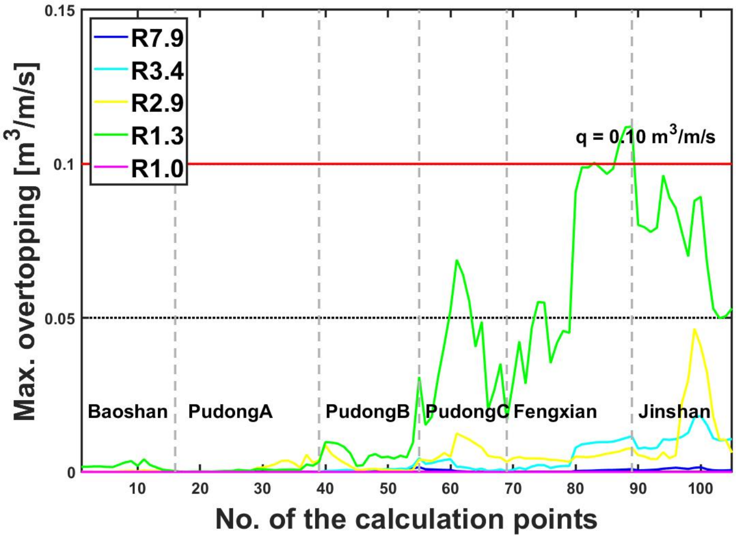

Fig. 5.6.: Max overtopping along Shanghai coast under hypothetical historical events (reference case)

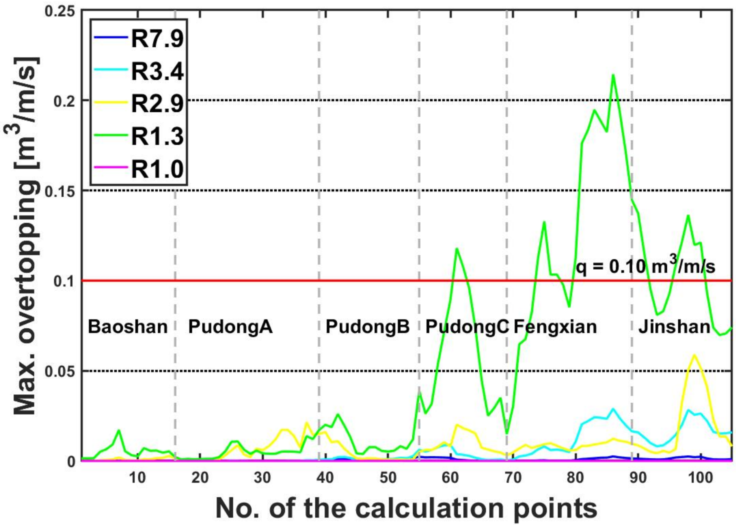

Fig. 5.7.: Max overtopping along Shanghai coast under hypothetical historical events (past case)

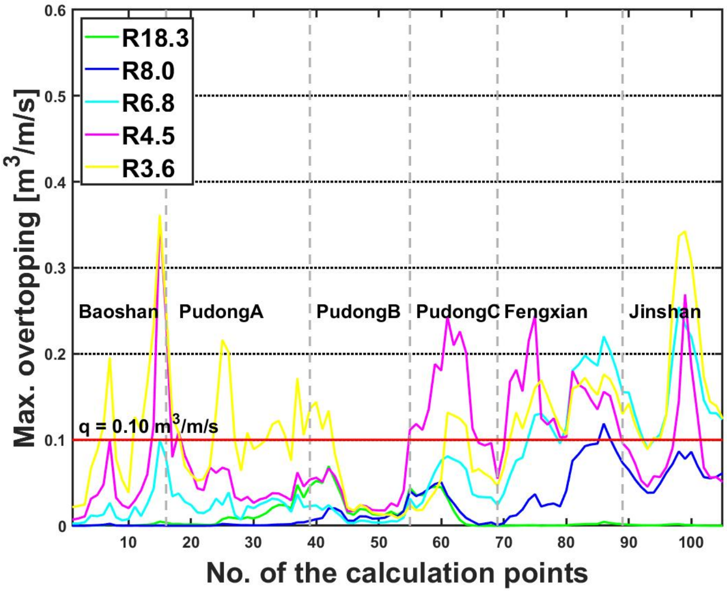

Fig. 5.8.: Max overtopping along Shanghai coast under future hypothetical events

Tab. 5.1.: The number of breaching points for different cases

Scenarios		Breaching points
R1.3	Reference case	4
	Past case	23
R8.0	Future case	2
R6.8		29
R4.5		37
R3.6		62

has the longest return period among the future climate cases, the overtopping rate is lower than the other cases. It is not surprising because of the water level and significant wave height of case R18.3 is not outstanding compared to other cases.

5.5 Breach discharge calculation results

With a total of 105 calculation points along the coast, Tab. 5.1 shows the number of breaching points for different cases. This table only shows the cases are likely to breach. For overtopping only cases, the number of breaching point is 0.

For past climate cases, only the R1.3 case is likely to breach. Fig. 5.10 shows the maximum breaching location and discharge in case R1.3 under the reference case. The maximum breaching rate on the y-axis means the highest breach discharge per meter during the specific typhoon for each calculation point. The No. of the calculation point on the x-axis represent 105 calculation points from Baoshan District to Jinshan District. Fig. 5.10 shows four points in Fengxian District. It means that if the typhoon in R1.3 with the sea embankment of reference case, these points along the sea embankment are likely to breach.

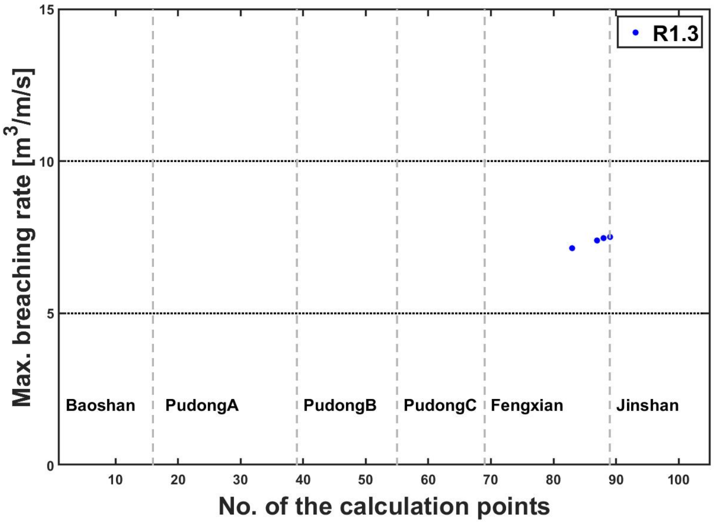

Fig. 5.9.: Breaching location and maximum breaching rate in case R1.3 (reference case)

Fig. 5.10 shows the maximum breaching location and discharge in R1.3 under the past case. And Fig. 5.10 shows breaching points in Pudong New District C, Fengxian and Jinshan District.

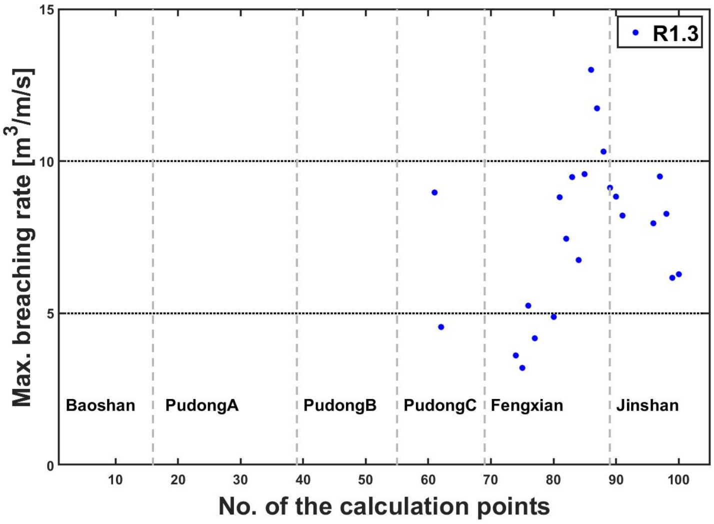

Fig. 5.10.: Breaching location and maximum breaching rate in case R1.3 (past case)

When it comes to future cases, more points are likely to breach according to Fig. 5.11. There is no breaching point for case R18.3. For breaching cases, quite a few breaching points are distributed along Hangzhou Bay, e.g. in Pudong New District C, Fengxian and Jinshan District.

There are only two breaching points for case R8.0 in Fengxian District. The breaching points in case R6.8 are distributed in Fengxian and Jinshan District. In case R4.5, several points at the boundary of Baoshan and Pudong New District A will breach with a large breach discharge. Most of the breaching points in case R4.5 are distributed along Hangzhou Bay, e.g. in Pudong New District C, Fengxian and Jinshan District. For case R3.6, the breaching points are distributed in every district.

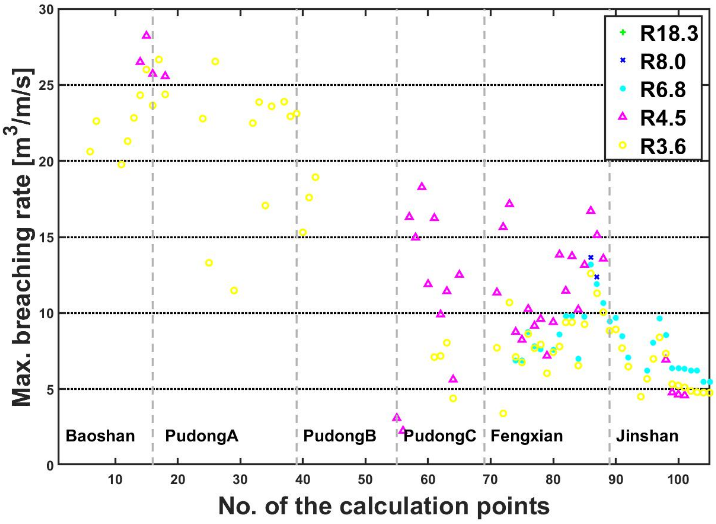

Fig. 5.11.: Breaching location and maximum rate discharge in future events

Fig. 5.12 shows the impacts of the breach width on the breach discharge. For that the breaching standard does not change, the breach locations keep the same for different breach width. The breach discharge also has a linear relation with the breach width. The highest breach discharge with a breach width of 1,000m is in Baoshan District. The breach discharge is nearly 30,000 m^3/s.

5.6 Overland simulation

In this part, the overland simulation is applied to different hypothetical scenarios. The cases for overland simulation are shown in Tab. 5.2.

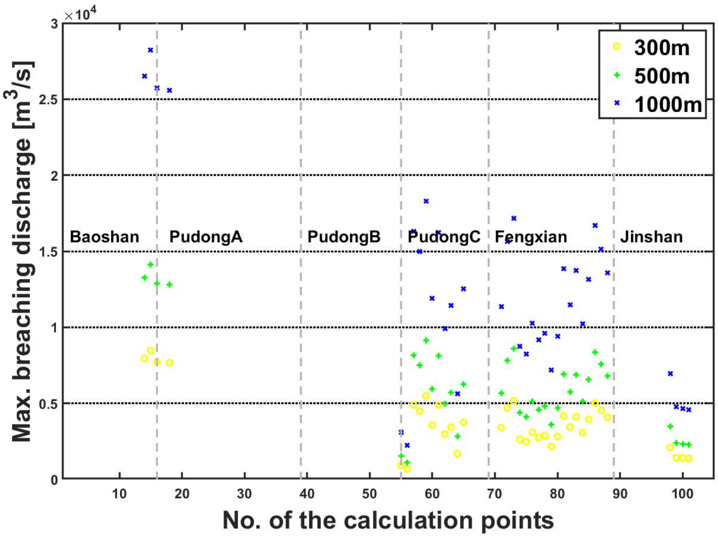

Fig. 5.12.: Breaching location and maximum breach discharge with different breach width along Shanghai sea dike in case R4.5

5.6.1 Overtopping only

During typhoon events under historical climate conditions, there is no breaching in either reference case and the past case in scenario R7.9, R3.4, R2.9 and R1.0. The inundation map is mainly depended on the overtopping. As shown in Fig. 5.13, Fig. 5.14, Fig. 5.15 and Fig. 5.16, it can hardly see the inundation area. However, for future cases, only scenario R18.3 does not have breaching situation. The inundation in R18.3 locates at some points on the east of Shanghai. The river water level is also raised by the overtopping discharge at Dazhihe and Wuhaogou sluice (sluices location seen in Fig. 3.13).

Tab. 5.3 is a summary of the inundation areas with different maximum inundation depths for overtopping only cases. The ratio here means the ratio of the total inundation depth and the simulated area. Among these overtopping only cases, the only future case R18.3 has the largest inundation areas. There are altogether 316 km^2 inundation area, which is 5.8% of the simulated area in Shanghai. For other cases, the inundation percentage ranges from 3.4% to 4.4%. For historical climate events R7.9, R3.4, R2.9and R1.0, they are not likely to breach in either reference nor past case. And the past cases have larger inundation area than the reference cases for all different inundation depths in all mentioned historcial climate events.

Tab. 5.2.: Overland simulation cases

Scenarios		Overtopping only	Overtopping+breaching		
			Breach width [m]		
			300	500	1000
R7.9	Reference case	✓			
	Past case	✓			
R3.4	Reference case	✓			
	Past case	✓			
R2.9	Reference case	✓			
	Past case	✓			
R1.3	Reference case		✓		
	Past case		✓		
R1.0	Reference case	✓			
	Past case	✓			
R18.3	Future case		✓		
R8.0	Future case	✓			
R6.8	Future case		✓		
R3.6	Future case		✓		
R4.5	Future case		✓	✓	✓

Tab. 5.3.: Inundation areas classified by maximum inundation depth for overtopping only cases. Ratio means the ratio of the total inundation depth and the simulated area.

Scenarios		Inundation area [km^2]						Ratio
		Inundation depth [m]					total	
		0-0.2	0.2-0.5	0.5-1	1-3	>3		
Reference case	R7.9	184	0	0	0	0	184	3.4%
	R3.4	195	8	2	1	0	205	3.8%
	R2.9	202	4	2	2	0	210	3.9%
	R1.0	186	0	0	0	0	186	3.4%
Past case	R7.9	201	1	0	0	0	202	3.7%
	R3.4	220	5	9	2	1	236	4.4%
	R2.9	210	14	2	4	0	230	4.2%
	R1.0	187	0	0	0	0	187	3.4%
Future case	R18.3	88	176	35	17	1	316	5.8%

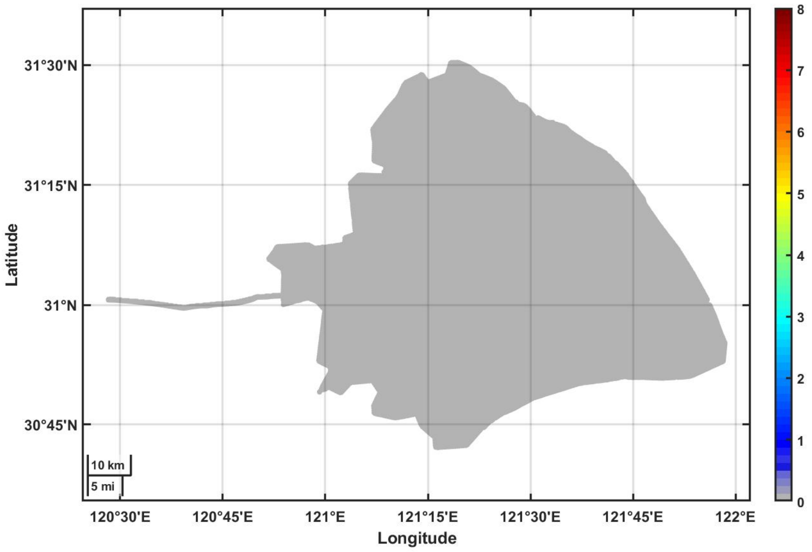

(a) reference case

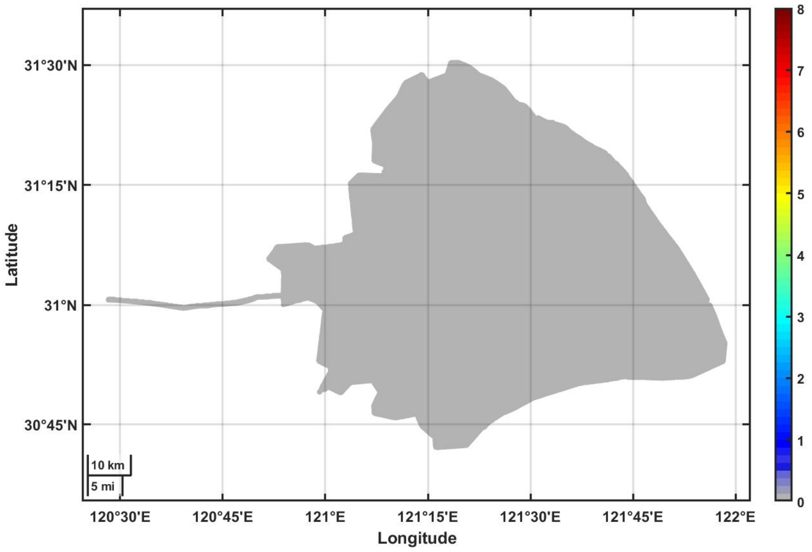

(b) past case

Fig. 5.13.: Inundation map in case R7.9

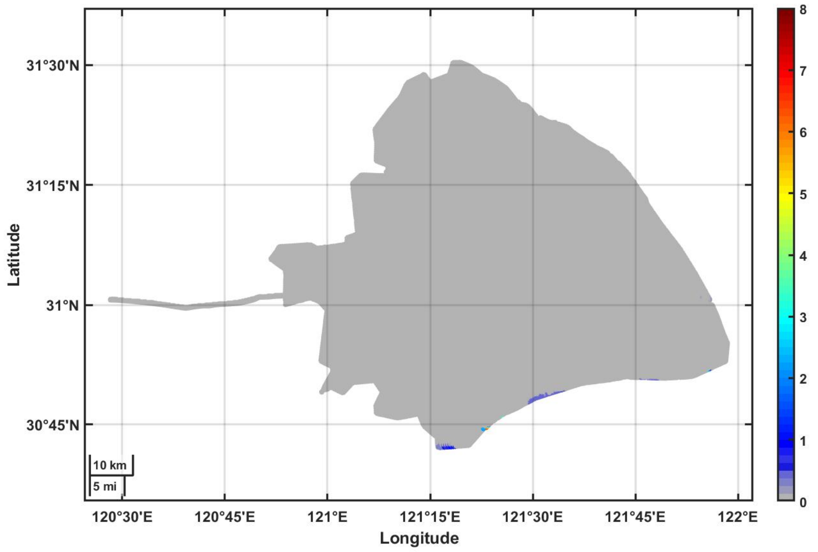

(a) reference case

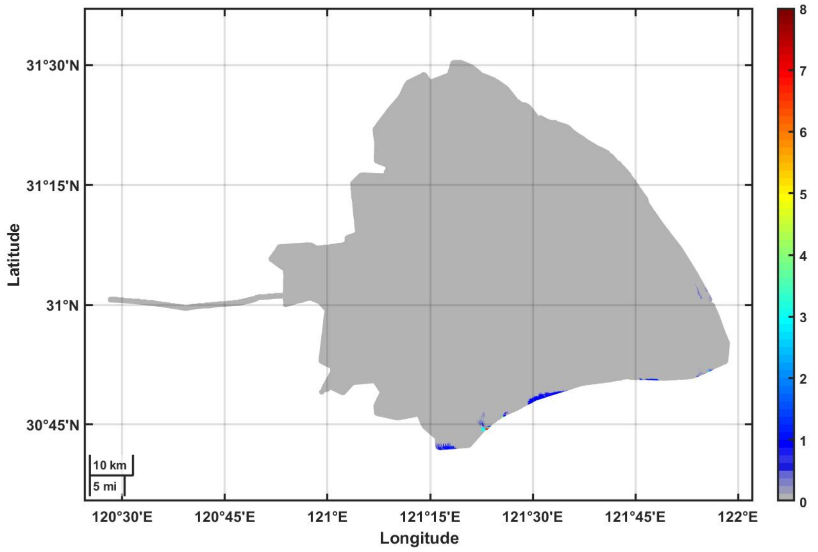

(b) past case

Fig. 5.14.: Inundation map in case R3.4

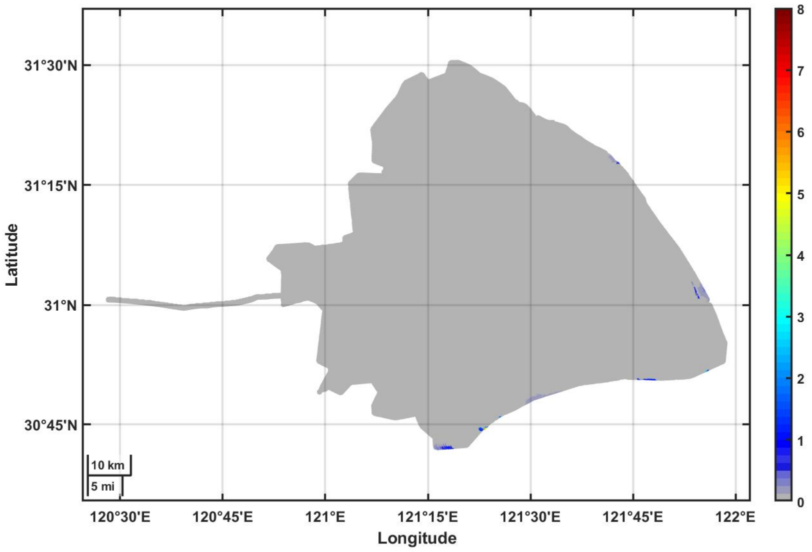

(a) reference case

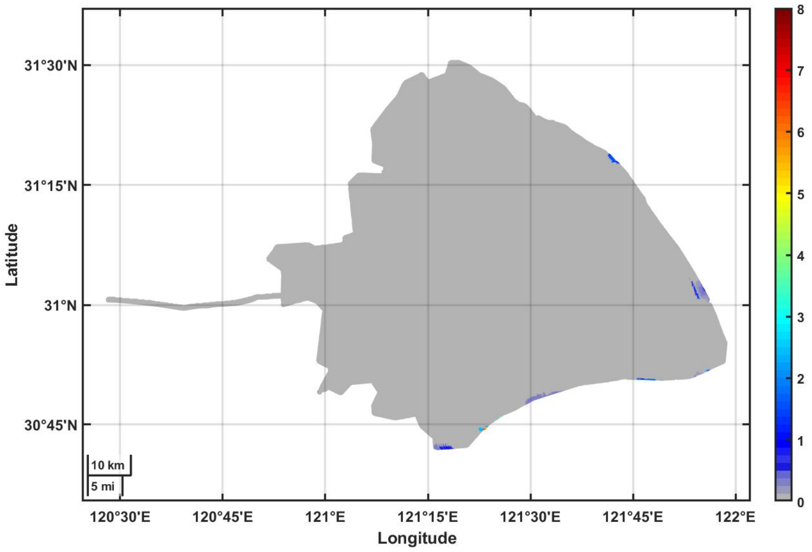

(b) past case

Fig. 5.15.: Inundation map in case R2.9

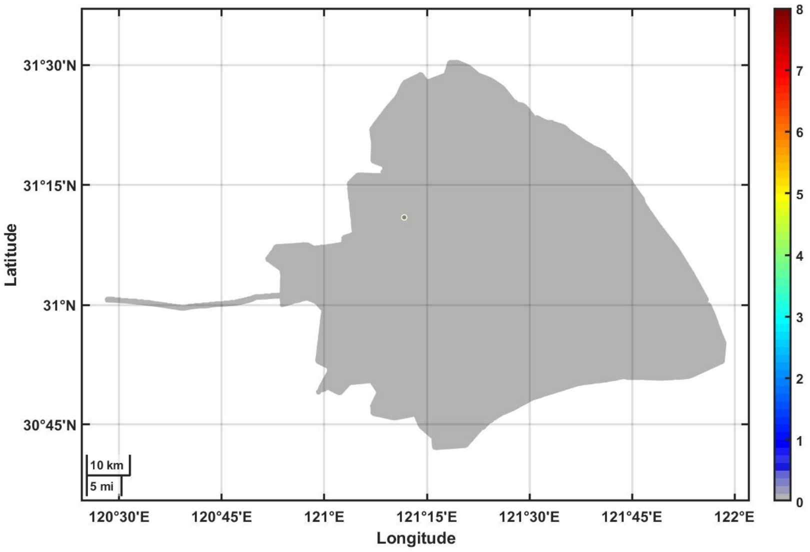

(a) reference case

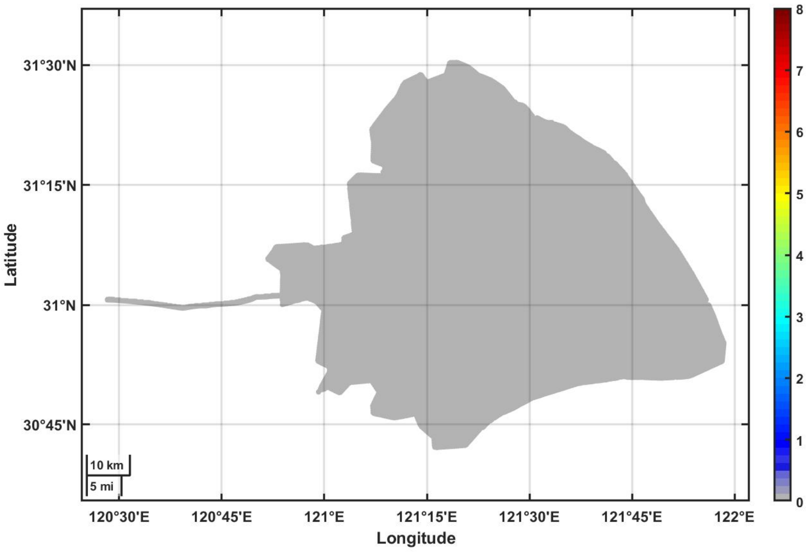

(b) past case

Fig. 5.16.: Inundation map in case R1.0

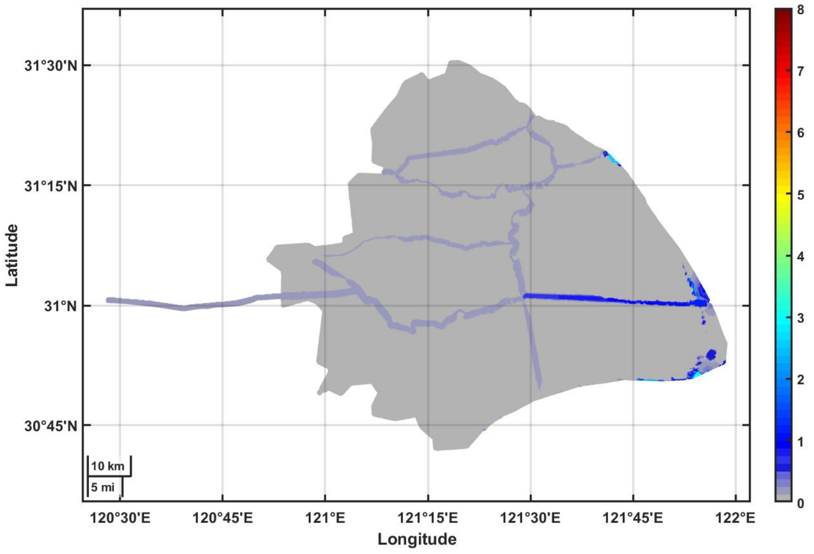

Fig. 5.17.: Inundation map in case R18.3 (B=300m)

5.6.2 Overtopping plus breaching

Tab. 5.4 is a summary of the inundation areas with different maximum inundation depths for overtopping plus breaching cases.

For the hypothetical events under historcial climate condition, only scenario R1.3 shows breaching points in both reference and past cases. As shown in Fig. 5.18, the breaching points locate along Hangzhou Bay, so does the inundation area. Besides, there is also some places flooding at the entrance of Shanghai Yangtze River Tunnel. For the case R1.3, the past case has an approximate three times inundation area of the reference one.

For the future cases, the inundation area also locates along Hangzhou Bay and near the entrance of Shanghai Yangtze river tunnel in case R8.0 and R6.8 shown in Fig. 5.19 (a) and (b). The inundation depth is relative higher in Jinshan District and Fengxian District for these two cases. However, for case R3.6 (Fig. 5.19 (c))and R4.5 (Fig. 5.20 (a)), the inundation area spread to almost along the coast. For case R3.6, higher inundation depth is mainly distributed in Jinshan District, Fengxian District and near the entrance of Shanghai Yangtze River Tunnel. For case R4.5, the inundation at the south-east corner of Shanghai is worse. Rivers share and bring water to further inland area, so some places near the river are also flooded.

The results of inundation in case R4.5 are shown in Fig. 5.20 with different breach widths of 300 m, 500 m and 1,000 m. It is obvious that the increasing of breach

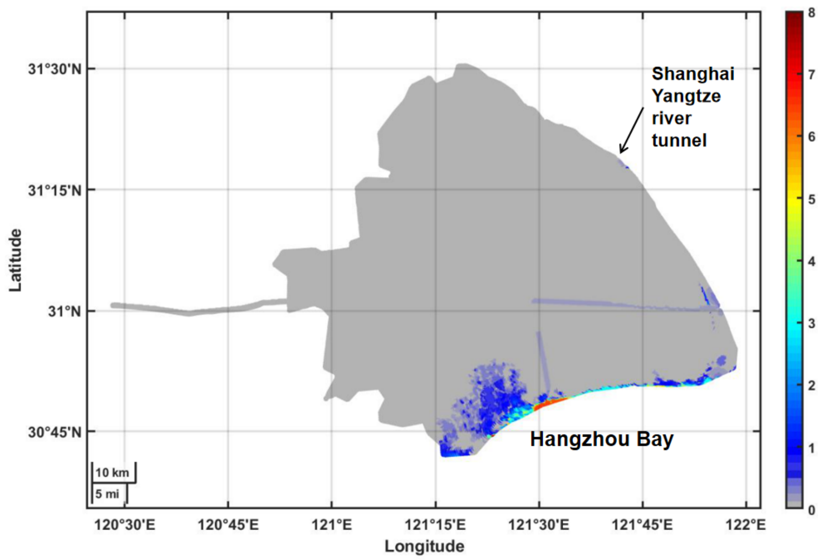

(a) reference case,B=300m

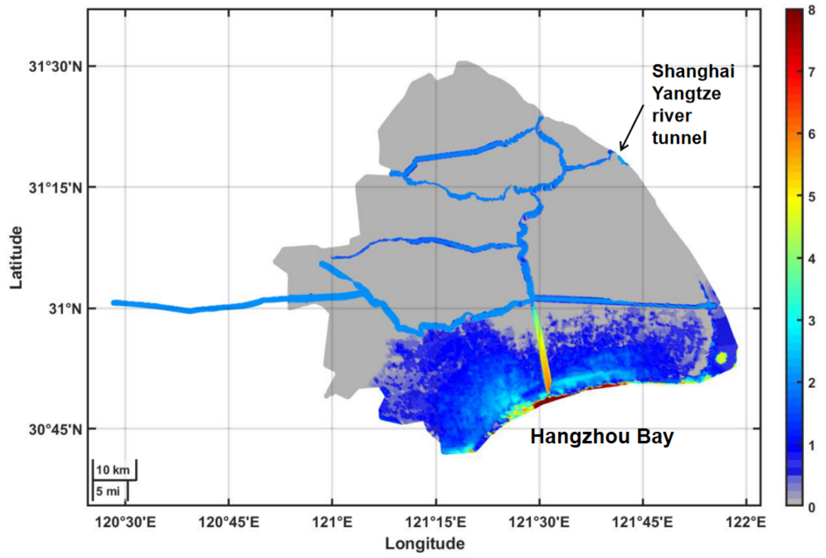

(b) past case,B=300m

Fig. 5.18.: Inundation map in case R1.3

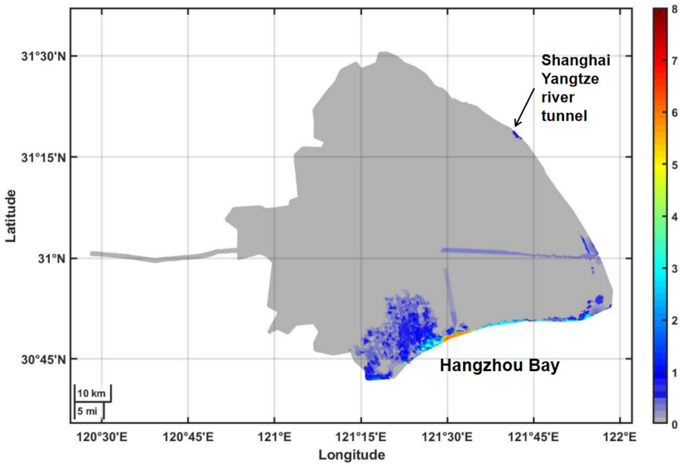

(a) case R8.0,B=300m

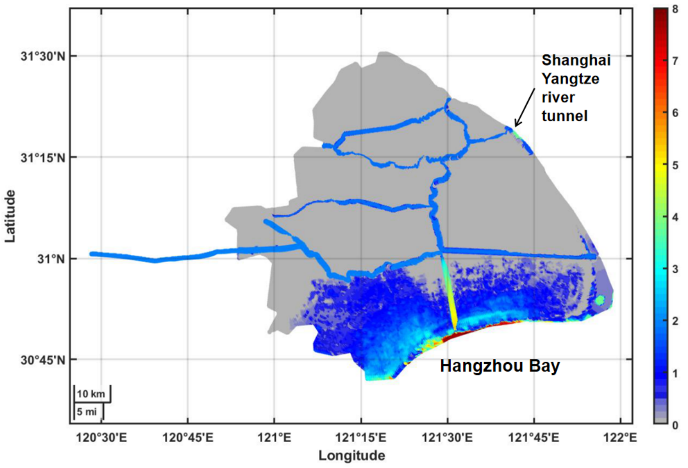

(b) case R6.8,B=300m

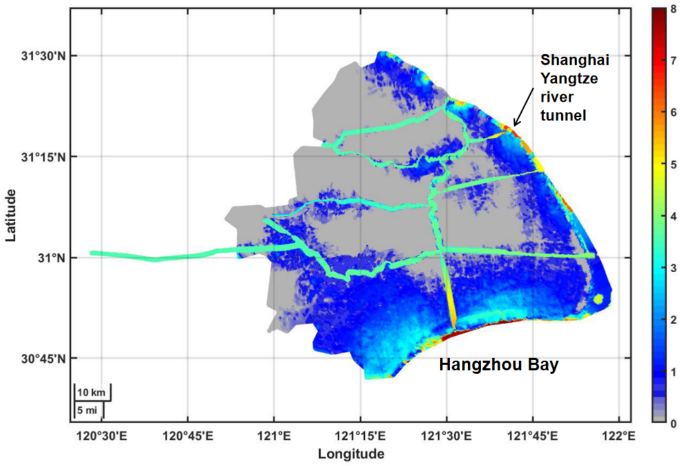

(c) case R3.6,B=300m

Fig. 5.19.: Inundation map in future cases

Tab. 5.4.: Inundation areas classified by maximum inundation depth for overtopping plus breaching cases. Ratio means the ratio of the total inundation depth and the simulated area.

Scenarios		Breach width [m]	Inundation area [km^2]						Ratio
			Inundation depth [m]					total	
			0-0.2	0.2-0.5	0.5-1	1-3	>3		
Reference case	R1.3	300	263	161	79	31	22	556	10.2%
Past case	R1.3	300	104	293	566	779	63	1,805	33.3%
Future case	R8.0	300	275	217	111	31	21	655	12.1%
	R6.8	300	138	323	551	779	65	1,855	34.2%
	R3.6	300	355	586	1,021	1,254	337	3,553	65.5%
	R4.5	300	327	526	1,047	1,154	333	3,387	62.4%
	R4.5	500	308	614	1,117	1,270	391	3,700	68.2%
	R4.5	1,000	274	695	1,307	1,518	587	4,381	80.7%

width can result in a larger inundation area. However, as the breach width growing, the increase of the inundation area become less. Shown in Tab. 5.4, from a breach width increase of 200 m (from 300 m to 500 m), the inundation area growth is 313 km^2, e.g. 156 km^2 per 100 m breach width. From a breach width increase of 500 m (from 500 m to 1,000 m), the inundation area growth is 680 km^2, e.g. 136 km^2 per 100m breach width. Some parts on the south-east of Shanghai have a deeper inundation depth when the breach width grows.

5.6.3 Inundation process

Fig. 5.21 and Fig. 5.22 show the inundation areas and volumes with different inundation depths during future case R4.5 with the breach width of 300 m. From the beginning to 60 h, the inundation depth of 0-0.2 m has the largest inundation area. During this period, overtopping is the main cause of the inundation, and the inundation volume is still at a low level. And the inundation area can hardly be seen in Fig. 5.23 (a) and (b). From 60 h, some places of along the Hangzhou Bay start to breach (shown in Fig. 5.23 (c)), the inundation area as well as the inundation volume with the depth higher than 0.2 m increase rapidly after then. Among them, area and volume of the depth of 1-3 m rise the fastest. After reaching the peak at 78 h for both area (10.65×10^8 m^2) and volume (17.58×10^8 m^3), the lines go down as the flood spreads more places in Shanghai (shown in Fig. 5.23 (f)), so the lines for depth lower than 1 m raise at the same time. The depth for more than 3 m is also raising, but as shown in Fig. 5.23 (f), most of the places have inundation depth higher than 3 m are the rivers rather than the land. After 100 h, the effects of the

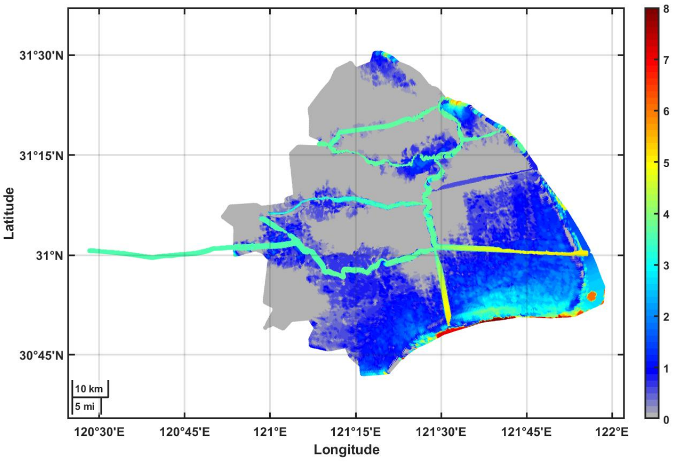

(a) future case,B=300m

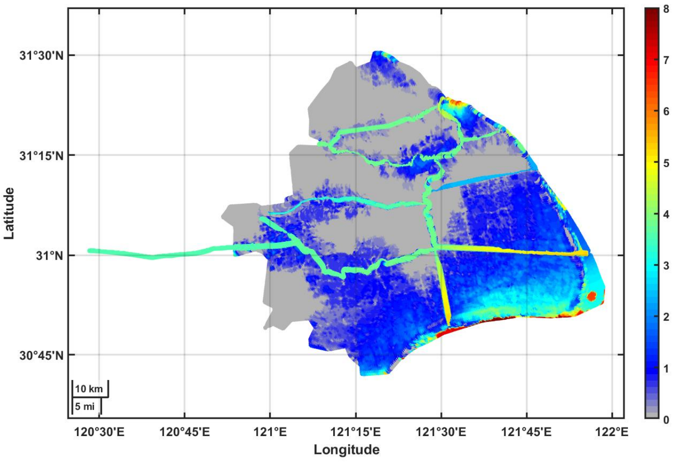

(b) future case,B=500m

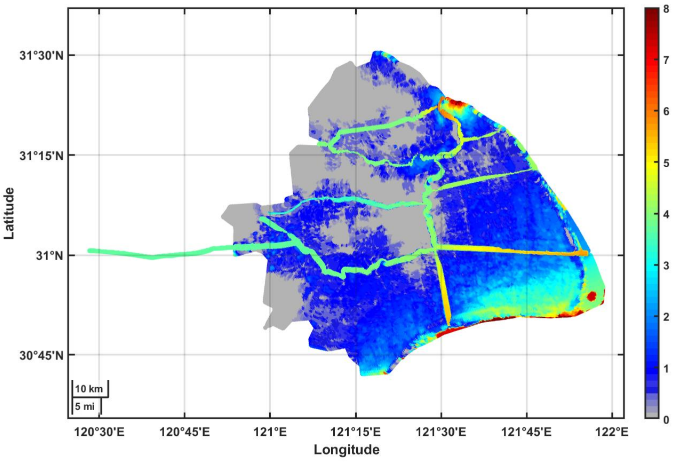

(c) future case,B=1,000m

Fig. 5.20.: Inundation map with different breach width in case R4.5

storm nearly disappear, so the area for depth 1-3 m keeps lowing down. However, as the water keeps spreading as shown in Fig. 5.24, the area for depth lower than 1m increases and area for the depth higher than 3 m keeps still.

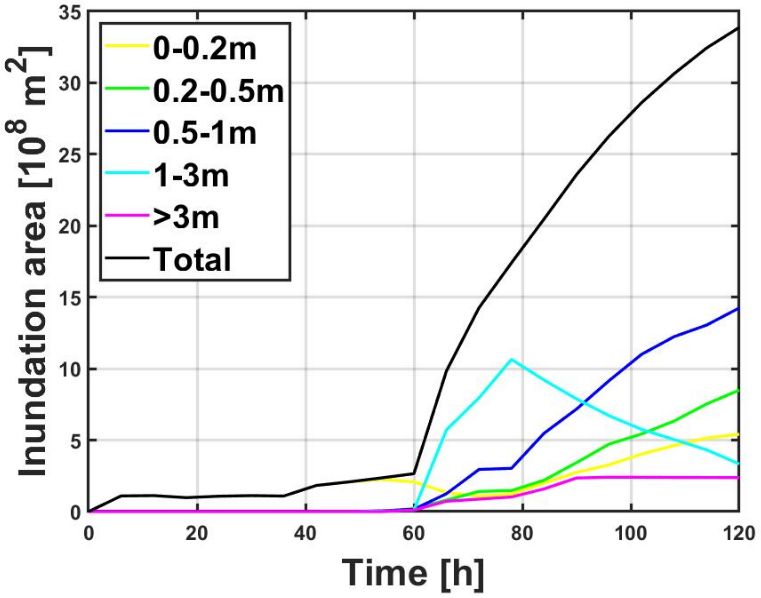

Fig. 5.21.: Inundation areas with different inundation depths during future case R4.5 (B=300m)

5.7 Summary

In this chapter, the results of climate change cases are shown for every model and method used in this research.

The result of each step has a connection with each other. In general, future climate cases have more substantial water level and significant wave height than the past climate cases along the coast. So the related overtopping rate and breaching rate are more significant. Then the result of inundation situation is worse. The wind speed return period does not show explicit effects on the results. The factors that influence the final result will be discussed in detail in the next chapter.

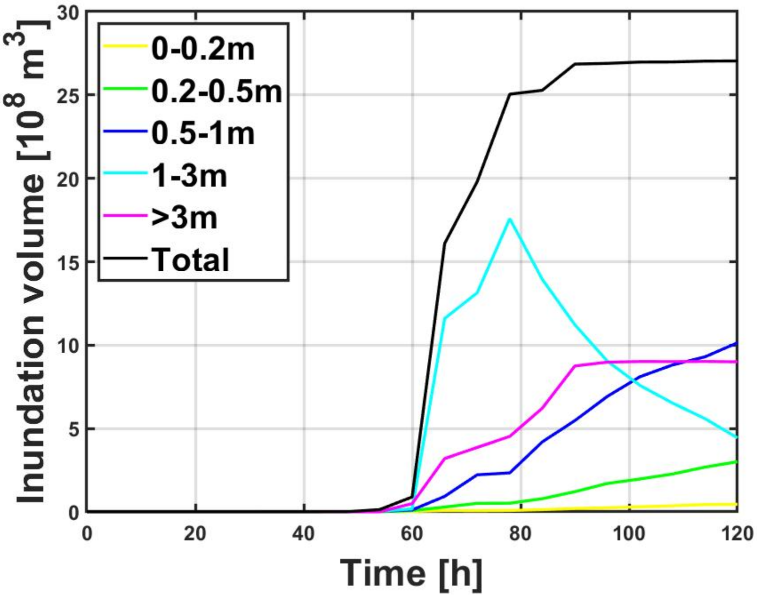

Fig. 5.22.: Inundation volumes with different inundation depths during future case R4.5 (B=300m)

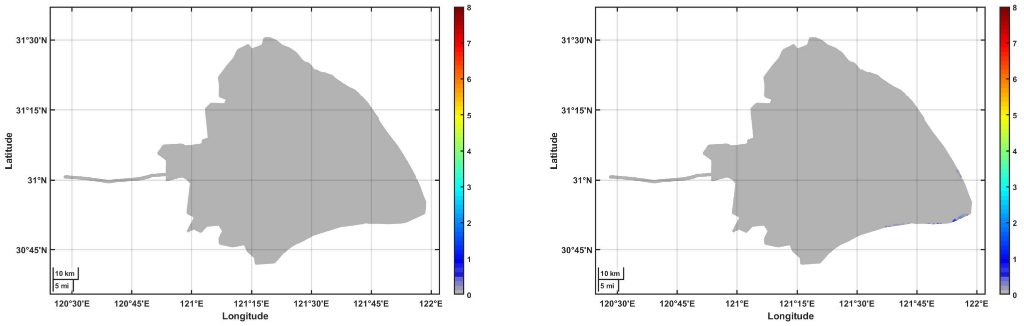

(a) 30h (b) 50h

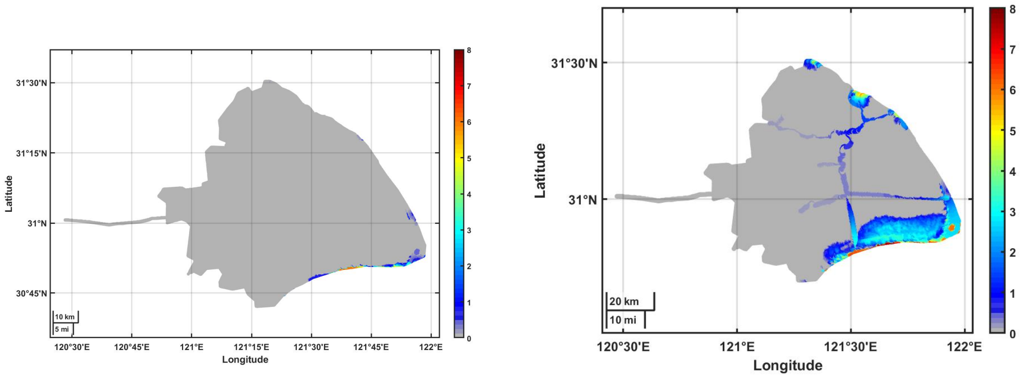

(c) 60h (d) 66h

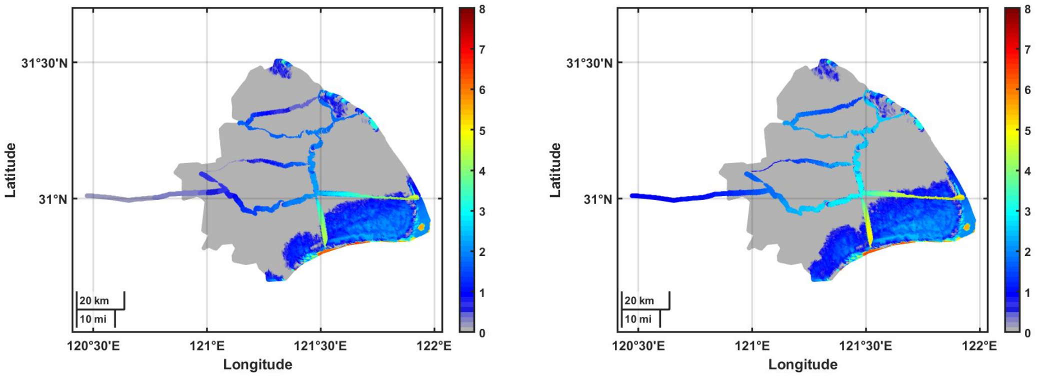

(e) 72h (f) 78h

Fig. 5.23.: Inundation process in case R4.5 (B=300 m) (part 1)

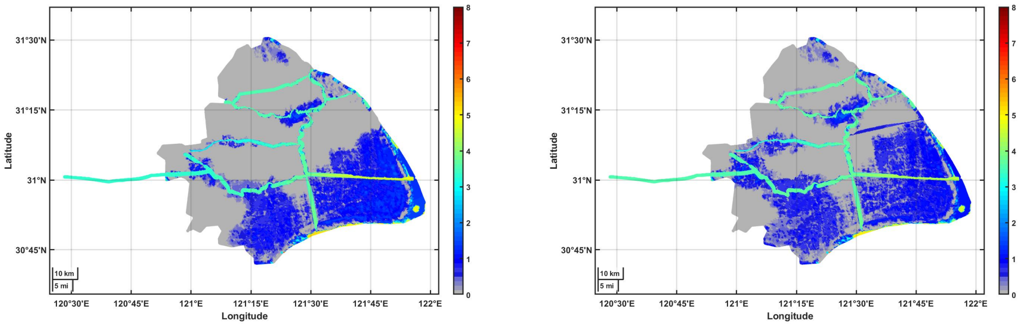

(a) 100h

(b) 120h

Fig. 5.24.: Inundation process in case R4.5 (B=300 m) (part 2)

Discussion

6

6.1 Introduction

In this chapter, the limitations of the methodology are discussed. Uncertainties of each step of this research are mentioned in Section 6.2. Then, some important results in the previous section are summarised to analyze how different factors contribute the inundation result in Section 6.3. The effects of climate change and land subsidence are generally mentioned in Section 6.3.1. After that, sea dike subsidence is discussed separately in Section 6.3.2. Then, typhoon effects are discussed in Section 6.3.3. Finally, the breach wdith effects are analyzed in Section 6.3.4.

6.2 Discussion of methodology

6.2.1 Hydrodynamic model and wave model

In this research, the hydrodynamic model and wave model affect the inundation result by providing the water level and wave parameters along Shanghai coast. There are some uncertainties throughout the whole process.

Validation of the hydrodynamic model and wave model

The validation results of the hydrodynamic model and the wave model are shown in Chapter 3. The RMSE results of wave level and significant wave height seem reasonable. However, some uncertainties still exist.

In the validation of hydrodynamic model, for the tide level only, the RMSE is around 20 cm according to the results in Section 3.3.2 for different years. The tide level seems insensitive with the local estuary bathymetry according to Tab. 3.2.

The meteorological forcing involves in hydrodynamic model and wave model. The wind and pressure fields generated by the typhoon model are used and only used in the validation of two models. The validation of the wind speed has been made for typhoon Lekima in Section 3.2.3. The result shows evident overestimation on the wind velocity around the top values. Cause there is no corresponded water level and wave parameters provided during typhoon Lekima, it is hard to say how this overestimation finally affect the water level and wave parameter results. For the validation of water level during typhoon Winnie, most of the water level peaks are underestimated, shown in Fig. B.11 and Fig. B.12. According to the validation of the wave model in Section 3.4.2, the significant wave height may be underestimated by the model when there is another typhoon event approaching around the same time.

Other uncertainties

In this research, storm, tide and wave affect the final inundation results by influencing the wave parameter and water level along the coast. The water depth at the toe structure applied to the overtopping calculation is calculated as the sum of water depth simulated by hydrodynamic model and the wave set-up (see in Section 3.5). Since the wave set-up cannot be simulated in spherical coordinate system by Delft3D, it is assumed to be 5% of the significant wave height modelled at the observation points according to the references in Section 2.7.3. In this process, there are some uncertainties:

1 The hydrodynamic model and wave model are not coupled in this research, and the wave simulation is based on still water level rather than the water level affected by storm and spring tide. The effect is more significant nearshore, where wave height is more sensitive to the water depth. That means, the modelled significant wave height may be underestimated for the underestimation of the water depth.

2 The modelled spring tide levels in 1997 at the boundaries are applied as the tide level boundaries for hypothetical events. Since there is a distance from the boundary to the coast, it is hard to control the highest tide meet the surge right at somewhere along the coast.

3 The wave set-up assumption is based on reference and experience. The result can be more reliable if the recorded wave set-up and local significant wave height can be provided.

6.2.2 Calculation points

There are two sets of calculation points. One is for the hydrodynamic model and wave model; the other is for the overtopping and breaching calculation. The relation between these two sets of points have explained in Section 4.5. An assumption has been made that each hydrodynamic calculation point has a related fixed calculation point along the coastline on land representing the sea dike over there. The lines of the connection of two related points are almost perpendicular to the coastline. However, in reality, wave and tide are not always normally incident, and the points for hydrodynamic models still have a distance from the actual location of the toe structure. If the distribution of the toe structure is provided, the results can be more reliable.

6.2.3 Overtopping calculation

In this research, the overtopping is calculated by Eq. 2.31 in Section. 2.8.2. Despite the water level and wave parameters achieved from hydrodynamic model and wave model, there is an error from the method itself. This method does not consider the effect of the berm or the incident angle of waves, which are considered by overtopping calculation in EurOtop (2016). The differences between these two methods can be compared in Shanghai case for further study. Besides, the validation of overtopping is only based on historical observation. For the lack of accurate records, such validation is reasonable but not reliable.

6.2.4 Breaching calculation

In this research, the threshold for breaching is the overtopping rate higher than 0.1 $m^3/m/s$. This value is overestimated by the overtopping result, historical observation and physical experiment reference. In reality, the sea dike breaching is complicated. Even though overtopping is the primary failure mechanism, the breaching is mainly based on a range of overtopping rate rather than just one value. Actually, additional researches are needed to achieve a more reliable range, including large-scale model experiments and prototype measurements.

Besides, it is assumed in Section 2.9.2 that the breaching process takes place in a relatively short period and that the final breach dimensions are achieved soon after the start of the breaching. It is also assumed that the breach in Shanghai sea embankment is a type A breach. The actual process must be more complicated, and it may be different breaching types for different places along Shanghai sea dike. More work can be done with detailed soil material provided along the sea dike.

6.2.5 Overland simulation

An assumption of overland simulation is that there is no drainage during typhoons in Shanghai. This assumption is reasonable because it is hard for water to drain when the tide level is high. Another assumption is that all the sluices are closed, and the discharge in Wusong River is 0 m^3/s (see in Section 3.7.1). This assumption is made due to the lack of discharge information during storm events. In this way, the model gets rid of the effect of upstream river. The flood only comes from the coastal side.

6.3 The effect of composite factors on Shanghai coastal flood

In order to answer the research questions in Section 1.2, the model results in Chapter 5 are analyzed for different aspects.

6.3.1 Effects of climate change and land subsidence

Future cases and past cases experience different climate and land elevation condition, which is one of the factors affecting the inundation condition. In general, future cases have lower sea dike and land elevation than in past cases. The water level along Shanghai sea embankments are relatively higher for future cases. So the future cases are more likely to breach and resulting in larger inundation area and deeper inundation depth than the past cases.

If only overtopping happens, the inundation area for past cases is around 4% of the simulated area, according to Tab. 5.3. Furthermore, most of the inundation area has a depth lower than 0.2 m. The only future case R18.3 has larger inundation areas than in past cases. There are altogether 316 km^2 inundation area, which is 5.8% of the simulated area in Shanghai. The ratio for the area with higher depth is also more substantial than the past cases.

When it comes to the breaching cases (see in Tab. 5.4), the inundation areas are higher than the overtopping only cases. Considering the breach width of 300 m only, even though past case R1.3 has a higher inundation area (1,805 km^2, 33.3% of the simulated area in Shanghai) than the future case R8.0 (655 km^2, 12.1% of the simulated area in Shanghai), it is still lower than future case R6.8, R4.5 and R3.6 (1,855 km^2, 3,388 km^2 and 3,553 km^2 respectively). For the same breach width, inundation area of future case R3.6 and R4.5 is about twice of that in past case R1.3.

For the past case R1.3 and the future case R6.8, the southern part of Shanghai is flooded. For case R3.6 and R4.5, most of the places in Shanghai coast are flooded. Shown in Fig. 5.23, the breach starts along Hangzhou Bay, and the inundation area generally spreads from south to north. Areas along Hangzhou Bay seem the vulnerable places for inundation.

Rivers also play a role in transporting water, resulting in inundation for some places along the river. This situation is visible in future cases R3.6 and R4.5, which have large inundation volumes.

6.3.2 Sea dike subsidence

In the previous section, the differences between future cases and past cases are discussed. The future case conditions are of course predicted. For the lack of elevation condition, the past case conditions are also not the actual conditions in the past. To study how reliable the past case conditions are, a comparison is made between the past case and the reference case.

The only difference between the past and reference case in Section 4.4 is the dike elevation. The past is the elevation measured from the field work going back to 10 years ago. The reference case is achieved by the typical sea embankment cross-sections in Section 2.4.2. The elevation changing in this research only takes the neotectonic subsidence into consideration, which may result in an underestimation of the land subsidence speed. According the difference results of case R1.3 in reference and past condition (see in Fig. 5.18 and Tab. 5.4 in Section 5.6), the past case shows obvious worse result than the reference case. It indicates that the anthropogenic subsidence also plays an important role even though there is some construction work for Shanghai sea embankments.

6.3.3 Typhoon effects

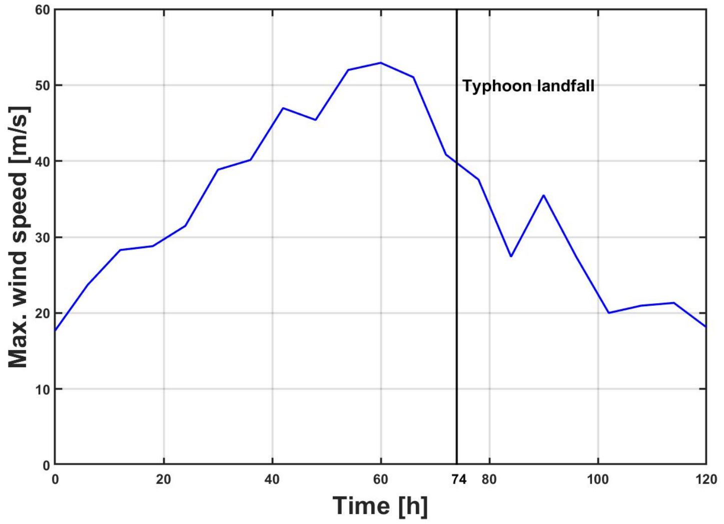

Fig. 6.1.: Maximum wind speed during future case R4.5 (every 6 h)

The effects of a typhoon on inundation is achieved indirectly from the effects of the typhoon on hydrodynamic model and wave model. As typhoon is a crucial factor contributing to inundation, its effects are discussed separately in this section.

Typhoon affects the overland inundation during the whole event. Here take future case R4.5 as an example. Fig. 6.1 shows the maximum wind speed during future case R4.5 with an interval of 6 h. The maximum wind speed here means the maximum wind speed in the Shanghai area of responsibility (26°N-34°N, 117°E-127°E). The maximum wind speed can represent typhoon intensity to some extent. After reaching the maximum wind speed around 60 h, a typhoon hits Shanghai coast around 74 h. Then the wind speed decreases generally. In Fig. 5.22 in Section 5.6.3, the inundation volume shows relation with the wind speed and location. The total inundation volume shows a significant increase from 60 h, which results from sea dike breaching. The total inundation volume increases rapidly from 60 h to 80 h. It is reasonable because typhoon makes landfall in Shanghai during this period. After the rapid increase, the growth of total inundation volume slow down and then accelerate a little bit around 90 h. This acceleration keeps pace with the increase of wind speed during the corresponded period in Fig. 6.1. After 100 h, the effects of the storm nearly disappear, and the total inundation volume almost keeps still.

Among inundation volume of different inundation depths, the inundation volume of depth 1-3 m generally shows sensitive inundation reaction inland to the typhoon.

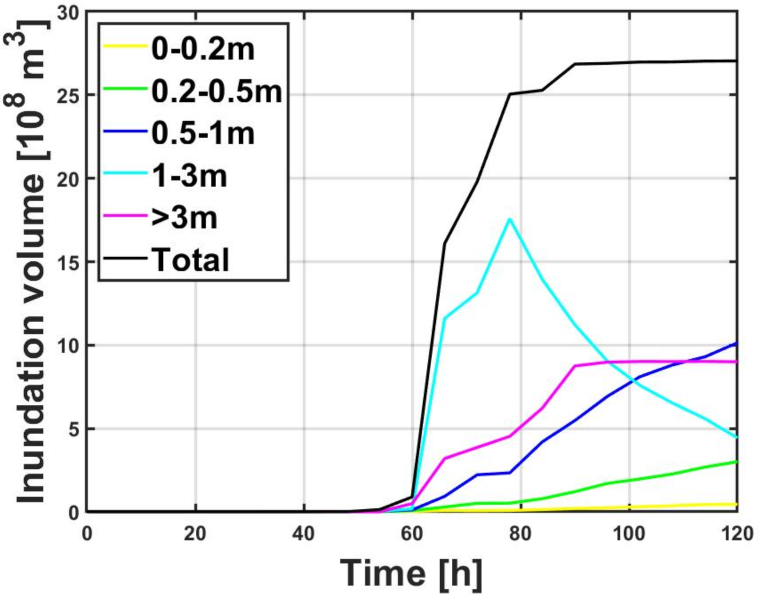

Fig. 6.2.: Inundation volumes with different inundation depths during future case R4.5 (B=300m)

Most of the places have inundation depth higher than 3 m are the rivers or lakes rather than the land according to the results in Section 5.6.3.

The return period of the maximum wind speed reflects the intensity of typhoon to some extent. However, it does not show an explicit effect on the inundation for all the cases in this research. In Section 4.2, case R7.9 and R18.3 rank the first place of return period in historical climate and future climate respectively. However, they do not even cause breaching scenarios.

Another important storm factor is the typhoon track. As shown in Fig. 4.1 and 4.2. For the historical climate cases, R7.9, R3.4 and R1.0 do not hit Shanghai coast directly, that may be the reason for no breaching in these cases. R2.9 and R1.3 hit Shanghai coast almost at the same place. Even though R2.9 has a higher wind speed return period, it does not show the same threat as R1.3 to Shanghai coast. It is because typhoon in case R2.9 is weakened when hovering in the ocean. For the future climate cases, the landfall locations of R18.3 and R8.0 are far away from Shanghai, so the inundation effects on Shanghai is not big. R6.8, R4.5 and R3.6 all land on Shanghai coast. R6.8 lands at a north-east part while the latter two land almost at the same place at Hangzhou Bay. Even though R6.8 has a larger return period, the inundation result is worse in case R4.5 and R3.6. It may result from the relative low sea embankments along Hangzhou Bay.

6.3.4 Breach width effects

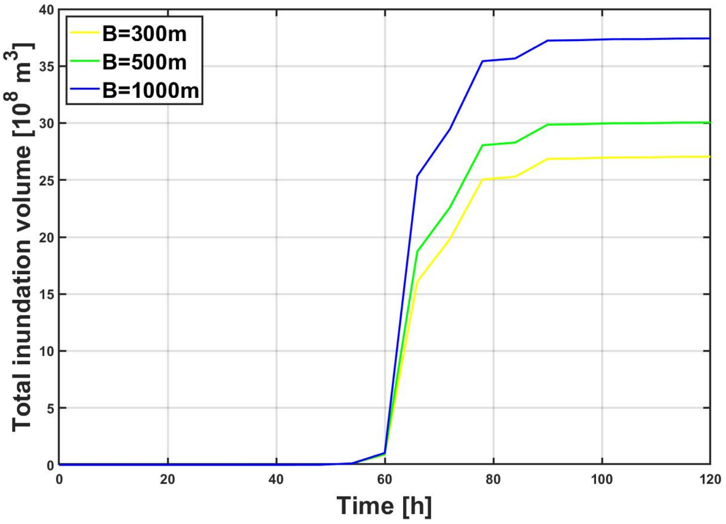

Fig. 6.3.: Total inundation volume during case R4.5 with different breach widths

Due to a lack of data of historical breaching events, potential breach widths can only be roughly estimated. So the breach widths are estimated at 300 m, and to determine the sensitivity of this estimation, also at 500 m and 1,000 m.

According to Fig. 5.20, the increase of breach width does result in a larger maximum inundation area. However, as the breach width increases, the increase of the inundation area becomes less. Shown in Tab. 5.4, from a breach width increase of 200 m (from 300 m to 500 m), the inundation area growth is 313 km^2, e.g. 156 km^2 per 100 m breach width. From a breach width increase of 500 m (from 500 m to 1,000 m), the inundation area growth is 680 km^2, e.g. 136 km^2 per 100 m breach width.

Total inundation volume during case R4.5 with different breach widths is shown in Fig. 6.3. In general, the total inundation volumes for different breach widths have a similar variational tendency, which results from the effect of the same typhoon. Moreover, the breach width affects the magnitude of volume. The influence of breach width on inundation situation is different for different stages.

In the early stage of breaching (60-66 h), the total inundation volume increases rapidly for different breach widths. There are some differences for the total inundation volume with different breach width. Notably, the inundation volume with depth 1-3 m is almost the same for different breach widths from 60 h to 66 h. Inundation volumes for inundation depth of 1-3 m are 11.60×10^8 m^3, 12.40×10^8

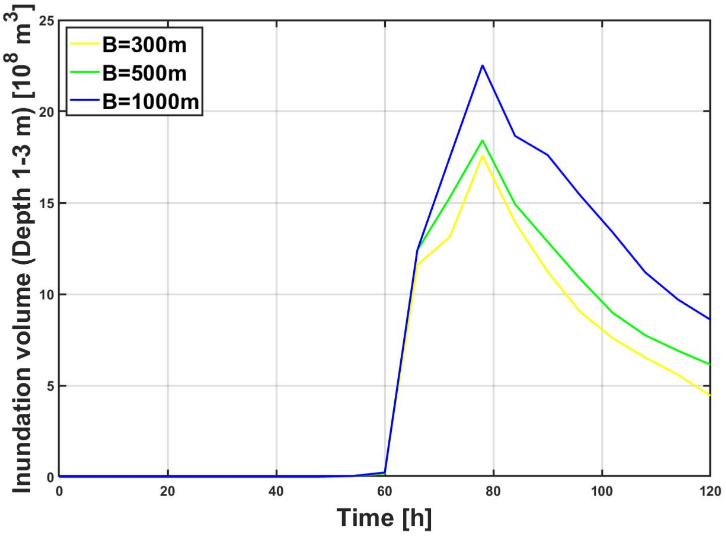

Fig. 6.4.: Inundation volume with depth 1-3 m during case R4.5 with different breach widths

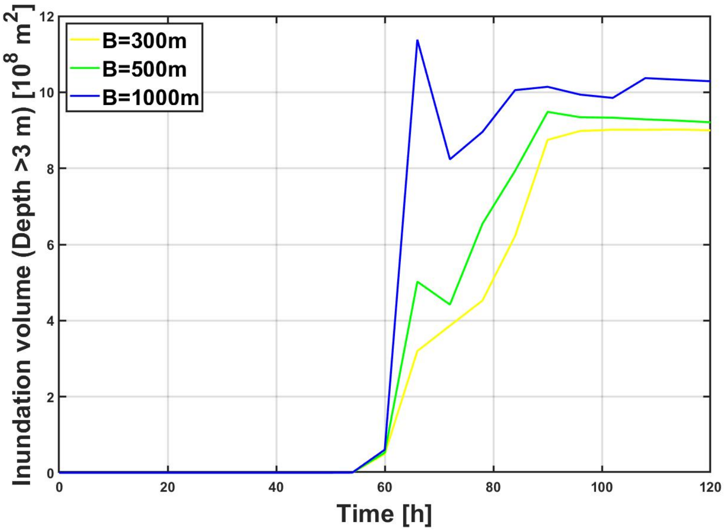

Fig. 6.5.: Inundation volume with depth higher than 3 m during case R4.5

m^3 and 12.41×10^8 m^3 for the breach width of 300 m, 500 m and 1000 m at 66 h respectively. Instead, the inundation volume differences mainly come from the one with depth higher than 3 m (shown in Fig. 6.5), which is also visible in Fig. 5.23 (d) in Section 5.6.3, Fig. B.21 (b) and Fig. B.22 (b) in Appendix B. At 66 h, the inundation focuses on the south-east part of Shanghai, places near Wusongkou and rivers in Shanghai are also affected. The inundation volumes for depth higher than 3 m are 3.20×10^8 m^3, 5.02×10^8 m^3 and 11.38×10^8 m^3 for the breach width of 300 m, 500 m and 1000 m at 66 h respectively. Here the breach widths show significant effects on inundation which may result in serious damage.

During 66 h to 78 h, the total inundation volumes keep increase for different breach widths. For depth higher than 3 m, it is interesting to note that the inundation volume with breach width of 300 m still increases, however, the volumes with breach width of 500 m and 1000 m have decreased at 72 h. In 72 h, part of the places with inundation depth higher than 3 m are the rivers or lakes for cases with different breach widths. River and lake prevent the land from severe flooding to some extent. However, rivers and lakes have the limitation of water storage, and they need time to transport. For the breach width of 500 m and 1000 m, the inundation volume is too large to be transported into rivers and lakes in a short time. Flood spreads at the same time, so the inundation volume higher than 3 m decreases rapidly, and more low-level inundation places can be found overland. It can also explain the visible difference of inundation volumes with different breach widths for depth 1-3 m from 66 h to 78 h.

After 78 h, the typhoon has reduced its intensity, and the corresponded total inundation volumes almost have no change except for the small increase from 84 h to 90 h. For the depth 1-3 m, the inundation volumes keep lowing down for different breach widths. For the depth deeper than 3 m, the inundation volumes for different breach widths raise with different speeds till 90 h then almost keep still after that. These curves reflect the rivers and lakes responses in reality. With so much flood overland, more and more water flows into rivers and lakes and rise the water level over there as time goes on. When the typhoon is weakened, less flood comes inland, the source of water flowing into the rivers and lakes are also reduced. From 90 h to 120 h, the difference of inundation volume for depth deeper than 3 m among different breach widths is not great. It may result from the limitation of river storage capacity.

6.4 Summary

In this chapter, the limitations of the methodology are discussed. The effects of composite factors on Shanghai coastal flood are also summarised. These discussions are helpful to draw the final conclusions in the next chapter.

7

Conclusions and recommendations

7.1 Conclusions

In general, the objectives of the research have been achieved by the following steps: model set-up, calibration and validation for the hydrodynamic model near Shanghai coast with D-Flow module in Delft3D-FM; model set-up and validation for the wave model near Shanghai coast with D-Wave module in Delft3D; calculate overtopping and breach discharge along Shanghai coast; set-up and apply the overland simulation in Shanghai city.

The methodology of this research can be summarised as follows:

1 In the validating period of the hydrodynamic model, typhoons in this area are represented by wind and pressure field, which are generated from typhoon tracks by WES and based on Holland's model. The RMSE is about 3.7 m/s for the wind model.

2 A hydrodynamic model has been set up close to the coast of Shanghai. Calibration and validation of tide level have been done for the model. The validation shows that the RMSE is about 0.2 m for the tide level. When a typhoon is added into the model, the RMSE of the water level is about 0.4 m.

3 The hydrodynamic model has been applied to climate change storm scenarios provided by the UK Met Office. Five in these ten scenarios are based on historical climate condition around the year 2000, and the other five scenarios are based on future climate condition around the year 2100. The water level along Shanghai coast has been achieved during these cases.

4 A wave model has been set up close to the coast of Shanghai. Validation has been made only once for the limited record value. The wave model is also applied to the ten scenarios mentioned above. Wave parameters have been achieved by the model, and wave set-up has been estimated.

5 With the results from hydrodynamic model and wave model, the overtopping can be calculated based on GBT51015-2014 Chinese Guideline of Dike Design. According to experiment reference and analysis on historical events, the threshold of breaching at a point is assumed to be the overtopping rate of 0.1 $m^3/m/s$. The dike dimension also affects the overtopping result. Two sets of dike dimensions have been made. The overtopping calculation is also applied to all these ten scenarios.

6 Apply the broad-crested weir formula to dike sections that are likely to breach in different scenarios. The sensitivity of the breach width to the inundation situation has applied in the case R4.5.

8 The overland simulation model has been set up for Shanghai city. With the input of the above results, the inundation maps for scenarios on different climate conditions, land elevation and breach widths are finally achieved.

Based on research objectives and questions, the following conclusions can be achieved according to the results of the overland simulation:

1 Where are the vulnerable places to be overtopped and breached in Shanghai coast under extreme weather condition?

It is easy to know that places with high water level and low sea dike elevation are more likely to get high overtopping that can finally result in breaching. For Shanghai city, such vulnerable places can be found near the entrance of Shanghai Yangtze River Tunnel and along Hangzhou Bay. For Hangzhou Bay, places are in danger especially in Jinshan District and on the south-east corner of Shanghai. However, for some extreme cases, the whole Shanghai coast is flooded due to overtopping and dike breaching.

2 How do climate change and land subsidence affect typhoon induced inundation in Shanghai?

In general, events in the future are more likely to experience dike breaching comparing to events in past climate condition. Given the challenge of climate change, the intensity of typhoon is generally strengthen according to the simulation of the UK Met Office. Besides, the sea level is also relatively rising due to climate change and land subsidence in the future. The resulting future hydrodynamic conditions worsen the inundation situation.

For the past climate and land elevation around the year 2000 with the wind speed return period[1] of 1.3 yr, it is simulated that 23 points along the embankment are likely to breach and the breach width is assumed to be 300 m. The maximum inundation area in Shanghai can be 1,805 km^2 (33.3% of the simulated area in Shanghai). For the future climate and land elevation around the year 2100 with the wind speed return period of 4.5 yr, it is simulated that 37 points along the embankment are likely to breach and the breach width is assumed to be 300 m. The inundation area in Shanghai can be 3,388 km^2 (62.4% of the simulated area in Shanghai), which is almost twice of the inundation area around the year 2000. Among all the inundation depths, the inundation area with the depth of 0-0.2 m is 327 km^2, 0.2-0.5 m depth 526 km^2, 0.5-1 m depth 1,047 km^2, 1-3 m depth 1,154 km^2, larger than 3 m depth 33 km^2.

The breach width also affects the inundation situation. With the 500m breach width of each breach point, maximum 3,700 km^2 (68.2% of the simulation area) are flooded. With the 1,000 m breach width of each breach point, maximum 4,381 km^2 (80.7% of the simulation area) are flooded. If the breach width becomes larger, the inundation situation will be worse. However, as the breach width grows, the increase of the inundation area decreases.

Rivers play a role in transporting water, which prevents the land area from severe flooding to some extent. However, when the inundation volume is large enough, it can also result in inundation for some places along the river inland.

7.2 Recommendations

1. This research provides inundation maps for Shanghai under different climate and land subsidence conditions, considering sea dike breaching due to overtopping. The results give strong support for further flood risk assessment and provide a reference for flood defence system maintenance and construction.
2. The models in this research can be applied to analysis the effects of forecasted typhoon and tide when the storm and tide conditions are provided.
3. A possible further work is to consider precipitation, combining the coastal system with river and urban part to analysis the multiple disasters affect.

---

[1] The return period is based on the maximum wind speed along the trajectory included in the Shanghai area of responsibility, rather than only hitting Shanghai.

4 In this research, for the limitation of sea embankment information, several assumptions have been made. To make the results more reliable, additional efforts can be down: large-scale model experiments on sea dike breaching, stability analysis for sea dikes, etc.

5 In this research, only the neotectonic subsidence is considered, which may bring underestimation of the inundation. Anthropogenic subsidence can also be included for further work.

Bibliography

National standard of tropical cyclones grade (GB/T 19201-2006) (in Chinese), 2006.

GBT51015-2014 Chinese Guideline of Dike Design (in Chinese), 2014.

V Bjerknes. The meteorology of the temperate zone and the general atmospheric circulation. *Monthly Weather Review*, 49(1):1–3, 1921.

J Bosboom and MJF Stive. *Coastal dynamics I: lectures notes CIE4305. Version 0.5*. Delft University of Technology, 2015.

Shanghai Water Resources Bureau. *Planning of Shanghai sea embankments(1996-2010) (in Chinese)*. Shanghai Water Resources Bureau, 1996.

Shanghai Water Resources Bureau. *Planning of Shanghai sea embankments (2011-2020) (in Chinese)*. Shanghai Water Resources Bureau, 2011.

L Cavaleri and PM Rizzoli. Wind wave prediction in shallow water: Theory and applications. *Journal of Geophysical Research: Oceans*, 86(C11):10961–10973, 1981.

H Charnock. Wind stress on a water surface. *Quarterly Journal of the Royal Meteorological Society*, 81(350):639–640, 1955.

F Chen and D Qi. Investigation and analysis on the current situation of seawall protection capability in shanghai (in chinese). *Journal of Marine Sciences*, 28(1): 72–79, 2010.

G Chen, Z Wang, W Yuan, and J Chen. Calculation of wave runup under the irregular wave action. *Port and Waterway Engineering*, (2):23–30, 2010.

J Chen and J Wang. Cross-section design of widened wave dissipating platform in shanghai seawall reaching standard project, a case study of a seawall reaching standard project in fengxian district (in chinese). *Urban Roads Bridges and Flood Control*, (4):99–103, 2015.

Deltares. *Delft3D-Wave, User Manual*, 2014.

Deltares. *Wind Enhance Scheme for cyclone modelling user manual*, 2017.

Deltares. *D-Flow Flexible Mesh, User Manual*, 2018.

MW Dingemans, AC Radder, and HJ De Vriend. Computation of the driving forces of wave-induced currents. *Coastal Engineering*, 11(5-6):539–563, 1987.

X Feng, B Yin, and D Yang. The effect of wave-induced radiation stress on storm surge during typhoon saomai (2006). *Acta Oceanologica Sinica (English Version)*, 2011.

T Fujita. Pressure distribution within typhoon. *Geophys. Mag.*, 23:437–451, 1952.

H Guo, W Jiao, and Y Yang. The systematic difference and its distribution between the 1985 national height datum and the global quasigeoid (in chinese). *Acta Geodaetica et Cartographica Sinica*, (02):8–12, 2004.

GJ Holland. An analytic model of the wind and pressure profiles in hurricanes. *Monthly weather review*, 108(8):1212–1218, 1980.

GJ Holland, JI Belanger, and A Fritz. A revised model for radial profiles of hurricane winds. *Monthly Weather Review*, 138(12):4393–4401, 2010.

PA Hwang. Drag coefficient, dynamic roughness and reference wind speed. *Journal of oceanography*, 61(3):399–413, 2005.

PAEM Janssen. Quasi-linear theory of wind-wave generation applied to wave forecasting. *Journal of physical oceanography*, 21(11):1631–1642, 1991.

CP Jelesnianski. A numerical calculation of storm tides induced by a tropical storm impinging on a continental self. *Mon. Wea. Rev*, 93:343–358, 1965.

SN Jonkman, RE Jorissen, T Schweckendieck, and JP van den Bos. *CIE5314 Flood defences*. Delft University of Technology, 2017.

W Kanning, S Van Baars, PHAJM Van Gelder, and JK Vrijling. Lessons from new orleans for the design and maintenance of flood defence systems. In *Proc. ESREL*. Citeseer, 2007.

Q Ke. Flood risk analysis for metropolitan areas–a case study for shanghai. 2014.

Q Ke. Preliminary results on storm surge modelling by a numerical model – delft 3d fm. *Draft version*, 2018.

GJ Komen, K Hasselmann, and K1 Hasselmann. On the existence of a fully developed wind-sea spectrum. *Journal of physical oceanography*, 14(8):1271–1285, 1984.

Y Li, Z Qin, and Y Duan. Prediction and research of sea level rise trend in shanghai area (in chinese). *Acta Geographica Sinica*, 000(5):393, 1998.

Ministry of Natural Resources Marine early warning monitoring division. *China sea level bulletin 2018 (in Chinese)*. Marine early warning monitoring division, Ministry of Natural Resources, 2018.

VA Myers. Characteristics of united states hurricanes pertinent to levee design for lake okeechobee, florida. *Hydrometeorol.rep.u.s.weather Bur*, 1954.

E Niederleithinger, A Weller, R Lewis, U Stötzner, Th Fechner, B Lorenz, J Nießen, and GBM Wiebe. Evaluation of geophysical methods for river embankment investigation. In *Proc. 4th Int. Symp. on Flood Defence: Managing Flood Risk, Reliability and Vulnerability, Toronto, Ontario, Canada*, 2008.

Shanghai Municipal Bureau of Statistics. *Shanghai Statistical Yearbook 2018*. China Statistics Press, 2018.

RA Pielke. The hurricane. *Routledge, London*, 1990.

S Shen. Discussion on several technical problems in seawall design (in chinese). *Shanghai Water*, (1):5–7, 1997.

Ch Small and RJ Nicholls. A global analysis of human settlement in coastal zones. *Journal of coastal research*, pages 584–599, 2003.

SD Smith and EG Banke. Variation of the sea surface drag coefficient with wind speed. *Quarterly Journal of the Royal Meteorological Society*, 101(429):665–673, 1975.

H Takagi and W Wu. Maximum wind radius estimated by the 50 kt radius: improvement of storm surge forecasting over the western north pacific. *Natural Hazards and Earth System Sciences*, 16(3):705–717, 2016.

K Takahashi. Distribution of pressure and wind in a typhoon. *J. Meteor. Soc. Japan*, 17(2):417–421, 1939.

The SWAN team. *SWAN Scientific and Technical Documentation SWAN Cycle III version 41.31*, 2019.

VTT Thuy. Storm surge modelling for vietnam's coast. Master's thesis, 2003.

J van der Meer, W Allsop, T Bruce, J Rouck, An Kortenhaus, T Pullen, H Schüttrumpf, P Troch, and B Zanuttigh. *EurOtop: Manual on wave overtopping of sea defences and related sturctures - An overtopping manual largely based on European research, but for worlwide application (2nd edition)*. 01 2016.

PJ Visser. *Breach growth in sand-dikes*. PhD thesis, Delf University of Technology, 1998.

J Wang, S Xu, M Ye, and J Huang. The mike model application to overtopping risk assessment of seawalls and levees in shanghai. *International Journal of Disaster Risk Science*, 2(4):32–42, 2011.

J Wang, W Gao, S Xu, and L Yu. Evaluation of the combined risk of sea level rise, land subsidence, and storm surges on the coastal areas of shanghai, china. *Climatic Change*, 115(3-4):p.537–558, 2012.

L Wang. Simulation of compound coastal flooding in shanghai (in chinese). Master's thesis, Shanghai Normal University, 2019.

E Wu. Problems and countermeasures of water conservancy elevation system in jiangsu province (in chinese). *Journal of Changzhou Institute of Technology*, pages 252–256, 2008.

Y Xu. *Chinese meteorological disaster in Shanghai (in Chinese)*. 2006.

Y. Yamanaka, R. Shibata, Y. Tajima, and N. Okami. Inundation characteristics in arida city due to overtopping waves induced by 2018 typhoon jebi. In Nguyen Trung Viet, Dou Xiping, and Tran Thanh Tung, editors, *APAC 2019*, pages 199–206, Singapore, 2020. Springer Singapore. ISBN 978-981-15-0291-0.

J Yin, Zh Yin, X Hu, Sh Xu, J Wang, Zh Li, H Zhong, and F Gan. Multiple scenario analyses forecasting the confounding impacts of sea level rise and tides from storm induced coastal flooding in the city of shanghai, china. *Environmental earth sciences*, 63(2):407–414, 2011.

D Yu, J Yin, and M Liu. Validating city-scale surface water flood modelling using crowd-sourced data. *Environmental Research Letters*, 11(12):124011, 2016.

C Zhang, F Zhu, L. I. Wei-Tao, and Z Liu. Current status of seawalls in shanghai,zhejiang and fujian in china (in chinese). *Advances in Science and Technology of Water Resources*, 2008.

Q Zhang, S Chen, Y Kuo, K Lau, and RA Anthes. Numerical study of a typhoon with a large eye: Model simulation and verification. *Monthly weather review*, 133(4): 725–742, 2005.

R Zhang, G Chen, J Hu, Z Guo, J Tan, and Q Liu. Experimental analysis of mechanism of seawall breach and threshold of seawall breach (in chinese). *Coastal engineering*, 36(3):10–21, 2017.

Y Zhang, L Pan, and Y Wang. Discussion on the cause of slope collapse in shanghai area (in chinese). *Urban Construction Theory Research*, 266(20):140–141, 2018.

Z Zhou and W Liu. Some characteristics of the typhoon disaster in zhejiang province. *Geog Res*, 14(2):56–63, 1995.

Y Zhu, PJ Visser, and JK Vrijling. A model for breach erosion in clay-dikes. In *Coastal Dynamics 2005: Proc., 5th Int. Conf*. ASCE, Reston, VA, 2006.

M Zijlema, G Ph Van Vledder, and LH Holthuijsen. Bottom friction and wind drag for wave models. *Coastal Engineering*, 65:19–26, 2012.

Y Zong and X Chen. Typhoon hazards in the shanghai area. *Disasters*, 23(1):66–80, 1999.

List of Figures

List of Tables

Field Work in Shanghai

A

The fieldwork in Shanghai was undertaken from 5 September to 28 September in 2019. This investigation involves urban, river and coastal embankments in Shanghai. In this chapter, only the coastal part is mentioned. The coastal part includes embankment types and conditions on different district along the coast. The elevation of the crest and wall were measured at the same time. All the elevation measures in this investigation are based on an RTK equipment with Wusong datum, which uses the low water level measured from 1871 to 1900 by Shanghai Wusongkou tidal station as the reference level.

This investigation focuses on sea embankments on the mainland. For easy understanding, the sea embankment is divided into six parts as in Fig. 2.1: Baoshan, Pudong New District A, Pudong New District B (former Nanhui), Pudong New District C (former Nanhui, north part of Hangzhou), Fengxian and Jinshan.

A.0.1 Baoshan part

Baoshan district locates on the north of Shanghai, which is the connection between Yangtze River and Huangpu River. It also adjoins Yangpu, Hongkou, Jingan, Putuo and Jiading District. As a result, Baoshan District plays a vital role in transportation. For convenient transportation, Baoshan district attracts investments from ports and industries. The famous Baosteel Group has factories in Baoshan district as well.

Since there are many industries in Baoshan, it is hard to make a successive investigation along the coastline. Investigation in this district is based on several points that can be approached. These points are concentrated on specific places, which can be generally classified as the northern part, middle part and southern part of Baoshan.

Northern part in Baoshan

The most north sea embankments within Shanghai area are occupied by two reservoirs. Since the reservoirs are for drinking water or other special use, it is not allowed to go inside. However, photos can be taken outside the fences, and the offshore embankment elevation can be estimated by the extending sea wall outside the fences. Fig. A.1 shows the embankment situation and location.

(a) Location A, Baosteel reservoir

(b) Location B, Chenhang reservoir

(c) Location of A and B on the map

Fig. A.1.: Reservoirs in Northern part of Baoshan

Middle part in Baoshan

To the south-east of these reservoirs, there are some wharves and factories along the sea embankment. These ‘wharf-embankment-factory’ occupy the coastline for about 6 km. Fig. A.2 shows a part of sea embankment near Sujian Wharf. The crest elevation is around 8 m over here. The revetment is covered with fence board. The width of the sea wall on the top is 35 cm, and this width is about the same along the wharf part.

Fig. A.2.: Sea embankment near Sujian Wharft

Southern part in Baoshan

The boundary between Baoshan and Pudong new area is at Wusongkou, which is the mouth of the Huangpu River. The only investigation point at the southern part is near Wusongkou international cruise terminal. Due to the protection by the breakwaters of the terminal on the north-east, the crest elevation of the sea embankment here is less than 7 m. The buildings and grasses behind the embankment even have a higher elevation than the road. The width of the sea wall on the top is around 30 cm. The outer slope is under maintenance.

A.0.2 Pudong New District

Pudong new district is one of the largest districts in Shanghai, and it has the most population. Located on the south-east of Shanghai, Pudong new district is separated from Xuhui, Huangpu, Hongkou, Yangpu and Baoshan district by the Huangpu River on the west and is adjacent to Fengxian and Minhang district on the south. On the north-west, Changxing Island and Hengsha Island shadow this district. This district will be divided into three parts.

Pudong new district A

Pudong new district A is the former Pudong new district. The sea embankments start from Wusongkou on the north and end at Pudong airport on the south. Shanghai Waigaoqiao Free Trade Zone and Pudong airport are located in this area.

It is hard to get close to the airport area on the southern part of Pudong new district A. See Fig. A.3 .

Fig. A.3.: Investigation points in Pudong new district A

As shown in Fig. A.4, the revetment of the embankment is covered with fence board. The buildings of the companies are pretty close to the road and of course the sea wall. The width of the sea wall on the top is about 50 cm here. The width, however, varies from 30 cm to 120 cm along the embankment in Pudong new district A. Due to the limited investigation places, the sudden-change points are hard to be observed.

Fig. A.4.: Embankment near point C

For the sea embankments, the crest elevation is about 8.2 m according to the measures from Wusongkou to Shanghai Yangtze river tunnel. However, the crest elevation near Shanghai Yangtze river tunnel has a significant decrease. The elevation here is only about 6.5 m, maybe as a result of land subsidence by the tunnel.

Pudong new district B

Pudong new district B is part of the former Nanhui district. The sea embankments start from the south of Pudong international airport and end around Dishui Lake. Green points in Fig. A.5 represent the investigation places on the south of Pudong international airport. It is also shown that on the seaside of the investigation places, there is a new reclaimland. The land is surrounded by the embankments on both seaward and landward. And grasses are covered inside the land (see Fig. A.6a). It is hard to get an approach to the seaward side, so only the landward side is investigated.

The crest elevation in this area is around 7.7 m, and the sea wall elevation is about 1.2m higher. The width of the sea wall on the top is 60 cm, and it is the same for the sea wall in this part. Concrete units are placed next to the sea wall (see Fig. A.6b).

Fig. A.5.: Investigation places on the south of the airport

On the inner slope of the embankment, there are some grasses and trees covered (see Fig. A.6c). Most of them are luxuriant, and only a few of them are getting yellow.

Green points in Fig. A.7 represent the investigation places from Dazhi River to Dishui Lake. Reclaimed land, or more accurate the dike protection project, is also observed in this part. The land is also covered with grasses.

The crest elevation in this area is around 8 m, which is a little bit higher than the north part. The sea wall elevation is about 1.4 m higher. The width of the sea wall on the top is 30 cm, and it is the same for the sea wall in this part. The outer slope of the embankment is covered with fence board. Trashes can be recognized under the board (see Fig. A.8a). Grasses covered on the inner slope are also luxuriant along the way (see Fig. A.8b).

Pudong new district C

Pudong new district C is part of the former Nanhui district, and it is mainly along the Hangzhou Bay.

(a) Grasses inside the reclaimed land

(b) Concrete units and the cross section of the sea wall

(c) Grass covered on the inner slope

Fig. A.6.: Pictures for the embankments on the south of the airport

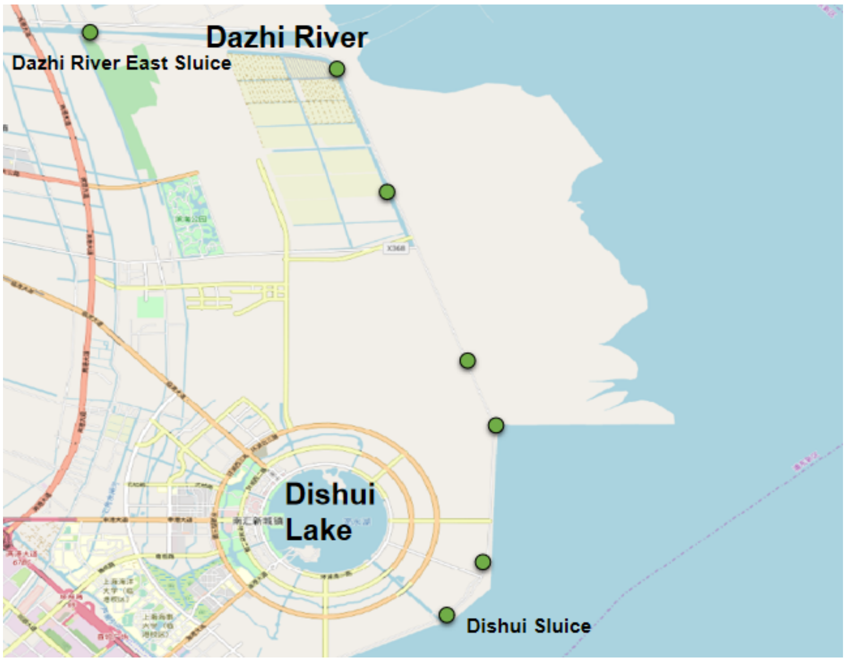

Fig. A.7.: Investigation places on the south of the airport

Green points in Fig. A.9 represent the investigation places in Pudong new district C. Fortunately, the investigation went on continuously along the embankment in this part, so the measurement took place every 2 km.

The crest elevation in this area is around 8.5 m, which is higher than other parts in Pudong new district. The sea wall elevation is about 1.1 m higher than the crest. The width of the sea wall on the top varies from 30 cm to 120 cm.

Above the berm, the outer slope of the embankment is covered with fence board. The slope under the berm is covered with concrete units. These concrete units are placed in order. Fig. A.10a shows the sea wall structure at location A in Fig. A.9. It is noticeable that the concrete units armour ends suddenly on the west, which is probably the edge of Fengxian District. Grasses covered on the inner slope are more or less luxuriant along the way. (See Fig. A.10b). Shown in Fig. A.10c, a sudden change of seawall height is observed at location B in Fig. A.9. The height difference is 80 cm according to measurement.

(a) Typical sea wall structure

(b) Grass covered on the inner slope

Fig. A.8.: Pictures for the embankments from Dazhi River to Dishui Lake

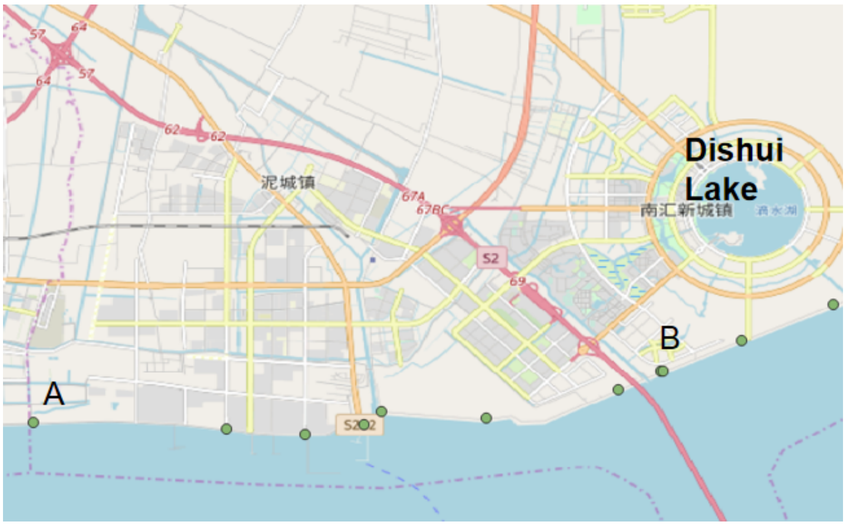

Fig. A.9.: Investigation places in Pudong new district C

A.0.3 Fengxian District

Fengxian district locates in the south of Shanghai, bordering Pudong new district in the east, Jinshan district and Songjiang district in the west, Hangzhou Bay in the south. Huangpu river separates Minhang district from Fengxian in the north.

Green points in Fig. A.11 represent the investigation places in Fengxian district. The sea embankment from Fengxian to Pudong new district C can be investigated continuously. The measurement took place almost every 2 km.

The crest elevation in this area is around 8 m, while the sea wall elevation is about 9 m. The width of the sea wall on the top is 60 cm in this district.

Generally, there are three kinds of outer slope structure in Fengxian. For the first type shown in Fig. A.12a, there is a wide berm at the outer part of the embankment. Above the berm, the outer slope of the embankment is covered with fence board. The slope under the berm is covered with concrete units. These concrete units are placed in order. This kind of structure can be found on the east half of Fengxian. For the second type shown in Fig. A.12b, there is no concrete units here. Instead, the revetment is connected to a large area of grassland. This kind of structure can be found in the middle by the west. The last type of structure locates on the west part of Fengxian (see Fig. A.12c). Nut blocks rather than fence board are used on the slope. At the toe of the nut blocks, there is a ditch separate the plants apart from the embankment.

(a) Sea wall structure at Location A

(b) Grass covered on the inner slope

(c) Sudden change of seawall height

Fig. A.10.: Pictures for the embankments in Pudong new district C

Fig. A.11.: Investigation places in Fengxian district

Grasses covered on the inner slope are more or less luxuriant (See Fig. A.13a). However, as shown in Fig. A.13b, the grasses have gotten yellow at location A in Fig. A.11.

A.0.4 Jinshan District

Jinshan district locates on the southwest of Shanghai. It borders Fengxian district in the east, Songjiang district and Qingpu district in the north, Pinghu Lake and Jiashan in the west.

Green points in Fig. A.14 represent the investigation places in Fengxian district. For the companies and industries along the embankment, only several points in Jinshan district were under investigation.

The crest elevation in this area is around 9.1 m, while the sea wall elevation is about 10 m. The elevation is the highest among all the involved districts. The width of the sea wall on the top is 60 cm.

A typical outer slope structure is shown in Fig. A.15. There is a berm at the outer part of the embankment. Above the berm, the outer slope of the embankment is covered with fence board. The slope under the berm is covered with concrete units. These concrete units are almost placed in order. On the seaward side of the concrete

(a) First type of outer slope structure

(b) Second type of outer slope structure

(c) Third type of outer slope structure

Fig. A.12.: Outer slope structure in Fengxian

(a) The grassed slope are usually luxuriant

(b) Yellow grasses on the slope at location A

Fig. A.13.: Grass cover on the inner slope in Fengxian district

Fig. A.14.: Investigation places in Jinshan district

units is grassland, which is also ended up with concrete units in a random placing method.

Grasses covered on the inner slope are usually luxuriant as shown in Fig. A.16.

Fig. A.15.: Typical outer slope structure

A.0.5 Conclusions of the field work

During this fieldwork, 168 points have been investigated and measured along the flood defence system in Shanghai. This investigation fully shows the complexity of

Fig. A.16.: Grass cover on the inner slope

the flood defence system. Since the embankments have been served for a long time, small problems like erosion on the wall may happen. In this case, annual repairs take place carefully by involved agencies. Projects with higher standard are undertaken for the following years. However, as frequent typhoon attack threatens the safety of sea embankment, it is still meaningful to research extreme situations.

Other information

B

B.1 Storm naming

In China, the typhoons are numbered following in the order of their occurrence. According to China Meteorological Administration (`http://www.cma.gov.cn`), the tropical cyclone can have a number if the following criteria are met: 1) it occurs in the west of 180 degrees longitude, north of the equator on Pacific northwest and south China sea; 2) the maximum mean wind speed in the vicinity of the centres is up to category 8 in Beaufort scale or higher. The number has four digits. The first two indicate the last two digits of the year and the last two indicate the order of occurrence in that year. For example, the sixth tropical cyclone to meet the numbering criteria in 2001 should be listed as ’0106’.

Typhoon is named following Northwest Pacific and South China Sea tropical cyclone naming system in China from Jan 1st 2000. The system is established in order to achieve convenient communication among different countries by the Typhoon Committee (`http://www.typhooncommittee.org`). The committee members come from 14 countries and districts, including Cambodia, China, North Korea, Hong Kong, Japan, Laos, Macao, Malaysia, the Philippines, South Korea, Singapore, Thailand, the United States and Vietnam. Each member contributes 10 tropical cyclone names, and the naming list containing 140 names are in order and used in cycles. Tropical cyclone names are named in a predetermined order. Tropical cyclones have maintained their name throughout life. When a typhoon becomes a publicly known typhoon after it has caused a particularly significant disaster or loss of life, the name will be removed from the current list and replaced with a new name in order to prevent it from sharing the same name with other typhoons.

B.2 Other figures and tables

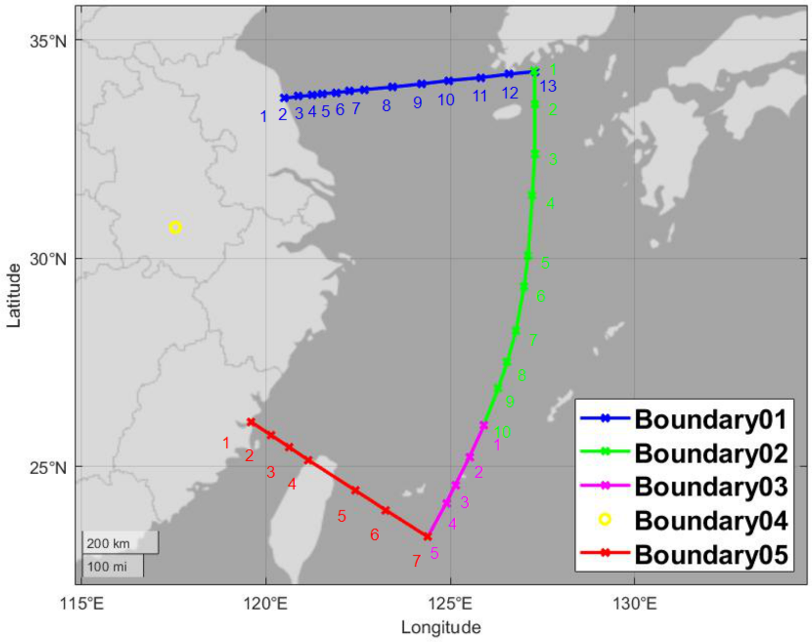

Fig. B.1.: Locations of points on the boundaries

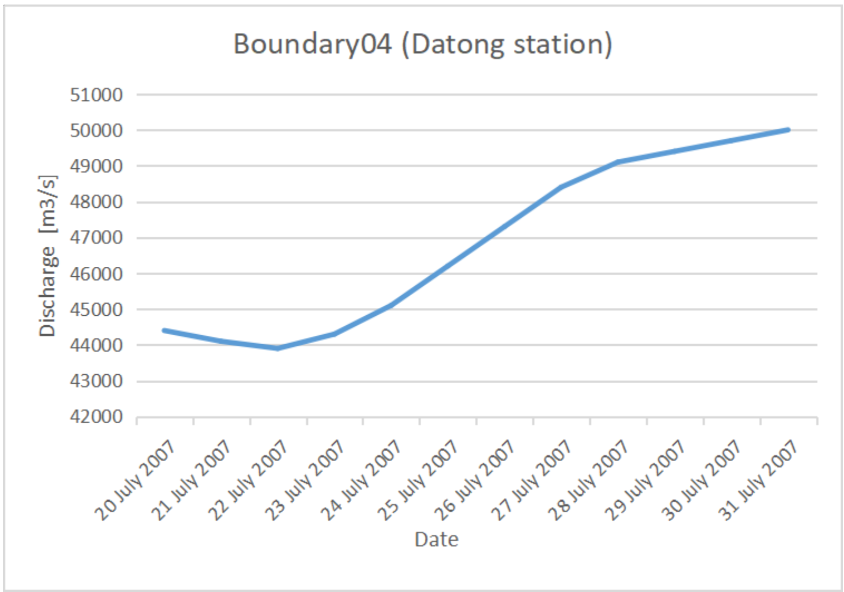

Fig. B.2.: Discharge series at Boundary04 (Datong Station) used for tide level validation in 2007

Tab. B.1.: Names and locations of points on the boundaries

Name	Lon [deg]	Lat [deg]
Boundary01_0001	120.49	33.69
Boundary01_0002	120.88	33.73
Boundary01_0003	121.25	33.76
Boundary01_0004	121.53	33.79
Boundary01_0005	121.90	33.82
Boundary01_0006	122.27	33.85
Boundary01_0007	122.66	33.88
Boundary01_0008	123.45	33.94
Boundary01_0009	124.22	34.01
Boundary01_0010	124.96	34.09
Boundary01_0011	125.82	34.15
Boundary01_0012	126.59	34.23
Boundary01_0013	127.31	34.29
Boundary02_0001	127.29	34.31
Boundary02_0002	127.29	33.57
Boundary02_0003	127.29	32.43
Boundary02_0004	127.23	31.47
Boundary02_0005	127.11	30.07
Boundary02_0006	127.00	29.34
Boundary02_0007	126.78	28.28
Boundary02_0008	126.55	27.54
Boundary02_0009	126.30	26.90
Boundary02_0010	125.91	26.02
Boundary03_0001	125.92	26.01
Boundary03_0002	125.52	25.23
Boundary03_0003	125.14	24.54
Boundary03_0004	124.89	24.09
Boundary03_0005	124.39	23.26
Boundary04	117.55	30.73
Boundary05_0001	119.60	26.09
Boundary05_0002	120.15	25.76
Boundary05_0003	120.62	25.48
Boundary05_0004	121.15	25.16
Boundary05_0005	122.42	24.41
Boundary05_0006	123.26	23.92
Boundary05_0007	124.38	23.26

Tab. B.2.: Semidiurnal tidal constituents for the points on the open boundaries (A:amplitude, P:phase)

Name	M2		S2		N2		K2	
	A [m]	P [deg]	A [m]	P [deg]	A [m]	P [deg]	A [m]	P [deg]
Boundary01_0001	0	0	0	0	0	0	0	0
Boundary01_0002	1.0061	66.63	0.3683	132.97	0.0659	56.15	0.0442	124.57
Boundary01_0003	0.9445	85.02	0.3512	141.93	0.0834	69.32	0.0533	129.84
Boundary01_0004	0.9029	93.22	0.347	140.56	0.1077	74.96	0.0654	127.22
Boundary01_0005	0.85	101.79	0.3319	140.24	0.1286	78.22	0.0744	124.1
Boundary01_0006	0.7298	100.5	0.2998	133.21	0.1365	77.43	0.0755	116.73
Boundary01_0007	0.6969	106.53	0.2795	138.43	0.1393	84.71	0.0732	121.71
Boundary01_0008	0.6926	116.18	0.2572	147.64	0.1414	96.84	0.0675	134.23
Boundary01_0009	0.7182	117.48	0.252	146.59	0.1477	99.75	0.0658	139.37
Boundary01_0010	0.7724	113.36	0.2676	140.7	0.1623	94.99	0.0703	136.11
Boundary01_0011	0.8861	91.83	0.3309	118.9	0.198	75.49	0.0884	113.29
Boundary01_0012	0.9462	54.77	0.3886	80.99	0.2105	43.62	0.1034	73.77
Boundary01_0013	0.9797	17.59	0.4247	44.58	0.2006	10.04	0.1129	35.77
Boundary02_0001	0.9885	18.71	0.4284	45.77	0.2024	11.09	0.1137	36.96
Boundary02_0002	0.753	14.66	0.3336	38.98	0.1593	9.43	0.0903	30.65
Boundary02_0003	0.6398	358.16	0.2919	23	0.1333	355.12	0.082	14.74
Boundary02_0004	0.5989	342.84	0.2703	9.67	0.1181	340.11	0.0783	1.63
Boundary02_0005	0.5887	323.94	0.2529	352.65	0.1126	320.42	0.0766	345.2
Boundary02_0006	0.5872	315.62	0.2458	343.14	0.1111	311.47	0.0755	336.78
Boundary02_0007	0.5687	309.39	0.236	334.24	0.1069	303.16	0.0722	329.67
Boundary02_0008	0.5588	307.99	0.2331	331.87	0.1061	300.45	0.0706	327.94
Boundary02_0009	0.5478	306.91	0.2294	330.47	0.1053	298.66	0.069	326.86
Boundary02_0010	0.5214	305.69	0.2202	328.94	0.1025	296.94	0.0658	325.69
Boundary03_0001	0.5212	305.65	0.2201	328.91	0.1025	296.91	0.0658	325.66
Boundary03_0002	0.4944	305.19	0.2108	327.74	0.099	295.89	0.0627	324.9
Boundary03_0003	0.5222	296.07	0.2185	318.83	0.1003	286.4	0.0631	316.17
Boundary03_0004	0.5155	295.66	0.2156	318.15	0.0985	285.73	0.0619	315.63
Boundary03_0005	0.5062	295.58	0.2111	317.71	0.0959	285.22	0.0603	315.32
Boundary05_0001	0	0	0	0	0	0	0	0
Boundary05_0002	1.9111	69.86	0.5641	101.63	0.3467	48.06	0.1476	100.67
Boundary05_0003	1.5615	72.17	0.4489	103.68	0.2968	51.3	0.1255	101.98
Boundary05_0004	1.2081	77.95	0.3262	110.16	0.238	58.66	0.0986	107.93
Boundary05_0005	0.429	300.43	0.1865	322.98	0.0867	292.79	0.054	321.17
Boundary05_0006	0.4821	298.1	0.2022	320.24	0.0929	288.66	0.0581	318.07

Tab. B.3.: Diurnal tidal constituents for the points on the open boundaries (A:amplitude, P:phase)

Name	K1		O1		P1		Q1	
	A [m]	P [deg]	A [m]	P [deg]	A [m]	P [deg]	A [m]	P [deg]
Boundary01_0001	0	0	0	0	0	0	0	0
Boundary01_0002	0.1922	295.93	0.1486	236.67	0.037	313.48	0.0208	200.91
Boundary01_0003	0.1688	302.16	0.1318	239.24	0.0336	313.39	0.0199	199.52
Boundary01_0004	0.1451	304.28	0.1132	236.9	0.0302	308.47	0.0188	192.8
Boundary01_0005	0.116	310.42	0.089	235.28	0.0251	304.76	0.017	185.53
Boundary01_0006	0.0855	314.86	0.064	228.13	0.019	295.93	0.0152	173.19
Boundary01_0007	0.0528	340.1	0.0347	217.5	0.0091	301.4	0.0125	161.45
Boundary01_0008	0.0579	76.93	0.0359	106.99	0.0131	103.24	0.0107	117.73
Boundary01_0009	0.1192	103.24	0.0892	92.17	0.0353	107.96	0.0175	83.34
Boundary01_0010	0.1808	106.99	0.1389	86.94	0.0569	105.3	0.0274	70.33
Boundary01_0011	0.2539	97.22	0.1929	74.26	0.0806	93.9	0.0391	57.34
Boundary01_0012	0.2626	81.04	0.1934	58.24	0.0821	78.46	0.0393	43.91
Boundary01_0013	0.2279	65.51	0.1632	43.97	0.0697	63.85	0.0324	32.26
Boundary02_0001	0.2292	65.93	0.1642	44.31	0.0701	64.26	0.0326	32.61
Boundary02_0002	0.2232	74.78	0.1628	54.55	0.0707	73.07	0.0347	41.3
Boundary02_0003	0.2315	77.45	0.1725	58.06	0.0743	75.37	0.038	44.1
Boundary02_0004	0.227	76.76	0.1714	57.45	0.0736	74.58	0.0382	44.43
Boundary02_0005	0.2212	77.36	0.1682	58.21	0.0721	74.51	0.0375	45.86
Boundary02_0006	0.22	78	0.1687	59.1	0.0715	75.27	0.0371	46.65
Boundary02_0007	0.2142	80.28	0.1674	61.1	0.0692	77.56	0.0356	49.06
Boundary02_0008	0.2101	81.97	0.1664	62.78	0.0675	79.14	0.0346	50.45
Boundary02_0009	0.2069	83.65	0.1659	64.76	0.0662	80.78	0.0339	51.96
Boundary02_0010	0.2012	86.07	0.1636	68.11	0.0638	83.13	0.0326	53.85
Boundary03_0001	0.2011	86.07	0.1635	68.12	0.0638	83.12	0.0326	53.84
Boundary03_0002	0.197	88.35	0.1631	70.83	0.0623	85.52	0.0315	56.14
Boundary03_0003	0.1867	88.8	0.1583	71.2	0.0604	86.55	0.031	58.19
Boundary03_0004	0.1838	90.12	0.1552	72.06	0.0591	87.72	0.0302	59.44
Boundary03_0005	0.1759	92.06	0.1489	73.7	0.0567	89.41	0.0293	61.57
Boundary05_0001	0	0	0	0	0	0	0	0
Boundary05_0002	0.285	122.17	0.2379	92.63	0.0876	122.32	0.0466	72.24
Boundary05_0003	0.2515	124.48	0.214	95.22	0.0803	124.53	0.043	76.38
Boundary05_0004	0.2143	126.21	0.1856	98.56	0.0697	127.89	0.0381	81.29
Boundary05_0005	0.1816	98.38	0.154	78.22	0.0578	94.45	0.031	63.51
Boundary05_0006	0.1781	95.68	0.1523	76.49	0.0572	92.46	0.0302	63.19

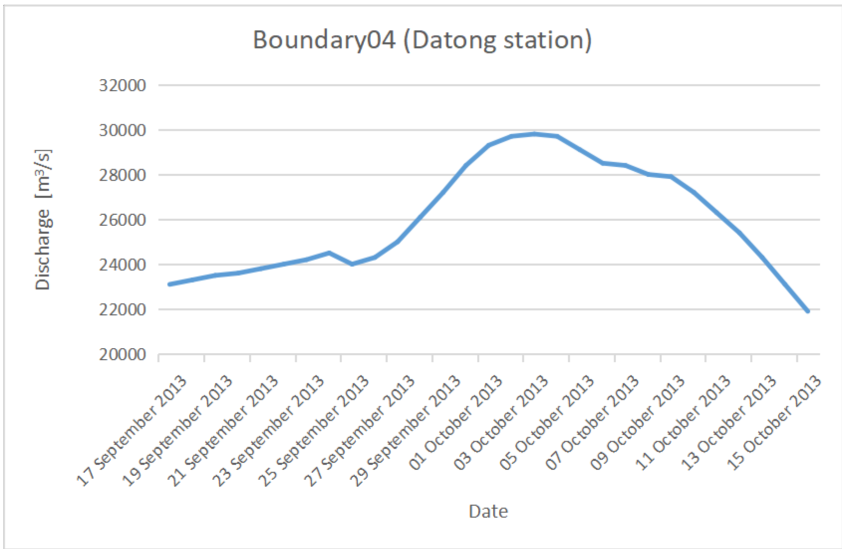

Fig. B.3.: Discharge series at Boundary04 (Datong Station) used for tide level validation in 2013

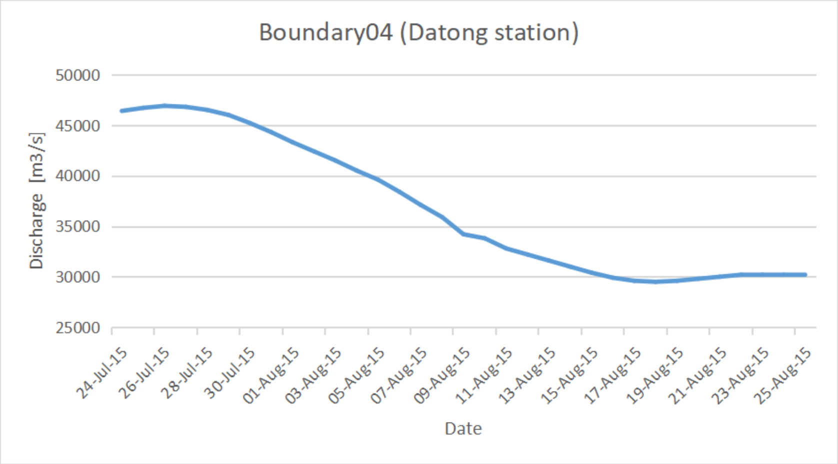

Fig. B.4.: Discharge series at Boundary04 (Datong Station) used for tide level validation in 2015

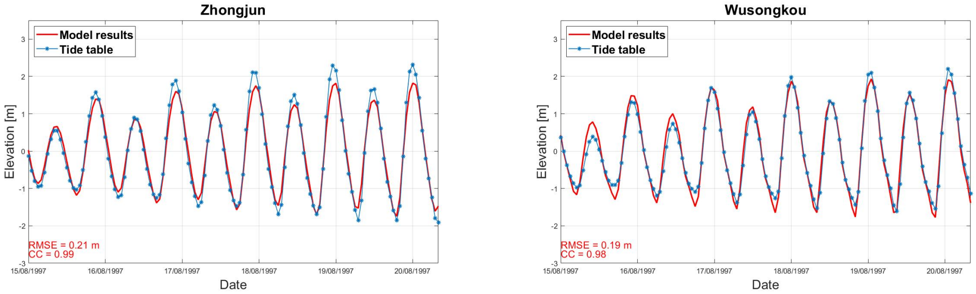

(a) Zhongjun **(b)** Wusongkou

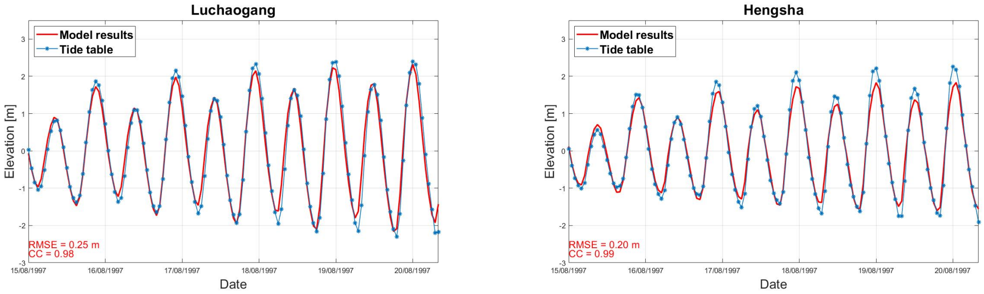

(c) Luchaogang **(d)** Hengsha

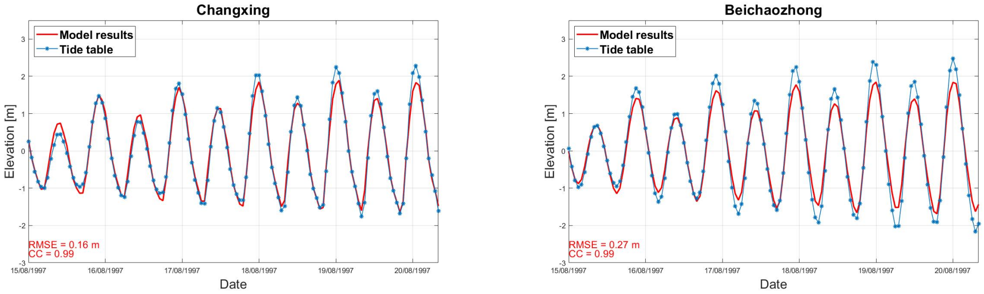

(e) Changxing **(f)** Beichaozhong

Fig. B.5.: Tide level in 1997 without changing the bathymetry

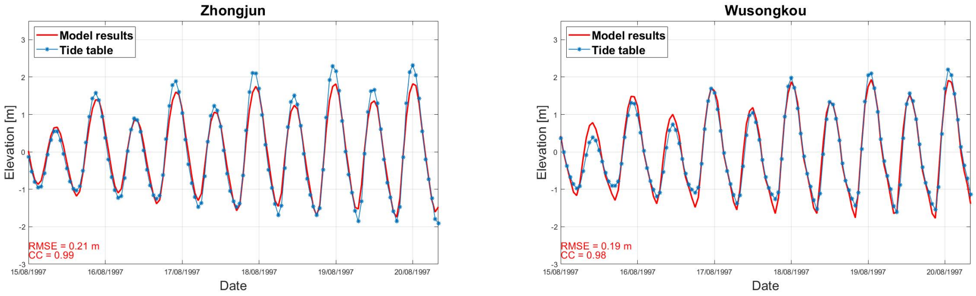

(a) Zhongjun **(b)** Wusongkou

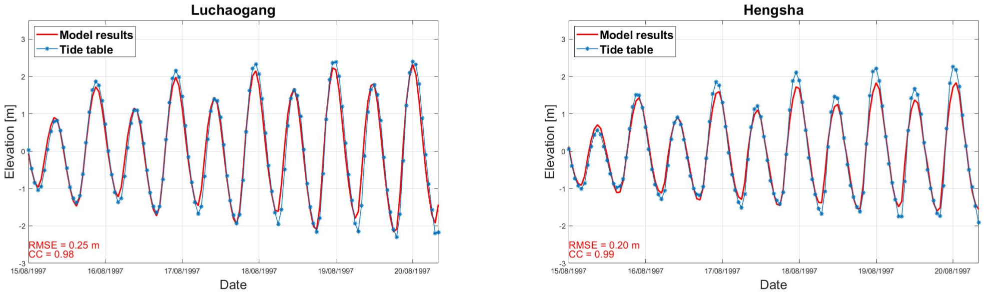

(c) Luchaogang **(d)** Hengsha

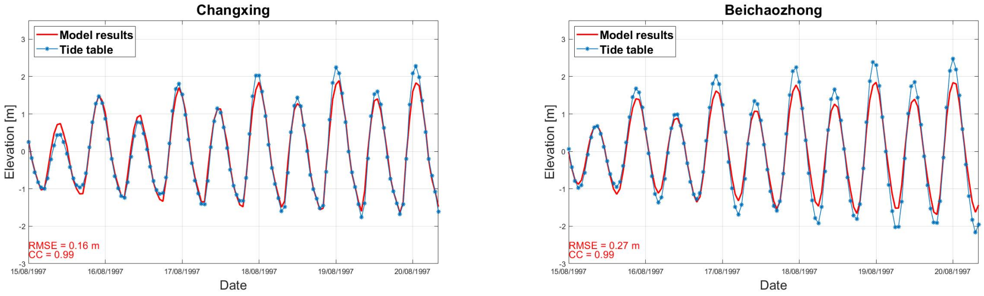

(e) Changxing **(f)** Beichaozhong

Fig. B.6.: Tide level in 1997 when deducted 2m of the local bathymetry

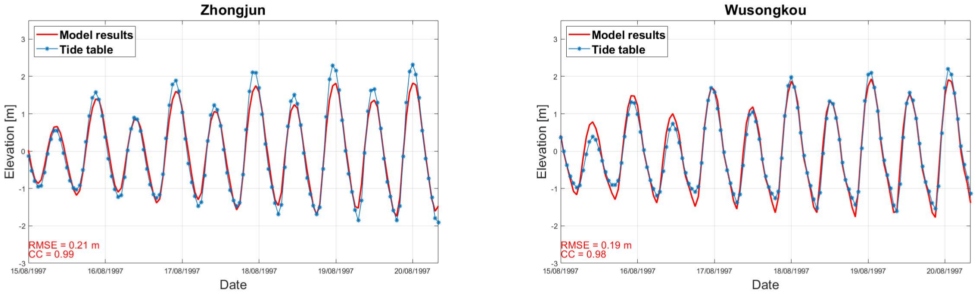

(a) Zhongjun **(b)** Wusongkou

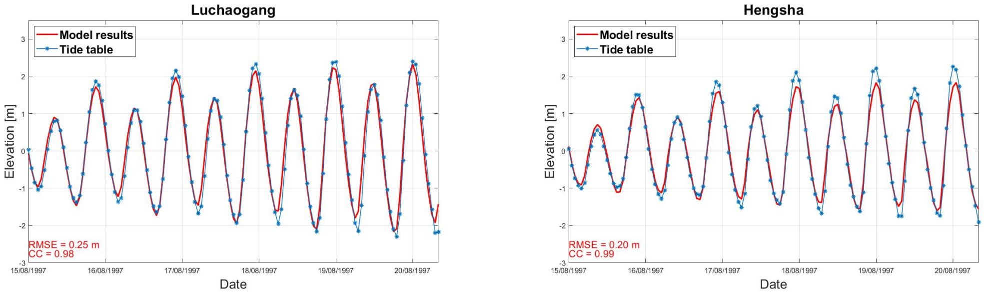

(c) Luchaogang **(d)** Hengsha

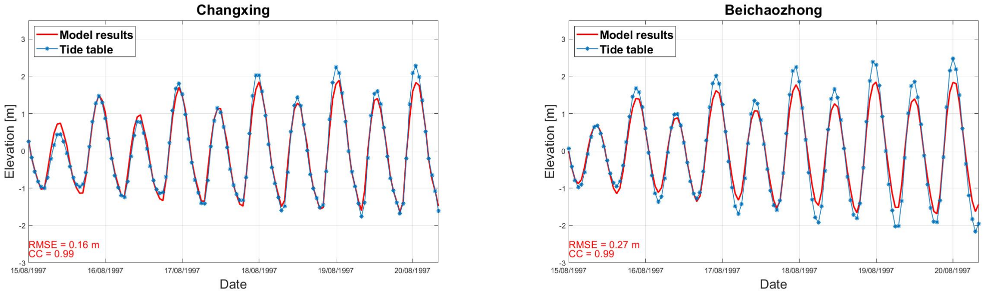

(e) Changxing **(f)** Beichaozhong

Fig. B.7.: Tide level in 1997 when deducted 3m of the local bathymetry

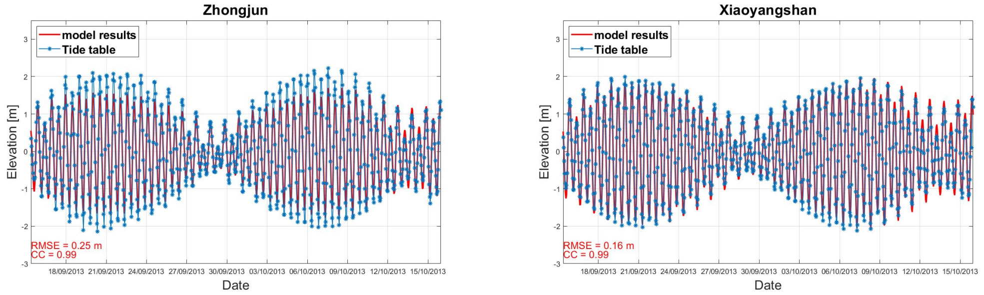

(a) Zhongjun **(b)** Xiaoyangshan

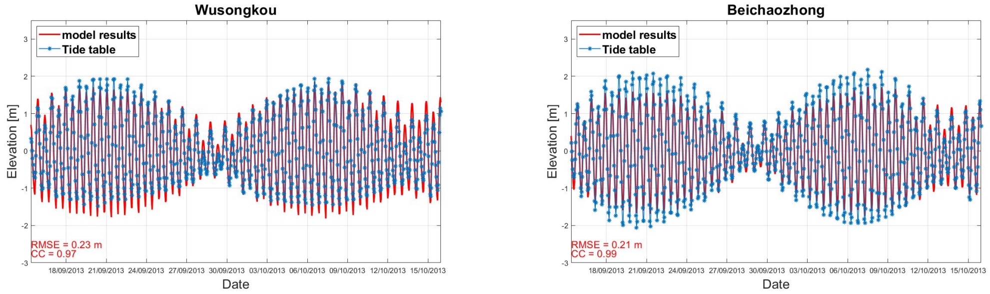

(c) Wusongkou **(d)** Beichaozhong

Fig. B.8.: Tide level validation in 2013

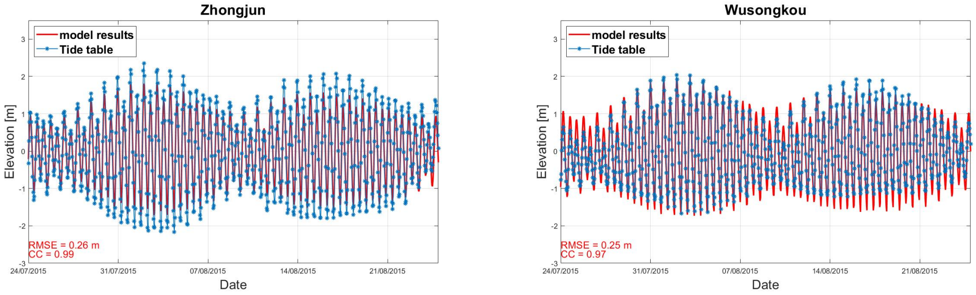

(a) Zhongjun **(b)** Wusongkou

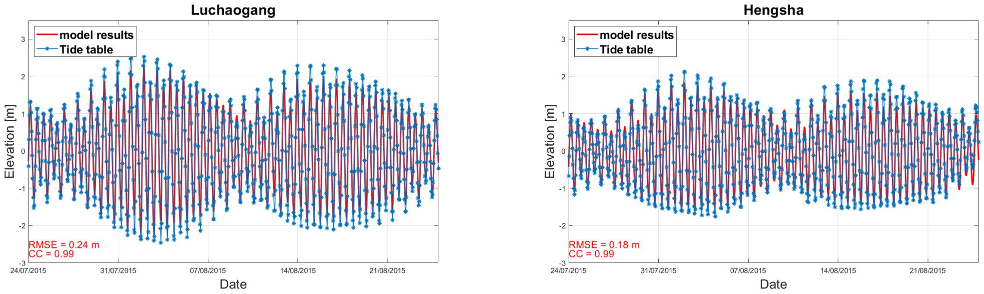

(c) Luchaogang **(d)** Hengsha

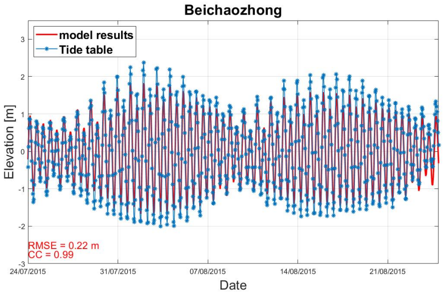

(e) Beichaozhong

Fig. B.9.: Tide level validation in 2015

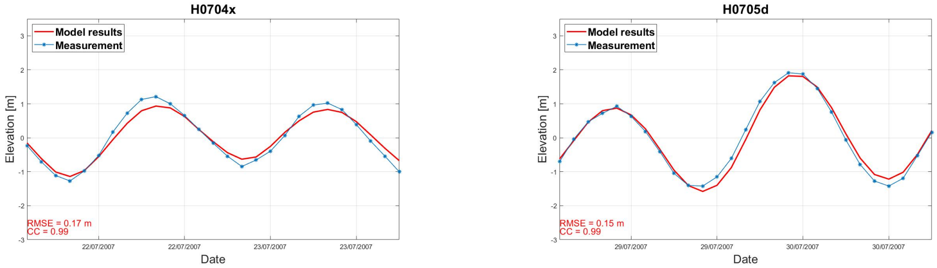

(a) H0704x **(b)** H0705d

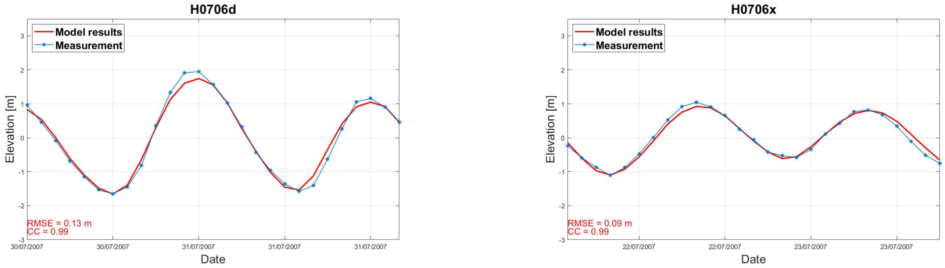

(c) H0706d **(d)** H0706x

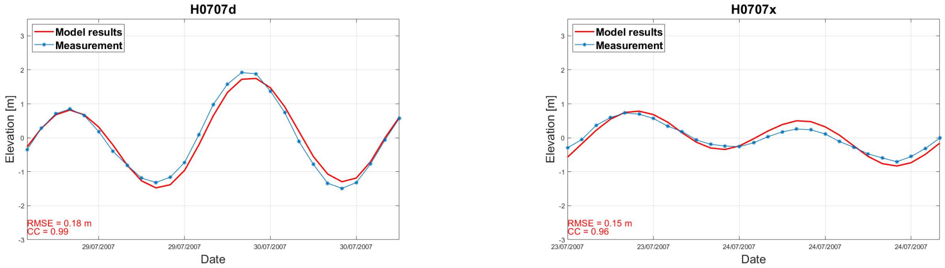

(e) H0707d **(f)** H0707x

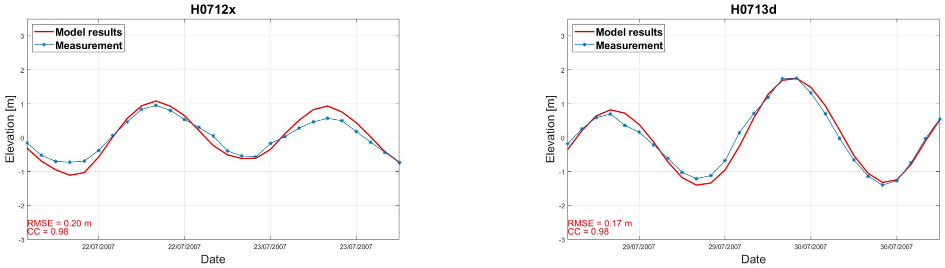

(g) H0712x **(h)** H0713d

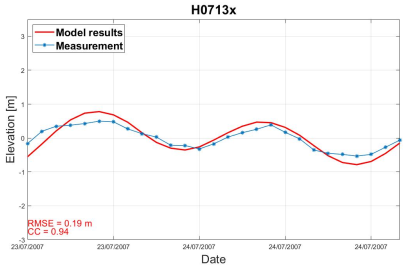

(i) H0713x

Fig. B.10.: Tide level validation in 2007

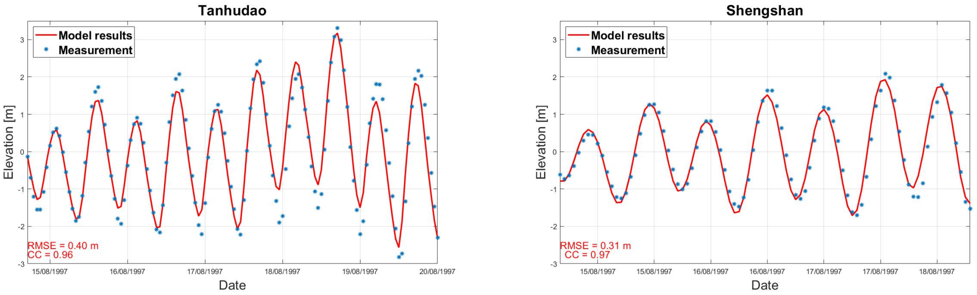

(a) Tanhudao **(b)** Shengshan

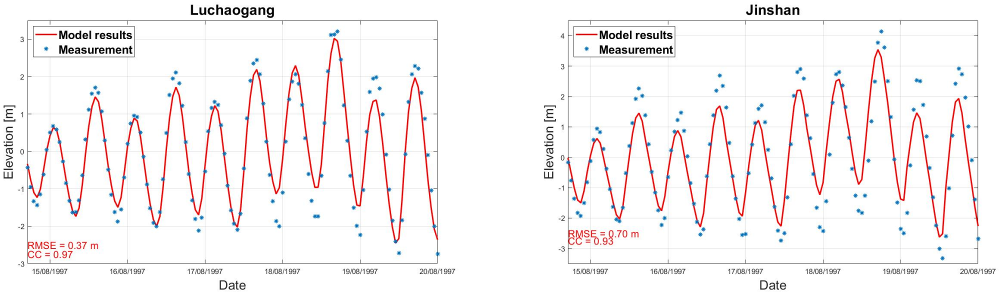

(c) Luchaogang **(d)** Jinshan

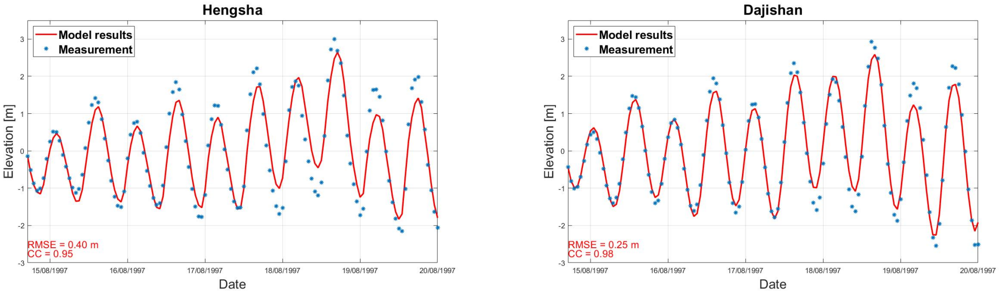

(e) Hengsha **(f)** Dajishan

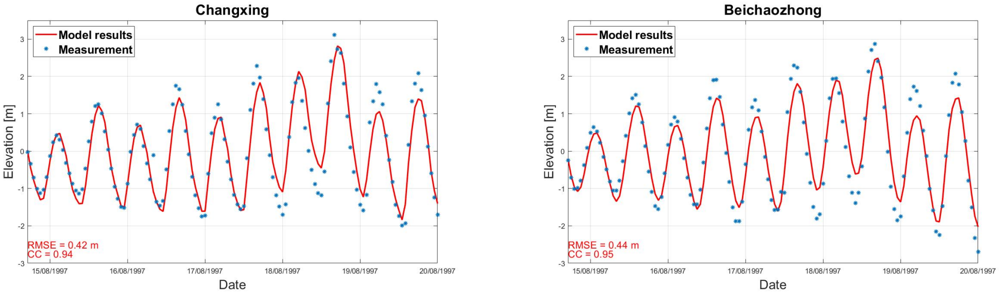

(g) Changxing **(h)** Beichaozhong

Fig. B.11.: 1997 Total level validation (part 1)

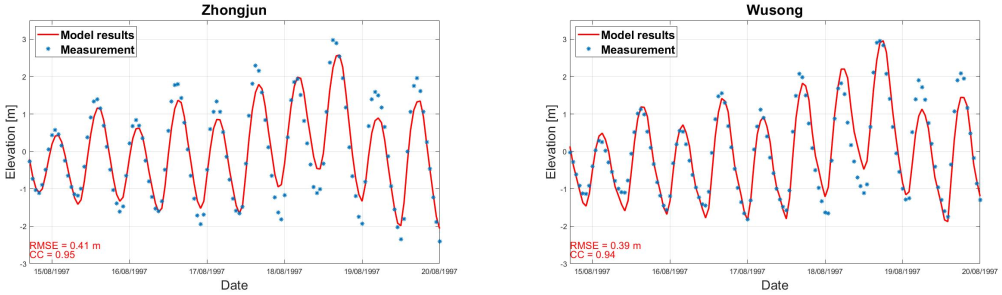

(a) Zhongjun **(b)** Wusongkou

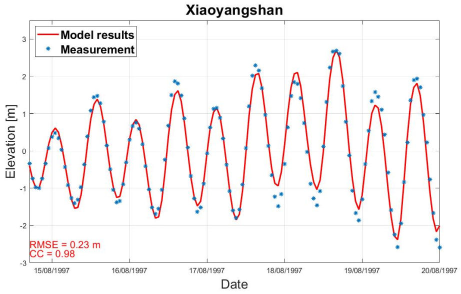

(c) Xiaoyangshan

Fig. B.12.: Total level validation in 1997 (part 2)

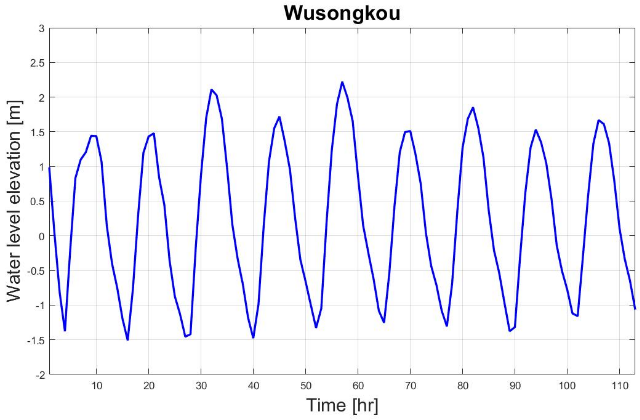

(a) R7.9

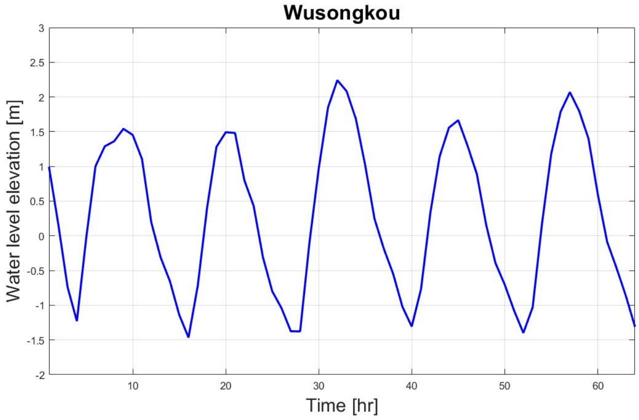

(b) R3.4

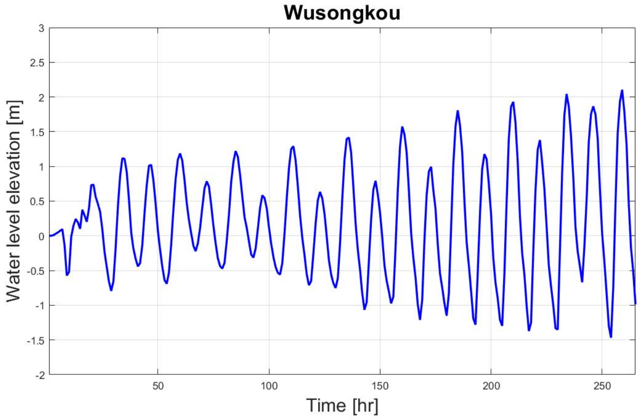

(c) R2.9

Fig. B.13.: Water level at Wusongkou during historical hypothetical events (part 1)

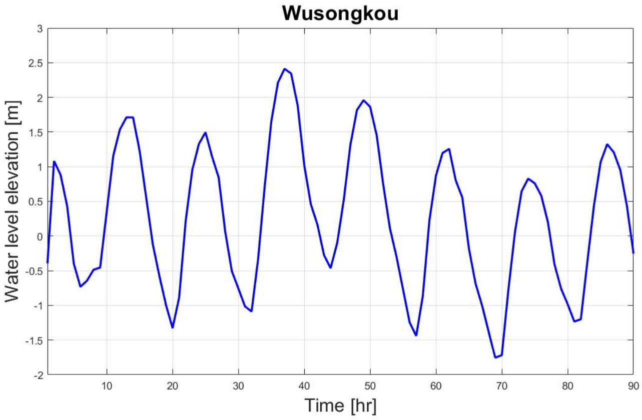

(a) R1.3

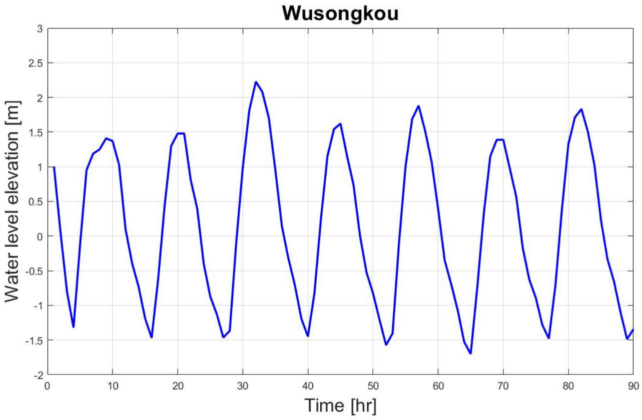

(b) R1.0

Fig. B.14.: Water level at Wusongkou during historical hypothetical events (part2)

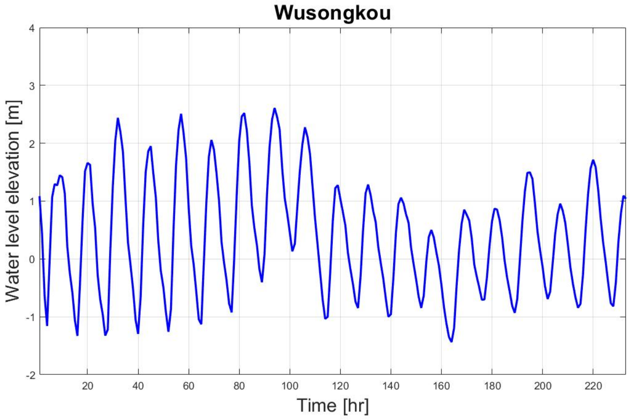

(a) R18.3

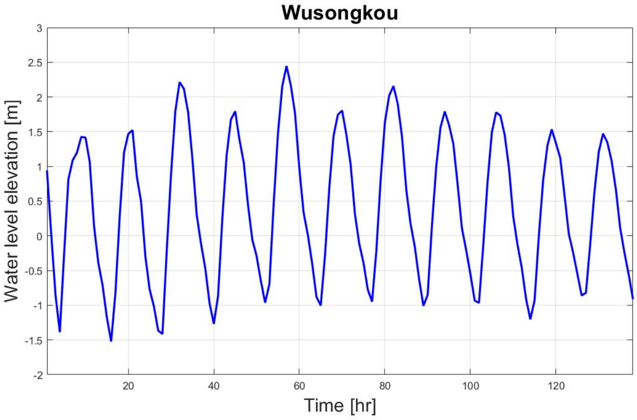

(b) R8.0

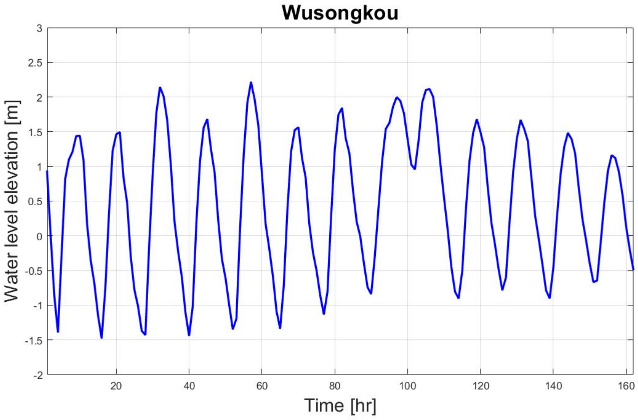

(c) R6.8

Fig. B.15.: Water level at Wusongkou during future hypothetical events (part 1)

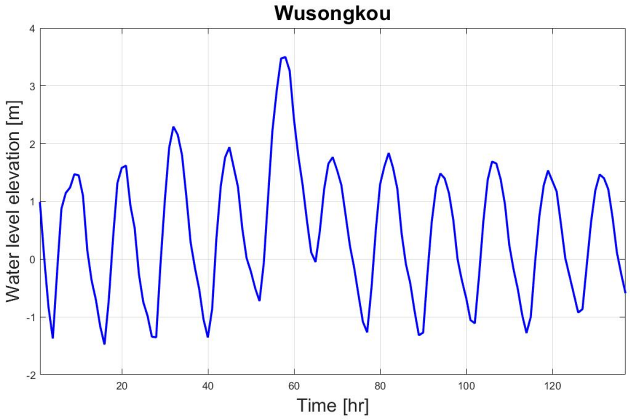

(a) R4.5

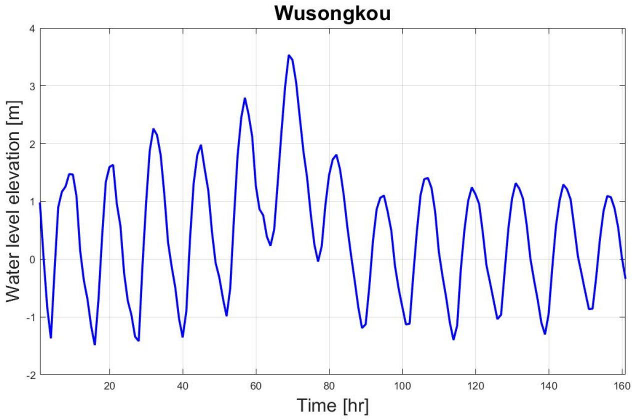

(b) R3.6

Fig. B.16.: Water level at Wusongkou during future hypothetical events (part 2)

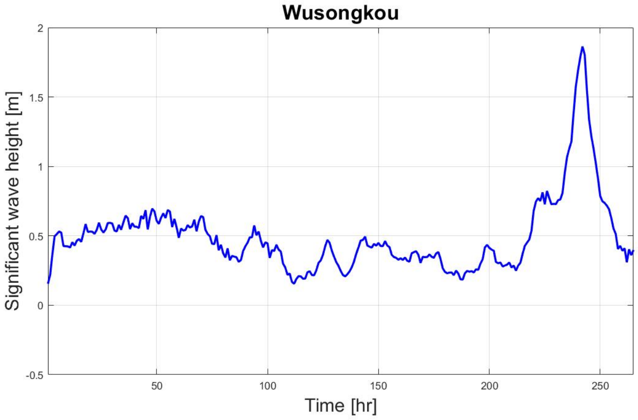

(a) R2.9

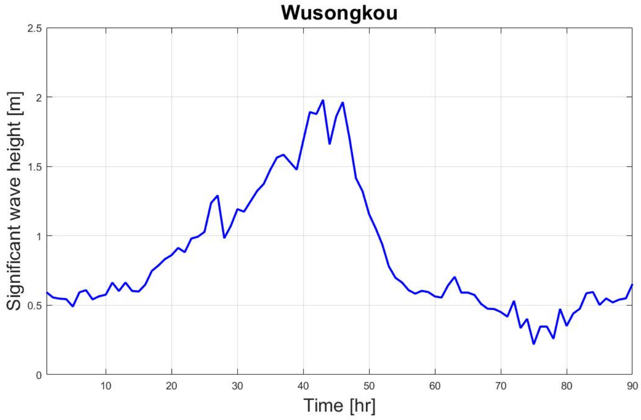

(b) R1.3

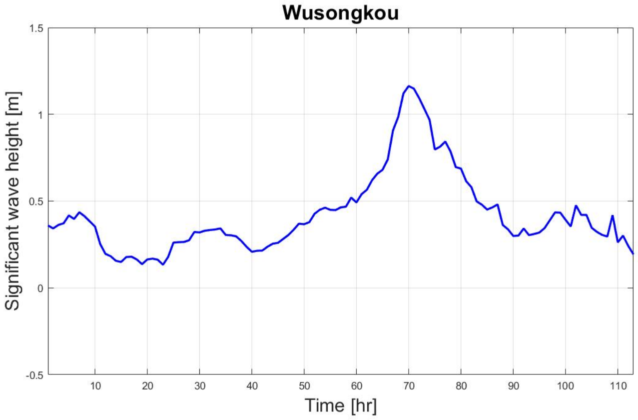

(c) R7.9

Fig. B.17.: Significant wave height at Wusongkou during hypothetical historical events (part 1)

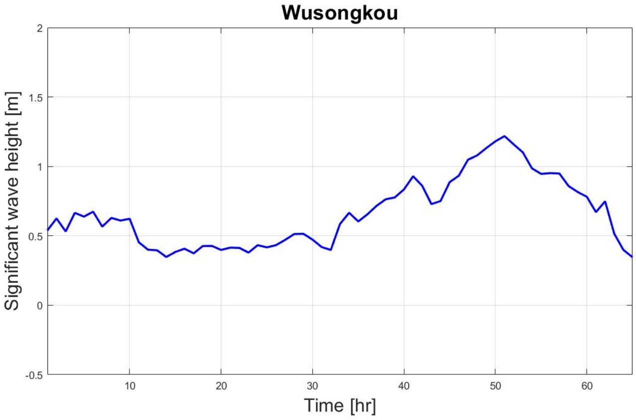

(a) R3.4

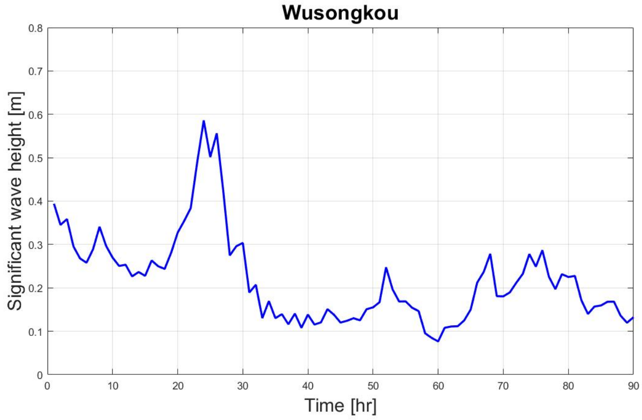

(b) R1.0

Fig. B.18.: Significant wave height at Wusongkou during hypothetical historical events (part 2)

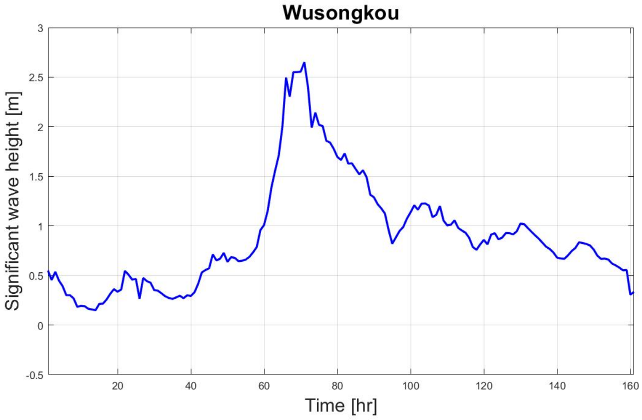

(a) R3.6

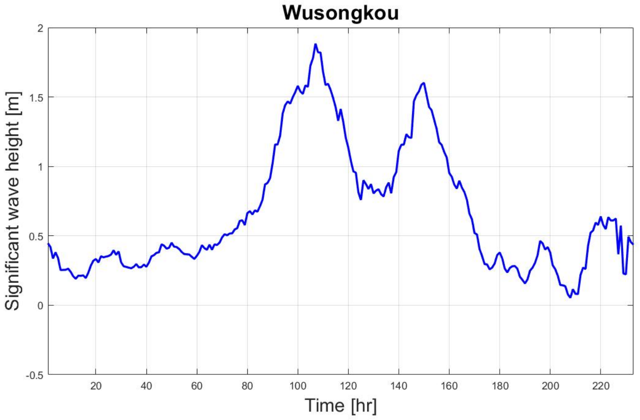

(b) R18.3

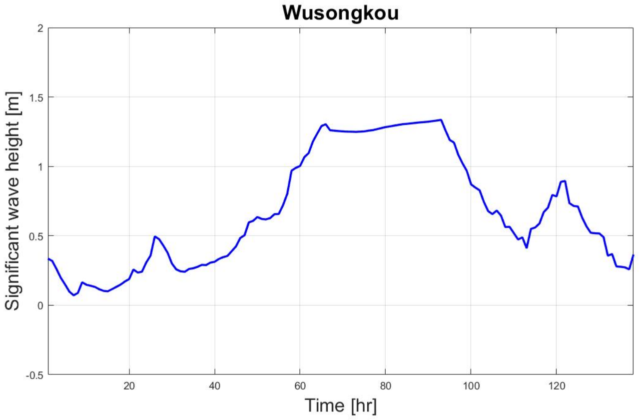

(c) R8.0

Fig. B.19.: Significant wave height at Wusongkou during hypothetical future events (part 1)

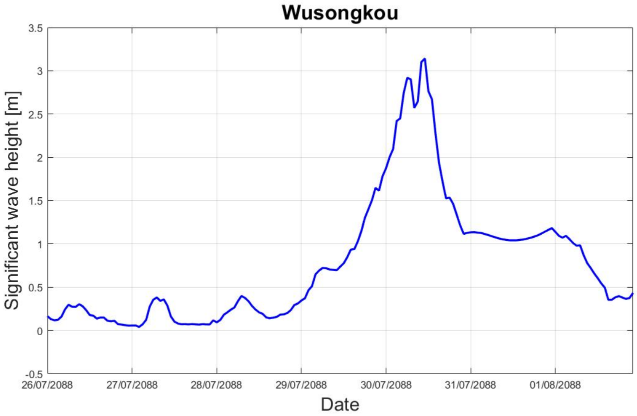

(a) R6.8

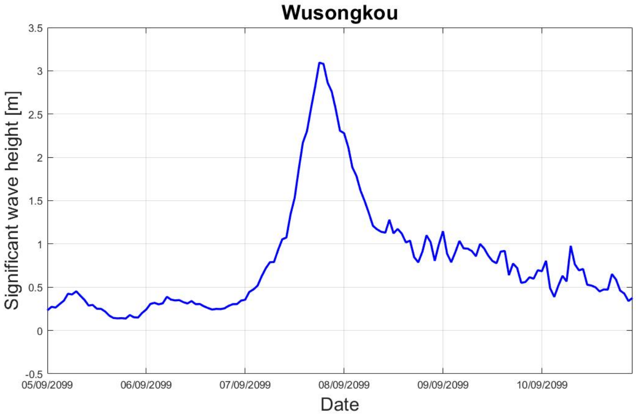

(b) R4.5

Fig. B.20.: Significant wave height at Wusongkou during hypothetical future events (part 2)

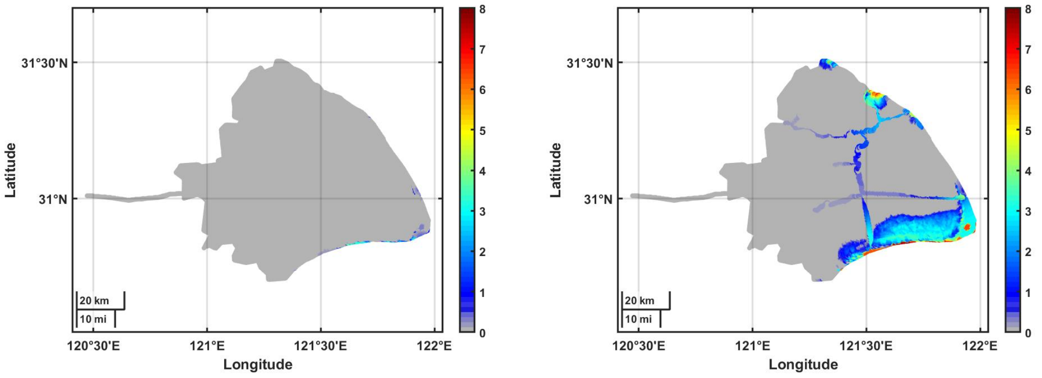

(a) 60h **(b)** 66h

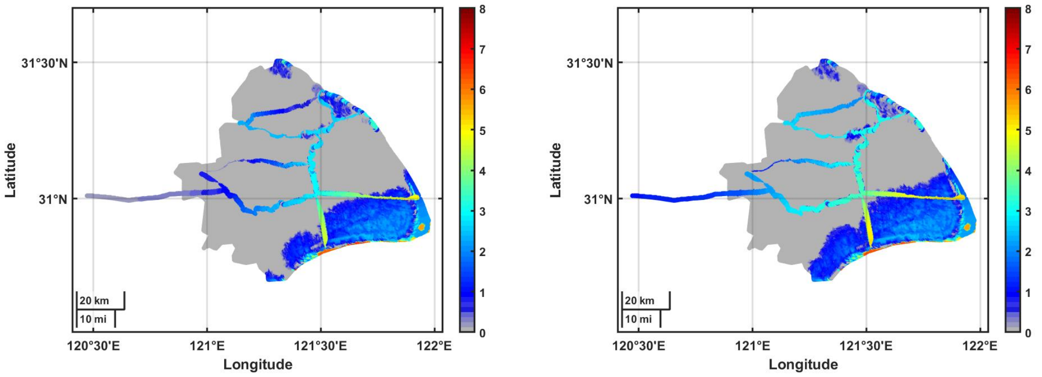

(c) 72h **(d)** 78h

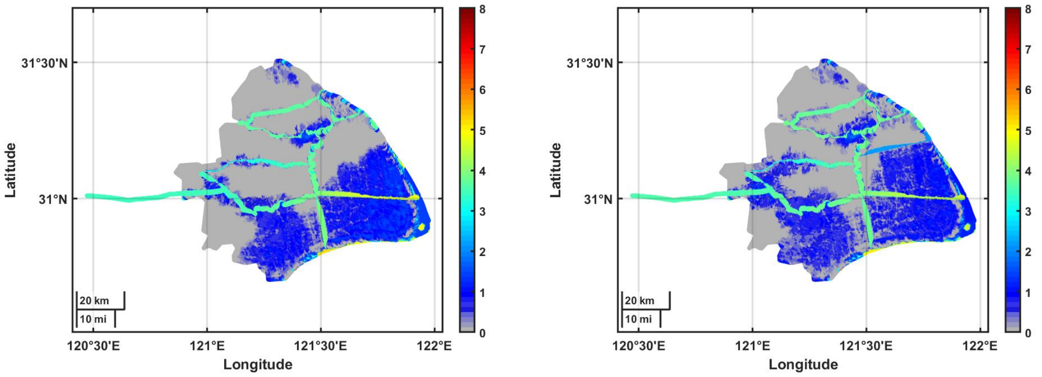

(e) 100h **(f)** 120h

Fig. B.21.: Inundation process in case R4.5 (B=500 m)

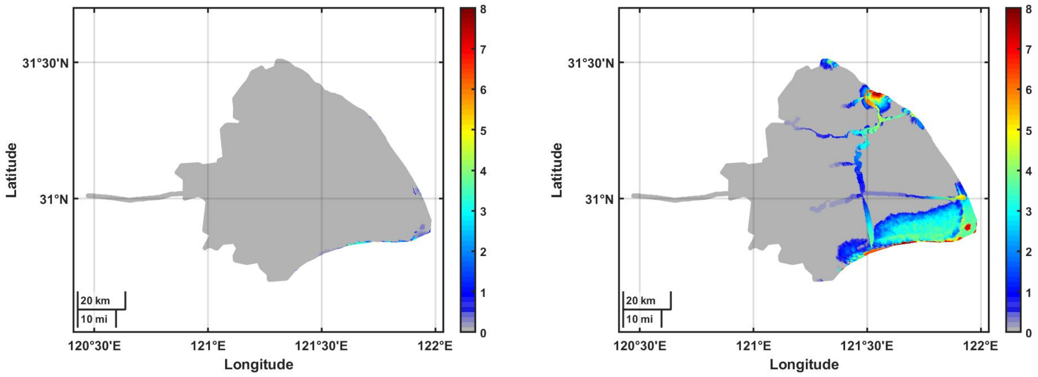

(a) 60h **(b)** 66h

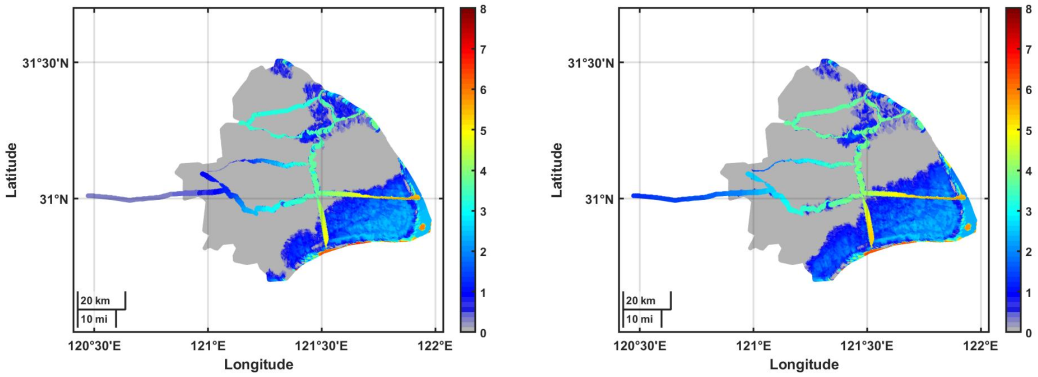

(c) 72h **(d)** 78h

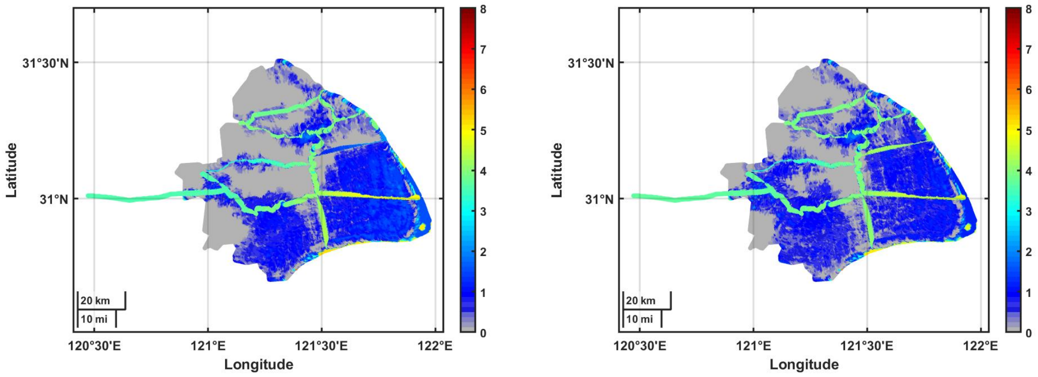

(e) 100h **(f)** 120h

Fig. B.22.: Inundation process in case R4.5 (B=1000 m)